Reverberation Mapping of the Accretion Discs in the Quasars 3C 273 and 1H 2106-099

JAMES THORNE

Reverberation Mapping of the Accretion Discs in the Quasars 3C 273 and 1H 2106-099

James Thorne

A Thesis presented for the degree of
Master of Science by Research

Department of Physics
Durham University
United Kingdom
September 2022

Abstract

The main aim of this thesis is to perform the first accretion disc reverberation mapping analysis on the AGN 3C 273 and 1H 2106-099 using the modern reverberation mapping algorithms Javelin, PyceCREAM and PyROA. This is with the intention of obtaining useful physical insights into these AGN and to compare the performance of the algorithms. Through spectral, photometric and reverberation mapping measurements we find evidence to suggest the accretion disc spectrum in 3C 273 follows a power law with a slightly shallower exponent $\beta \sim 1$ than expected from the approximated thin disc model ($\beta = \frac{4}{3}$). However the difference does not seem very significant and good agreement was found with the more physically meaningful unapproximated thin disc model simulated with a boundary condition at the radius of innermost stable circular orbit. We therefore conclude 3C 273 likely conforms to the thin disc model and displays the 'accretion disc size problem' with a scale $\sim 2 - 3$ larger than expected. For 1H 2106-099, we found an unexpected discontinuity in the PyROA and Javelin lag estimates which is reflected in the spectrum and which we cannot identify with any specific contamination. Investigating the possibility that the discontinuity is anomalous, we obtain corrected Javelin and PyROA lag estimates in near perfect agreement with the thin disc model without an up-scaled accretion disc. Our PyceCREAM RM results also indicate that the discontinuity is anomalous but differ from PyROA and Javelin in suggesting the accretion disc in 1H 2106-099 is up-scaled by a factor ~ 2. A secondary aim of the thesis was to investigate how the uncertainties on lag estimates returned by the algorithms depends on the length of the observing period and cadence of the light-curve data. Analysis on two dust reverberation mapping campaigns returned results which suggest that the length of the light-curve relative to the expected lag has a more significant effect on the size of the uncertainties than the cadence relative to the lag. We then estimate the optimum light-curve length to be $\sim 10\times$ the expected lag and the optimum cadence to be $\sim 6\times$ smaller than the expected lag which had associated lag uncertainties of $\sim 11\%$ and $\sim 10\%$ respectively.

Declaration

The work in this thesis is based on research carried out at the Department of Physics, Durham University, United Kingdom. No part of this thesis has been submitted elsewhere for any other degree or qualification and it is all my own work unless referenced to the contrary in the text.

Acknowledgements

I would like to acknowledge the invaluable guidance given by my supervisor Dr Hermine Landt-Wilman without which this thesis would not have been possible.

Contents

List of Figures

List of Tables

Dedication

Dedicated to my family.

CHAPTER 1

Introduction

Active galactic nuclei (AGN) are highly luminous phenomena thought to be exhibited in the behaviour of at least 40% of all nearby galactic nuclei (Collier, 1998). AGN are notable because they generate optical luminosities on scales similar to or greater than the total starlight luminosity of the host galaxies they are situated within (typically $\gtrapprox 10^{11} L_{\odot}$). Historically, a taxonomy developed to classify AGN based on their luminosity relative to their host galaxy. The two largest of these subclasses of AGN are Seyfert Galaxies and Quasars. In general, Seyfert galaxies are loosely defined as being AGN that emit at optical luminosities comparable to the total optical starlight luminosity from their host galaxy whilst Quasars are defined as being brighter than the starlight luminosity of their host galaxy by typical factors of a hundred or more.

The discovery of AGN as a separate astronomical class can reasonably be traced back to the classification of Seyfert Galaxies by Carl Seyfert (1943). Quasars were discovered shortly afterwards in the late 1950's by radio surveys such as the 3C catalogue (Edge et al. 1959). For more information about the history of AGN research please see Peterson (1997). Over the decades following these discoveries, the identity of AGN and the mechanism through which they generate their unprecedented luminosities has been a strong source of contention for astronomers. This debate has been complicated by the fact that, owing to their large extragalactic distances relative to observers, AGN are not currently spatially resolvable in telescopes meaning only indirect observations can be made to ascertain their

behaviour and structure. Nevertheless, a standard description of AGN behaviour has since emerged and is outlined in Figure 1.1. Much of the theory addressed in the following

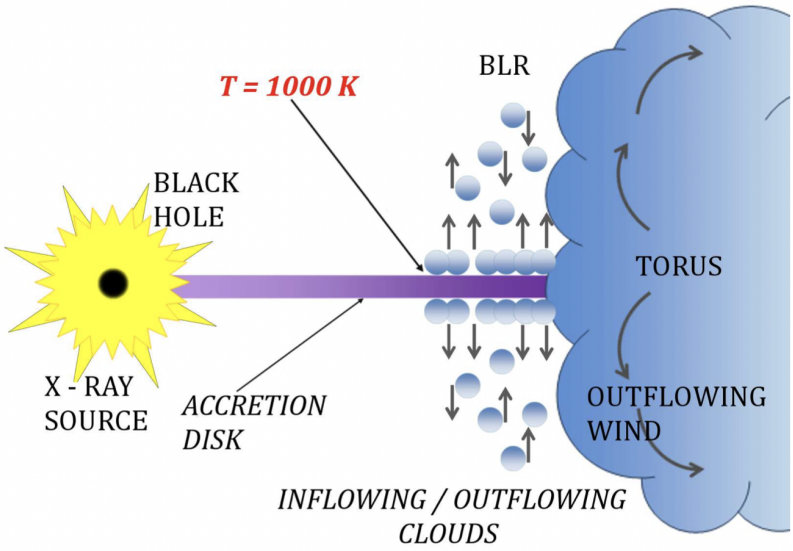

Figure 1.1: A schematic for the structure of the standard paradigm of AGN. The accretion disc exists on the order of light hours/days, the broad line region (BLR) on the order of light days, the torus on the order of light months to a year and the narrow line region (not shown) on the order of light years. This is taken from Czerny et al (2015) and displays the FRADO model for the formation of the BLR (see Appendix B.2.6

section was informed by Peterson (1997) and Netzer (2015).

1.1 Standard Paradigm of AGN

1.1.1 Black Hole Accretion

The most widely accepted mechanism for the production of energy in AGN is centred around the idea that mass accretion onto the super-massive black holes (SMBH) expected to exist at the centre of the AGN host galaxy is driving the luminosity. The development of this model can largely be attributed to the work done by Zel'dovich & Novikov (1964) and Salpeter (1964). In this picture the SMBH acts as a central engine, powering the heating of in-falling material to high temperatures through the influence of its large gravitational field. As such the AGN acts to convert a mass m of in-falling matter into energy equivalent to $E = \eta mc^2$ where η is the efficiency of energy conversion (typically assumed to be $\eta \sim 0.1$) and c is the speed of light. This means the luminosity $L \equiv \frac{dE}{dt}$ of the AGN can

be expressed as

$$L = \eta \dot{m} c^2, \tag{1.1}$$

where $\dot{m} \equiv \frac{dm}{dt}$ is the mass accretion rate. This model is supported by much indirect evidence including the detection of intra-day X-ray variability (from e.g. Terrell, 1967) which suggests the existence of a highly energetic but spatially compact source in the AGN. In addition to this, lower limits for the mass of this source can be obtained by substituting the measured bolometric luminosity of the central source L_{bol} as the Eddington luminosity defined as

$$L_E = \frac{4\pi G c m_p}{\sigma_e} M_E, \tag{1.2}$$

where G is Newtons gravitational constant, m_p is the proton mass, σ_e is the Thomson cross-section and M_E is the Eddington mass. The Eddington luminosity is the maximum possible luminosity that can maintain spherical accretion meaning the Eddington mass sets an estimate for the lower mass limit of an accreting source $M \geq M_E$. These considerations typically yield large mass estimates of $M \gtrapprox 10^8 M_\odot$ for AGN. Even larger mass estimates can be obtained using the virial theorem

$$M = \frac{f \Delta v^2 R}{G}, \tag{1.3}$$

where R is the radial distance from the central object in the AGN to a gravitationally bound structure typically estimated using reverberation mapping (see Section 1.1.3), Δv is the rotational velocity of the orbiting structure around the central object estimated from Doppler broadening of emission lines and f is a dimensionless scale factor that controls the geometry/inclination of the orbiting structure. This approach yields mass estimates typically an order of magnitude greater than those from the Eddington Luminosity. Whilst these mass estimates are crude, taken together these observations imply the existence of a super-massive, spatially compact central object in the AGN which is consistent with a SMBH.

1.1.2 The Accretion Disc Structure and Variability

It is considered unlikely that the accretion occurring in AGN will be spherically symmetric due to the strong likelihood that in-falling matter (from e.g. a rotating binary star) will approach the SMBH with a non-zero angular momentum. Conservation of angular momentum requirements would therefore constrain such in-falling material to rotate in a

plane perpendicular to its angular momentum vector. The gradual loss of gravitational potential energy as the matter spirals inwards would result in the material compacting along the direction parallel to its angular momentum vector in which its angular momentum is conserved. This is ultimately thought to lead to the formation of a so called 'thin accretion disc' around the SMBH. The physics of this thin disc model for accretion adopted by the 'Standard Paradigm' largely originated with the work done by Shakura & Sunyaev (1973) and describe an optically thick, geometrically thin acretion disc as the source of the majority of the AGN's luminosity.

The mechanism for generating this luminosity in the classic thin disc model is viscous heating in the accretion disc. By assuming the disc has a non-zero viscosity, in this picture viscous forces acting between adjacent annuli encircling the central SMBH at different rotation rates generate a torque acting against the direction of rotation of the inner, faster annulus. This torque effectively acts to slow down the rotation rate of elements in the inner annulus by transferring their angular momentum outwards thereby resulting in these elements spiralling inwards. In this way, the disc has a mechanism of transferring angular momentum in local parts of the disc outwards whilst conserving the total angular momentum of the entire disc meaning the stability of the disc as a whole is preserved.

The consequence of this friction in the disc (along with expected turbulence) is the conversion of gravitational potential energy of in-falling elements into thermal energy to locally heat the disc. This heating mechanism leads to an expected temperature gradient in the disc dependent only on the radius from the SMBH r, the SMBH mass M and the mass accretion rate $\dot{m}$ of the form

$$T^4(r) = \frac{3GM\dot{m}}{8\pi\sigma r^3}\left(1 - \sqrt{\frac{r_{ISCO}}{r}}\right), \tag{1.4}$$

where σ is the Stefan-Boltzmann constant and r_{ISCO} is the radius of innermost stable circular orbit around the SMBH. Here the boundary condition $\left(1 - \sqrt{\frac{r_{ISCO}}{r}}\right)$ ensures a hard boundary at the inner edge of the disc at r_{ISCO} but is often ignored as it becomes insignificant at $r >> r_{ISCO}$ distances. As such the temperature-radius relation above is often expressed in an approximated form as

$$T^4(r) = \frac{3GM\dot{m}}{8\pi\sigma r^3} \quad \text{for } r >> r_{ISCO}. \tag{1.5}$$

For a complete proof of Eq. (1.4) please see Shakura & Sunyaev (1973). Eq. (1.4) can also be proven using the virial theorem which is suitable for the classic thin disc model due to the inherent stability in the disc.

It is clear from Eq. (1.4) that only changes in the mass accretion rate $\dot{m}$ will lead to temperature variations for a particular annulus in a given classic accretion disc. By assuming a stable accretion disc with an approximately constant mass accretion rate, the thin disc model therefore provides a condition of thermal equilibrium for each annulus at radius r in the disc. This means the classic thin disc can be modelled as a collection of optically thick black-body emitters existing at each annulus at approximately constant temperatures. The emission of each annulus can therefore be modelled as a black-body spectrum with an intensity described by the Planck function

$$B_\nu(\lambda, T) = \frac{2hc}{\lambda^3} \frac{1}{e^{\frac{hc}{\lambda k_B T}} - 1}, \tag{1.6}$$

where h and k_B are the Planck and Boltzmann constants and the temperature of each annulus T is described by Eq. (1.4). As such the peak wavelength emitted by each black-body annulus can be modelled by Wien's law ($T \propto \lambda_{max}^{-1}$) which, when combined with Eq. (1.5), gives an expectation for the peak wavelength emitted by the classic thin disc to scale with radius as $R \propto \lambda^\beta$ where $\beta = \frac{4}{3}$.

The total flux at a given wavelength emitted across the entire accretion disc can be expressed as a sum of the flux contributions from each black-body annulus as

$$f_\nu = \int_{R_{in}}^{R_{out}} B_\nu(\lambda, T).d\Omega = \int_{R_{in}}^{R_{out}} \frac{2hc}{\lambda^3} \frac{1}{e^{\frac{hc}{\lambda k_B T}} - 1} \frac{2\pi R \cos i}{D^2}.dR, \tag{1.7}$$

where R_{in} and R_{out} are the inner and outer edges of the accretion disc respectively and $d\Omega \equiv \frac{2\pi R cos i}{D^2} dR$ is the solid angle of the disc at distances D and inclinations i with respect to observers. A representation of the contribution to the accretion disc spectrum from different parts of the disc is shown in Figure 1.2. It should be noted that different parts of the accretion disc will exist under different conditions and so should emit differently to each other. Shakura & Sunyaev (1973) argue that the inner regions of the accretion disc should experience significant non-thermal opacity from Compton scattering which would alter the shape of the spectrum to be more consistent with a Wien distribution. Nevertheless, they conclude that the outer regions of the disc can be expected to have predominantly thermal opacity and so can be well described by Plancks function Eq. (1.6) as done above.

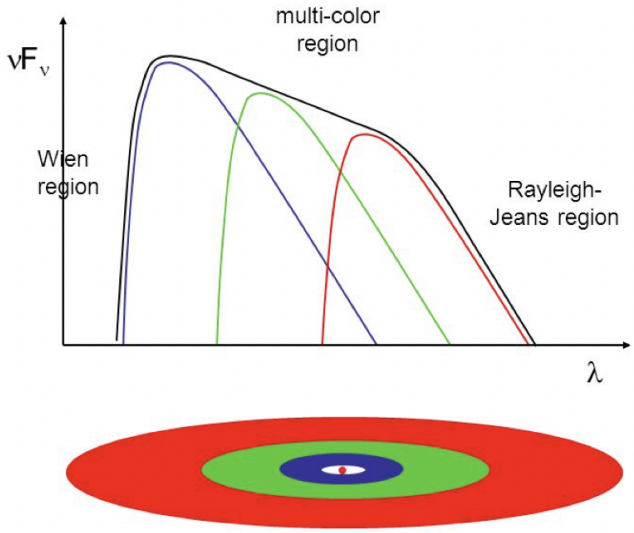

Figure 1.2: A representation of the accretion disc spectrum with different contributions from different regions of the disc. Author C.P. Dullemond.

In general, the UV and optical emitting regions of the accretion disc can be expected to lie comfortably within the Planckian regime and so can be well approximated by the description above.

In general the continuum component of measured spectral energy distributions (SED) of AGN, which are attributed to the accretion disc, are well described by power laws with respect to frequency $f_\nu \propto \nu^{-\alpha}$ to at least a low order approximation. By integrating Eq. (1.7) under certain approximations, the Planckian part of the accretion disc spectrum can be expected to follow a power law of the form $f_\nu \propto \nu^{\frac{1}{3}}$ if conforming to the thin disc model (please see Collier, 1998 for the proof). There is circumstantial evidence for this description of the accretion disc, namely the 'big blue bump' spectral feature observed in the UV and optical part of the SED of many AGN. This feature is widely considered to be thermal in nature with many linking it to an optically thick source consistent with an optically thick accretion disc emitting black-body spectra in the UV and optical and even at near-IR wavelengths if accretion disc radii are sufficiently large (Landt et al. 2011, 2019). However this explanation is not unique as it can also be explained from an optically thin source (Collier, 1998). Accretion disc reverberation mapping studies (e.g. Edelson et al 2019) typically estimate the scale of the accretion disc to be on the order of light hours or days.

However inconsistencies have been found between the timescales allowed by the classic thin disc model and those observed in AGN lightcurves. In particular, it is clear from Eq.

(1.4) that variations in the thermal flux emitted in a particular photometric band (which originates predominantly from a specific annulus in the disc) will be controlled by changes in the mass accretion rate which would act to perturb the local temperature of the disc and therefore alter the emitted flux. The timescale of these flux variations would therefore be expected to occur over 'thermal timescales' (ie. the timescales required for local regions of the disc to return to thermal equilibrium) which is typically on the order of months (see W. Ishibashi & T.J.L. Courvoisier, 2009). This is inconsistent with the observations of AGN lightcurves which regularly show flux variations on much shorter timescales typically on the order of days and hours.

This discrepancy has lead to modifications of the standard AGN paradigm. One of the more popular modifications is the 'lamp-post model' which adds a second source of luminosity into the classic thin disc description in an attempt to keep it consistent with observations (see Niedzwiecki et al 2016). This so-called lamp-post object is modelled as an emitter of short timescale variable flux and is located above the accretion disc such that it beams its emission onto the disc below (hence its name). In this picture, the lamp-post flux is reprocessed by each of the black-body annuli in the disc. This means that the short timescale variations in the lamp-post driving lightcurve are preserved in the reprocessed lightcurves from the disc (after a degree of blurring) thereby matching the observed timescales. To account for the highly variable emission, the lamp-post is expected to be constrained as a small structure and is likely located near the r_{ISCO} in order to explain the positive correlation between wavelength and lag found by reverberation mapping campaigns (e.g. Edelson et al, 2019). With this consideration in mind, the lamp-post is typically modelled as a zero-dimensional structure residing above the disc in line with its rotation axis. This has the effect of adding a second term to the classic temperature-radius relation Eq. (1.5) to account for the additional heating in the disc by the lamp-post such that

$$T^4(r) = \frac{3GM\dot{m}}{8\pi\sigma r^3} + \frac{L_b(1-a)h}{4\pi\sigma x^3} \quad \text{for } r >> r_{ISCO}. \tag{1.8}$$

where L_b is the luminosity of the lamp-post driving flux, a is the disc albedo, h is the height of the lamp-post above the disc and $x \equiv \sqrt{r^2+h^2}$ (see D. Starkey, K. Horne C. Villforth, 2016).

Currently there is no consensus on the possible identity of the lamp-post. However one compelling theory is that it can be attributed to the hypothesised accretion disc corona

which is modelled as a plasma of relativistic electrons surrounding the inner disc. In this picture, energetic electrons in a hot, optically thin part of the corona Compton up-scatter a fraction of the softer UV and optical photons from the inner accretion disc into the hard X-ray regime (defined typically at energies $E \geq 2 - 100$keV). It should be noted that Compton up-scattering is a process whereby relativistic particles impart energy and momentum onto photons via collisions thereby transforming them to higher frequency regimes. The hard X-rays emitted by the corona will then act as the lamp-post driving flux to be reprocessed by the disc. There is some indirect evidence to support this model such as observations (by e.g. Shappee et al, 2014 and McHardy et al, 2016) that suggest X-ray lightcurves may lead UV and optical lightcurves.

1.1.3 Broad Line Region

The SED obtained from real AGN are more complicated than the idealised spectrum depicted in Figure 3.4 for 3C 273. Real spectra contain emission lines superimposed onto the black-body continuum curve. A subset of observed AGN's appear to contain two distinct types of emission lines within their SED: 'broad emission lines' which are loosely defined as having full widths at half maximum (FWHM) corresponding to orbital velocities of ~ 5000 kms^{-1} and 'narrow emission lines' which are loosely defined as having FWHM corresponding to orbital velocities of ~ 500 kms^{-1} (see Collier, 1998). A taxonomy exists based around the prevalence of these two types of emission lines with so-called Type 1 AGN being classified as having both broad and narrow emission lines present in their SED and Type 2 AGN being classified as having only narrow emission lines present. It should be noted that this classification scheme is widely considered to be outdated due to the popularity of unification schemes which suggest the differences between Type 1 and 2 AGN's are not physical in nature but are only a matter of orientation (see Section 1.1.4).

As elucidated above, the classic thin accretion disc is expected to emit as a continuum meaning the existence of broad emission lines in the spectra of Type 1 AGN's implies the existence of a separate structure. As already stated, the likelihood of unification between Type 1 and 2 AGN's means this additional structure likely also exists in Type 2 AGN. This so-called 'broad line region' (BLR) is expected to exist further from the SMBH than the accretion disc. This has been well verified by reverberation mapping campaigns which regularly show the broad emission line lightcurves to lag with respect to the accretion disc continuum and place the linear extent of the BLR on the order of light days (see e.g. De

Rosa et al 2018).

In addition to broad emission lines, narrow emission lines are seen in the spectra of Type 1 and Type 2 AGN. As a result of Doppler Broadening effects (Peterson, 1997), narrow emission lines are thought to originate from a separate structure significantly further from the SMBH than the BLR called the narrow line region (NLR) which corresponds to rotational velocities approximately an order of magnitude slower than for the broad emission lines. The NLR exists at large enough distances from the SMBH that it is spatially resolvable for some AGN and is thought to reside at a length scale on the order of light years (see Collier, 1998). As a result, the flux from the NLR is essentially constant over timescales of about a decade meaning RM based on spectra can calibrate their spectral flux scale based on the flux from the NLR.

1.1.4 The Dusty Torus

Photometric near Infrared reverberation mapping campaigns (e.g. Koshida et al, 2014) reveal the lightcurves of near infrared bands lag with respect to the accretion disc continuum on typical timescales of a few months to about a year. This suggests the existence of a final structure to incorporate into the standard paradigm existing at the outer edge of the AGN. At this large distance, the structure would be cool enough to be expected to be comprised of dust sublimated from gas and would re-emit continuum flux from the accretion disc as a black-body peaked strongly in the infrared. Unification schemes between Type 1 and Type 2 AGN incorporate this dusty structure by modelling it as a torus enveloping the entire AGN. These unification schemes are widely accepted and attempt to explain the observed differences between Type 1 and Type 2 AGN due to differences in their orientation with respect to observers rather than any physical differences. In this picture, Type 1 AGN are orientated approximately face on with respect to the observers line of sight meaning both the BLR and NLR are exposed. Type 2 AGN are modelled as being orientated at larger inclinations with respect to an observers line of sight meaning the BLR is obscured by the side of the torus whilst the NLR is far enough from the SMBH to still be visible.

1.2 Case Studies: 3C 273 and 1H 2106-099

The two AGN 3C 273 and 1H 2106-099 are objects of major importance for the analysis carried out later in the thesis. Therefore, a brief mention of their properties and observational history is given below.

1.2.1 3C 273

3C 273 is of historical importance as it is the first discovered Quasar and was identified as existing at extra-galactic distances by Schmidt (1963) by the identification of the Hydrogen Balmer series in its spectrum. This enabled an estimate of the redshift $z = 0.158$ and therefore a measure of its large luminosity $L_{bol} \sim 10^{46}$ ergs^{-1} (Landt et al 2011). The scale of this luminosity was unprecedented at the time and spurred on the creation of the Quasar class of AGN. The large bolometric luminosity in 3C 273 indicates that its accretion disc, BLR and torus exist on large scales. This has been verified by observations from the infrared interferometric instrument GRAVITY on ESO's VLT (Sturm et al. 2018; Gravity Collaboration et al. 2020) which has spatially resolved the torus and BLR. Subsequent observations of 3C 273 revealed its existence as a 'blazar' which are a subset of AGN which exhibit abnormally large short timescale variability on the day and intra-day scale (Peterson, 1997). These unique properties are attributed to the effect of a relativistically beamed radio jet.

Jets in AGN are well documented phenomena and exist as extended linear structures reaching out to kpc distances that they can be well resolved spatially (see Bridle, Perly 1984). The emission received from jets extends over almost the entire electromagnetic spectrum and is non-thermal in nature, being widely believed to originate from synchrotron emitting relativistic particles accelerated by a magnetized accretion disc and/or a spinning Kerr black hole (for more information please see Dutan, I., 2010). In the case of blazars like 3C 273, the jet is expected to lie on or close to the observers line of sight meaning it is relativistically beamed to much greater apparent luminosities. As such the jet is thought to have a disproportionately large influence on the spectra of blazars thereby explaining their unique properties. Specifically, 3C 273 is classified as a 'flat spectrum radio quasar' (FSRQ) which is a subset of blazars characterised by having strong emission lines as can be seen in Figure 3.2. Wide wavelength range spectral observations of 3C 273 taken over the course of 40 years compiled by Soldi, S et al (2008) reveal two broad peaks in the SED (reproduced as Figure 1.3): a lower energy hump spanning the infrared into the optical

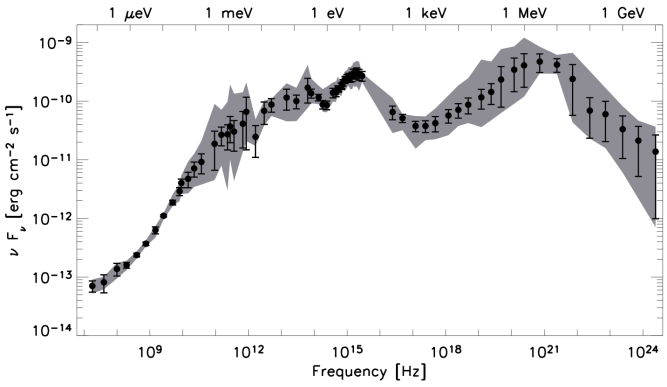

Figure 1.3: SED of 3C 273 spanning the radio to gamma ray regions taken from Figure 3 in Soldi et al (2008).

attributed to synchrotron radiation from the jet and a higher energy hump peaked in the gamma ray region attributed to inverse Compton scattering by relativistic electrons (see Berton et al 2018). Optical spectral analysis carried out by Yuan et al (2022) also reveals a prominent blue-bump feature (as seen in Figure 3.2) which indicates that most of the optical spectrum of 3C 273 is likely dominated by the thermal accretion disc emission instead of the jet.

1.2.2 1H 2106-099

The AGN 1H 2106-099 is a member of the Seyfert 1 galaxy class located relatively nearby at redshift $z \sim 0.027$. As a Seyfert galaxy, 1H 2106-099 can be expected to emit at optical luminosities comparable to the total optical starlight luminosity from its host galaxy meaning host galaxy contamination of the flux received from this AGN is an important factor to consider. Landt et al (2011) were not able to obtain confident estimates of the scale of the host galaxy contamination although the flattened spectrum obtained is suggestive of significant levels of contamination as shown in Figure 3.15 in Section 3.4.1.

Like other Type 1 AGN's, 1H 2106-099 has strong broad and narrow emission lines present in its spectrum as shown in Figure 3.3. These are mostly typical of emission lines found in other Seyfert 1 galaxies but with an unusually strong HeI line (Remillard, 1986). Rather unusually for Seyfert 1 galaxies, 1H 2106-099 is also likely to be a strong emitter of highly variable X-rays due to the presence of FeX lines (Remillard, 1986) which is a high excitation line present in other strong X-ray emitters at similar relative intensities (e.g. NGC 4151 see Remillard, 1986 and Mushotzky et al, 1980). According to the coronal theory of X-ray emission in AGN's outlined above, this may indicate a very active

corona in 1H 2106-099. It should also be mentioned that the spectrum shown in Figure 3.15 indicates only a weak blue-bump which was similarly concluded by spectral analysis carried out by Grossan et al (1996). In contrast to 3C 273, 1H 2106-099 does is considered a radio-quiet AGN as it does not have a strong radio jet but is a much more active X-ray emitter. 1H 2106-099 also emits at a bolometric luminosity approximately a factor of 10 more dimly than 3C 273 (Landt et al 2011).

1.3 Reverberation Mapping

It is incredibly difficult to obtain detailed measurements of most AGN and their central SMBH's due to their large extragalactic distances from observers. As such, it is not currently possible to spatially resolve the inner regions of most AGN owing to the small angular distances meaning no direct observations can be made to constrain the AGN's mass and geometry. There are a few exceptions of nearby, bright AGN (e.g. 3C 273) for which infrared interferometry can resolve the torus and sometimes BLR. Nevertheless, indirect methods of observing the AGN have been developed including probing the radio emitting locations using Very Long Baseline Interferometry (e.g. Gabanyi et al, 2019), the use of gravitational microlensing (Stalevski et al, 2012) and reverberation mapping (RM). RM uses the fact that different spectral features of the AGN can be attributed to different structures (following the standard paradigm) to estimate the linear distances between these structures. By modelling the emission from these different structures as reprocessed accretion disc flux, the observed lags between the light-curves from these structures and the accretion disk continuum light-curve can be used to estimate the distance between the accretion disc and the structure assuming the lag is entirely due to light travel time.

The most common form of RM is done in the BLR regime and attempts to measure the distances between the accretion disc and the BLR for a given AGN as represented in Figure 1.4. This is done by obtaining light-curves in photometric bands corresponding to a strong broad emission line and a smooth, continuous part of the SED which can be expected to originate predominantly from the BLR and accretion disc respectively. As mentioned above, emission line light-curves are regularly found to lag with respect to the continuum meaning, if these lags can be accurately estimated, the distance between the accretion disc and BLR can be trivially determined. The expected relationship between

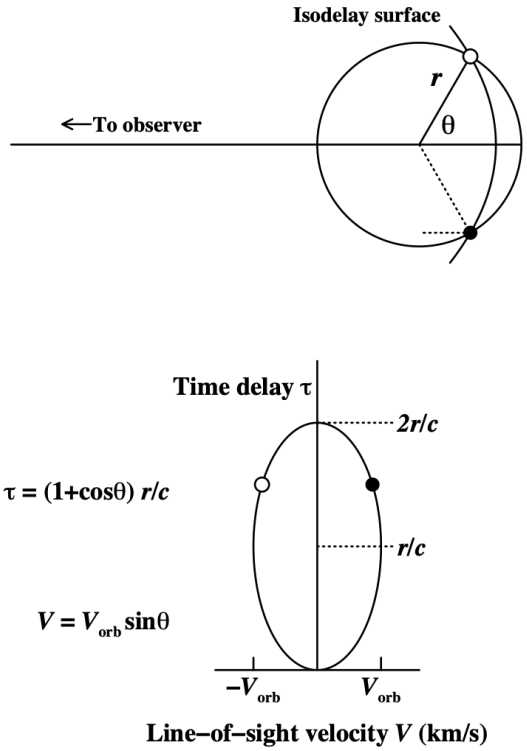

Figure 1.4: A diagram of the mechanism of BLR RM. The upper figure shows a spherically distributed BLR at radius r from the SMBH emitting reprocessed continuum flux as emission line flux. The observer will see the emitting clouds lying on an 'isodelay surface' with a lag with respect to the continuum given by Eq. (1.11). The lower figure shows the BLR orbital velocity-time delay plane. This figure is taken from Peterson & Horne 2004.

the light-curve lag τ and linear distance r is

$$\tau(r) = \frac{r}{c}, \tag{1.9}$$

which assumes that the lag is entirely attributed to the greater light travel time taken for the accretion disc flux to travel to the BLR and then to the observer as reprocessed emission line flux compared to travelling straight from the accretion disc to the observer as continuum flux. In addition to producing estimates for the general length scales in AGN, RM campaigns can give more finely tuned measurements by carefully selecting continuum bands and emission lines to sample light-curves which correspond to specific parts of the accretion disc and BLR. For instance high excitation emission lines can be expected to occur more strongly in the hotter, more strongly ionised inner part of the BLR facing the accretion disc. RM in the BLR regime is also useful because the distance estimates it provides can be used in Eq. (1.3) to give an independent estimate of the SMBH mass at

the centre of the AGN (Peterson et al, 2004).

RM requires several assumptions to hold true such, as already stated, assuming the light travel time is the most significant timescale (and so the flux reprocessing time is negligible). This seems likely justified when compared to the expected dynamical and recombination timescales (see Collier, 1998 for more information). RM also assumes that the observed continuum flux originates from a single source (namely the accretion disc) which exists on smaller spatial scales than the BLR. In addition, the observed continuum flux is assumed to be simply related to the ionising continuum flux reprocessed by the BLR (but not necessarily in a linear way) such that the observed continuum flux can be used as a substitute for the unobserved ionising flux that produces the broad emission lines.

One complication is the fact that the response of the BLR to variations in the continuum flux will likely not be trivial (ie. one to one). Variations in the emissivity of the material in the BLR as well as effects arising from the geometry and dynamics of the individual gas clouds making up the BLR will act to blur the reprocessed light-curve with respect to the continuum (see Collier, 1998). This blurring will be further compounded by the fact that the accretion disc is expected to be an extended structure emitting as a black-body meaning photometric light-curves being reprocessed by the BLR will not originate from a point source but from across the whole disc. The effect of these unknown physical conditions are represented by a transfer function $\psi(\tau)$ which controls the blurring of the response light-curve. The majority of RM techniques assume a simple linear relationship between the observed continuum flux $f_c(t)$ and the unobserved ionizing continuum such that the lagged light-curve $f_L(t)$ can be represented as

$$f_L(t) = \int \psi(\tau) f_c(t-\tau).d\tau. \tag{1.10}$$

Eq. (1.10) takes the form of a convolution whereby the transfer function $\psi(\tau)$ controls the response of the line light-curve to a Dirac delta continuum pulse. In essence, Eq. (1.10) describes the lagged light-curve at time t as a weighted sum of the continuum over all lags weighted by the transfer function which controls the influence of each part of the continuum light-curve over the lagged light-curve at time t. Determining an appropriate transfer function is an important consideration for any RM campaign.

More recently, RM is also performed in the torus and accretion disc regimes. Accretion disc RM assumes the driving light-curve originates from the lamp-post meaning the

majority of all continuum variability on timescales shorter than typical light travel times within the disc can be attributed to it. This raises unique challenges for accretion disc RM campaigns due to the fact that little variability is typically seen on these short timescales (e.g. Mudd et al, 2018). Another complication arises from the accretion disc geometry which means the inclination of the disc i with respect to observers should be accounted for in the analysis. This has the effect of altering Eq. (1.9) to

$$\tau(r, \phi, i) = \frac{r}{c}(1 + \sin i \cos\phi), \tag{1.11}$$

where ϕ is the azimuthal angle for the reprocessing region (Starkey et al. 2016). This consideration is generally not a concern for BLR RM as the BLR is usually modelled as being spherically distributed around the SMBH. It should be noted that the inclination i of the accretion disc has no effect on the mean lag obtained defined as $\langle\tau\rangle \equiv \frac{\int \tau\psi_\nu(\tau,\lambda)}{\int \psi_\nu(\tau,\lambda)}$. This is shown in Figure 1.5 (taken from Starkey et al. 2016) which shows the variation in the accretion disc transfer function described below with inclination.

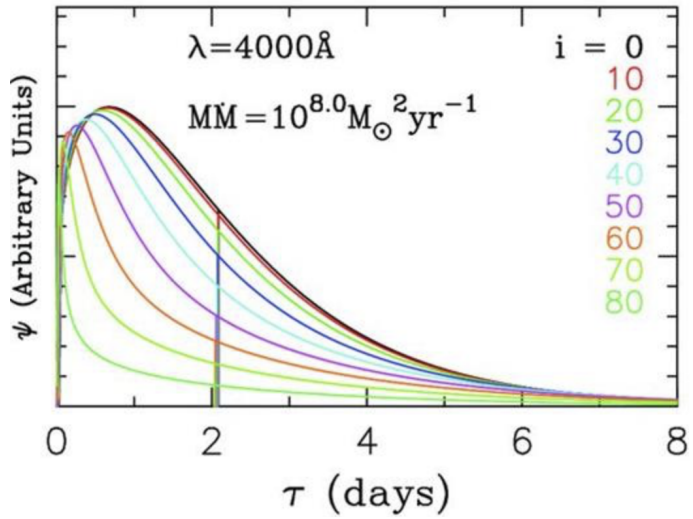

Figure 1.5: Variations of the accretion disc transfer function ψ with inclination i taken from Figure 3 in Starkey et al (2016). Here the lamp-post height $h_x = 3r_s$ and the mean lag $\langle\tau\rangle$ is represented by the vertical lines.

Like RM in the BLR regime, accretion disc RM must also take account of blurring effects in the reprocessed light-curves by introducing a transfer function. In accretion disc RM, the transfer function will also include the blurring introduced by the extended nature of the lamp-post, the variable emissivity of different parts of the disc as well as the likelihood of multiple reprocessings happening within the disc. The expected form of the transfer

function within the accretion disc can be physically derived from the thin disc model by invoking the Planckian description of the reprocessed flux Eq. (1.7). The form of the accretion disc transfer function is shown below as outlined by Collier (1998) and Cackett et al (2007)

$$\psi_\nu(\tau|\lambda) = \int_{R_{in}}^{R_{out}} \int_0^{2\pi} \frac{\partial B_\nu(T,\lambda)}{\partial T} \frac{\partial T}{\partial L_x} \delta(\tau - \frac{r}{c}(1 + \sin i \cos\phi)).d\Omega, \tag{1.12}$$

where L_x is the driving luminosity from the lamp-post and Ω is the solid angle defined in Eq. (1.7).

1.4 Reverberation Mapping Algorithms

Reverberation Mapping techniques rely on obtaining accurate time lag estimates between a series of AGN light-curves, typically by assuming the lagged light-curves are linearly related to the driving light-curve according to Eq. (1.10). Due to the finite sampling of the data and gaps in time coverage, this involves fitting the light-curves by assuming the reverberating light-curves are lagged, blurred versions of the driving light-curve. This is not a trivial task as AGN light-curves appear to be aperiodic and stochastic in nature which makes them challenging to fit.

Traditionally, lag estimates were usually obtained by determining the peak in the cross correlation function (CCF) between light-curves after a simple interpolation had been done between the data points (often just a linear interpolation, see Gaskell, Peterson, 1987). However, advances in computing capabilities and the growth in machine learning in recent years has enabled more sophisticated methods of interpolation and lag estimation to be developed. Modern methods of RM employ Bayesian statistics to optimise the parameters for the light-curve fits and use Markov Chain Monte Carlo (MCMC) techniques to sample the resulting posterior distributions. This has advantages over traditional statistical methods as it leads to posterior parameter distributions (as opposed to single best-fit values) which allows more natural estimates of uncertainties to be obtained, typically determined by the width of these distributions. The most common RM algorithms currently in use are Javelin (developed by Zu, Y., Kochanek C. S., Peterson B. M., 2011), PyceCREAM (developed by Starkey, D. A., Horne, K., Villforth, C. 2016) and PyROA (developed by Donnan , F R. et al, 2021) and will be the main methods of analysis for the rest of the thesis. A general description of each algorithm is given below. For a brief explanation of

MCMC and how it relates to Bayesian statistics please see the statistics background in the Appendix A.0.1.

1.4.1 Javelin

The following explanation draws heavily from Zu, Y., Kochanek C. S., Peterson B. M., (2011) and is focused on the 'Rmap Model' mode. Javelin obtains lag estimates by modelling AGN light-curves as damped random walks (DRW) which is motivated by their stochastic appearance and the power spectrum of optical light-curves being well described by $\frac{1}{\nu^2}$ power laws consistent with random walk processes (see Kelly, B. C., Bechtold, J., Siemiginowska, A. 2009). As such, Javelin treats AGN light-curves as stochastic time series described by the Ornstein-Uhlenbeck (O-U) process (see Gillespie, D. T. 1996) which has as an exponential autocovariance function between times t_i and t_j of the form

$$\langle s_c(t_i)s_c(t_j)\rangle = \frac{\tau_d\hat{\sigma}^2}{2}e^{-\frac{|t_i-t_j|}{\tau_d}} \tag{1.13}$$

where τ_d and $\hat{\sigma}$ can be interpreted as the decorrelation timescale and the short timescale variability respectively for the light-curve. The driver-lagged and lagged-lagged covariance functions can also be trivially derived by assuming the lagged light-curves are linearly related to the driver by Eq. (1.10). To do this Javelin uses a simple top-hat transfer function defined as

$$\psi(t-t') = \frac{A}{t_2-t_1} \qquad t_1 \leq t-t' \leq t_2, \tag{1.14}$$

where A is the amplitude of the top-hat and $t_2 - t_1 \equiv w$ is the width. The average lag $\langle\tau\rangle$ is defined as the mid-point of the top-hat whilst the width controls the degree of blurring.

To perform the fit on N_D data points across N_L light-curves, Javelin decomposes the $(N_D \times 1)$ light-curve data vector $\underline{y}$ into three parts

$$\underline{y} = \underline{s} + \underline{n} + \mathbf{L}\underline{q}, \tag{1.15}$$

where $\underline{s}$ are the best-fit light-curve signals, $\underline{n}$ is the measurement error in the data, $\mathbf{L}$ is a $(N_D \times N_L)$ matrix and $\underline{q}$ is a $(N_L \times 1)$ vector with entries corresponding to the mean fluxes of the N_L light-curves in the data set. The $\mathbf{L}\underline{q}$ term is introduced so that the mean fluxes can be easily removed from the data when doing the fit for the purposes of

linear de-trending. This is an important step as much of the statistical analysis done to fit light-curve data works on the assumption that the process is stationary (ie. the mean and variance are time independent) despite the fact many light-curves are observed with trends in their mean. Denney et al (2010), Li et al (2013) and Peterson et al (2014) all demonstrate the problems long timescale trends bring to RM campaigns by introducing a different component of variability operating on longer timescales. RM techniques will often find solutions for both the trend and the AGN variability meaning the trends can introduce false peaks into the lag distributions. Welsh (1999) in particular highlights the specific effect trends have on CCF analysis in biasing the lag estimates towards zero. Without a detrending function, RM algorithms are limited to fit only stationary periods of the light-curves thereby limiting the accuracy of these fits as the entire data-set cannot be used.

Javelin fits the light-curves simultaneously using a Gaussian Process by treating the $\underline{s}$ and $\underline{n}$ parameters as random variables with Gaussian probability distributions $P(\underline{s}) \propto |S|^{-\frac{1}{2}} e^{-\frac{1}{2}(\underline{s}^T \mathbf{S}^{-1} \underline{s})}$ and $P(\underline{n}) \propto |N|^{-\frac{1}{2}} e^{-\frac{1}{2}(\underline{n}^T \mathbf{N}^{-1} \underline{n})}$ with covariance matrices $\mathbf{S} = \langle \underline{s}\underline{s} \rangle$ and $\mathbf{N} = \langle \underline{n}\underline{n} \rangle$. In particular, the covariance matrix $\mathbf{S}$ is a generalisation of the O-U process such that the diagonal autocovariance elements are given by Eq. (1.13) whilst the off-diagonal elements correspond to covariance between separate light-curves. As such, the DRW is encoded in the kernel of the Gaussian process. The Gaussian distributions $P(\underline{s})$ and $P(\underline{n})$ enable a likelihood to be defined which give best-fit constraints for the light-curve variability $\hat{\underline{s}}$ and mean $\hat{\underline{q}}$. The final Javelin fit $\underline{s} = \hat{\underline{s}} + \underline{u}$ has a random Gaussian term $\underline{u}$ added to the optimum fit to give the fit the appearance of stochasticity. The optimum fit parameters τ_d, $\hat{\sigma}$ and τ_i, w_i and A_i for each i^{th} light-curve are sampled using the 'emcee' MCMC sampler (Foreman-Mackey et al 2012).

It should be mentioned that, before doing the joint light-curve analysis, Javelin first fits the driving light-curve alone in order to calibrate the τ_d and $\hat{\sigma}$ parameters by using Log-Gaussian priors on each centred at the median cadence and standard deviation of the light-curve data. This is done to discourage τ_d and $\hat{\sigma}$ values that deviate too much from the median sampling interval and standard deviation respectively. The purpose of this is to try to avoid 'white-noise' fitting solutions which involve the fitting of incorrect lags by the algorithm sending $\tau_d \to 0$ (ie. treating the data points as uncorrelated) and broadening $\hat{\sigma}$ such that a white-noise signal with variability much shorter than the typical sampling intervals is fit. This will always be a solution for Javelin at any lag as uncorrelated white-

noise can be matched at any lag (see Zu, Y., Kochanek C. S., Peterson B.M., 2011). For a more detailed explanation of the statistical method used by Javelin and the new 'disc Mode' please see Appendix A.0.2.

1.4.2 PyROA

The following explanation draws heavily from Donnan, F R. et al (2021). PyROA attempts to fit light-curve data in a more traditionally statistical approach compared to the Machine Learning method used by Javelin. Unlike Javelin, PyROA does not fit AGN light-curves using a model of variability but rather fits each light-curve directly using a running optimal average (ROA). The ROA is as an optimal inverse-variance weighted average of all the N data points D_i with errorbars σ_i in the light-curve measured at times t_i such that at time t

$$X(t) = \frac{\sum_{i=1}^{N} D_i W_i(t)}{\sum_{i=1}^{N} W_i(t)} \tag{1.16}$$

where the weighting of each data point to the fit

$$W_i(t) = \frac{1}{\sigma_i^2} e^{-\frac{1}{2}\left(\frac{t-t_i}{\Delta}\right)^2}. \tag{1.17}$$

This approach follows a traditional inverse variance weighted average with an added Gaussian window function Eq. (1.17) which lessens the influence data points have on the fit according to how far they are from time t and how much error they have (see Donnan , F R. et al, 2021 for more detail). Following from the traditional inverse variance weighted average, the variance of the fit $X(t)$ is defined as

$$Var(X(t)) = \frac{1}{\sum_{i=1}^{N} W_i(t)} \tag{1.18}$$

which determines the 'error snake' obtained from PyROA fits.

The Δ parameter in the weights corresponds to the width of the Gaussian window function and therefore controls how quickly the influence data points have over the fit diminishes with time separation. The scale of Δ is therefore a measure of the flexibility of the fit. If Δ is small, $X(t)$ is sensitive to rapid variations in the data leading to a close fit meaning the model has a large effective number of parameters whilst if Δ is larger, $X(t)$ is stiffer and can only follow slower variations in the data leading to a worse fit meaning the

model has a smaller effective number of parameters. Clearly having too large a value of Δ is undesirable as it leads to a poor fit but conversely having too small a value of Δ is also undesirable as it can lead to over-fitting noisy data. A compromise between simplicity in the model and a good fit to the data can be found by minimising the Bayesian Information Criterion (BIC) statistic.

The best-fit is determined for each i^{th} light-curve by shifting the ROA by the appropriate lag τ_i and scaling it by the appropriate rms A_i and mean B_i such that

$$f_i(t) = A_i X(t - \tau_i) + B_i. \tag{1.19}$$

PyROA samples posterior distributions for the fitting parameters A_i, B_i, τ_i and s_i for each i^{th} light-curve using the 'emcee' MCMC sampler (Foreman-Mackey et al 2012) with the BIC as the likelihood and uniform priors for the parameters.

By using the same ROA $X(t)$ for all light-curves in Eq. (1.19), PyROA assumes a single level of blurring for all light-curves controlled by the window function in Eq. (1.17). This means, by default, PyROA assumes a Dirac delta transfer function. To generalise this, PyROA also allows an optional convolution between the best-fit light-curves and a model transfer function to add an additional degree of blurring (including uniform, Gaussian and log Gaussian forms). This is often necessary with PyROA to give it the flexibility to fit less densely sampled data. As such, PyROA can accommodate multiple transfer functions unlike Javelin. In this case the lag τ represents the mean time delay and a new parameter Δ_i is introduced to represent the rms of the delay distribution around the mean.

One of the major advantages PyROA has compared to the other algorithms is that it takes account of the probable underestimation of photometric error bars in AGN light-curve data. It does this by sampling the additional error parameter s_i with a uniform prior centred at zero. The original error-bars σ_i in the i^{th} input light-curve data are then inflated by adding s_i to them in quadrature $\sigma_i \rightarrow \sqrt{\sigma_i^2 + s_i^2}$. It should be mentioned that the $\frac{\sigma_i}{\sqrt{\sigma_i^2+s_i^2}}$ normalisation term in the BIC likelihood (see A.0.11) is important as it penalises the algorithm for adding too much additional error to the variance σ_{ji}^2 when the BIC is minimised. This acts to stop the algorithm from forcing a bad fit by arbitrarily increasing the error-bars. The effectiveness of PyROA's scaling of the error-bars on light-curve data was tested by Donnan , F R. et al (2021) using synthetic data where it was found that PyROA tends to slightly overestimate the error-bars. This is a safe effect as it does not introduce any bias and only reduces some of the certainty in the fit thereby making

PyROA essentially unaffected by the unknown errors. For a more detailed explanation of the method used by PyROA please see Appendix A.0.2.

1.4.3 PyceCREAM

The following explanation draws heavily from Starkey et al (2016). PyceCREAM models the lagged light-curve flux at a particular wavelength band $F_\nu(\lambda, t)$ by adapting the linear response function (1.10) into a discretised, algorithmic form

$$F_\nu(\lambda, t) = \bar{F}_\nu(\lambda) + \Delta F_\nu(\lambda) \sum_{i=0}^{\tau_{max}} \psi(\tau_i|\lambda) \Delta F_x(t - \tau_i) \Delta\tau \tag{1.20}$$

where the variable component of the driving light-curve $\Delta F_x(t)$ is convolved with the normalised, dimensionless transfer function $\psi(\tau|\lambda)$ as expected. Here $\Delta F_\nu(\lambda)$ is the variable component of the spectrum and is used to scale the model variations to fit the data and $\bar{F}_\nu(\lambda)$ is the background flux.

Of the three algorithms discussed, PyceCREAM has the strongest considerations for the thin disc model of Shakura & Sunyaev (1973) described in Section 1.1.2 for accretion disc RM. PyceCREAM does this by allowing the use of a physically motivated accretion disc transfer function derived from the classic thin disc model based on Eq. (1.12). This means that $\psi_\nu(\tau)$ is a function of $M\dot{m}$ and inclination i. By taking account of the inclination and azimuth, PyceCREAM enables the use of the more physically correct lag expression for accretion discs Eq. (1.11). By default PyceCREAM assumes a classic thin disc ($\beta = \frac{4}{3}$) orientated face-on ($i = 0$). As shown in Figure 1.5, an incorrect value for i should have no effect on the mean lag $\langle\tau\rangle$ derived and should only produce misshapen delay distributions. It should be mentioned that for emission line light-curves, PyceCREAM uses a top-hat transfer function for $\psi(\tau)$ like Javelin.

For accretion disc RM, PyceCREAM also incorporates the lamp-post model by inferring the shape of the lamp-post driving light-curve during its fitting procedure. This is in stark contrast to PyROA and Javelin which make no accommodation for the lamp-post and instead treat the shortest wavelength input light-curve as the driving light-curve. PyceCREAM attempts to infer the shape of the 'true' driving light-curve from the data by expressing the driving light-curve as a Fourier time series.

To perform the fit, PyceCREAM samples posterior distributions for the fitting parameters S_k, C_k (which are the Fourier coefficients), cos$i$, log$M\dot{m}$, logΔF_ν and log$\bar{F}_\nu(\lambda)$

using an MCMC sampler. During the fitting procedure, PyceCREAM uses a bayesian statistic called the Badness of fit (BOF) which the MCMC sampler attempts to minimise. Uniform priors are chosen for cos$i$ to reflect the assumption that the accretion disc is randomly orientated in the sky. Likewise uniform priors are chosen for log$M\dot{m}$, logΔF_ν and log$\bar{F_\nu}(\lambda)$ to express a lack of knowledge for these parameter values. Particular Gaussian priors are chosen for the Fourier coefficients due to the tendency of the algorithm to overfit with uniform priors (see A.0.2). The full set of fitting parameters and their priors are summarised in Table 1.1 which is derived from Starkey et al. 2016.

Parameter	Number of Parameters	Prior
S_k and C_k	$2N_k$	Gaussian with $\langle S_k \rangle = \langle C_k \rangle = 0, \langle S_k^2 \rangle = \langle C_k^2 \rangle = \sigma_k^2$
cos$i$	1	Uniform
log $M\dot{M}$	1	Uniform
log ΔF_ν	N_λ	Uniform
log $\bar{F_\nu}(\lambda)$	N_λ	Uniform

Table 1.1: A table outlining the parameters fitted by pyceCREAM adapted from (Starkey et al, 2016). The table shows the parameter (first column), the number of these parameters (second column) and the prior on the parameters (third column).

The parameter space is significantly larger for PyceCREAM than for Javelin and PyROA owing predominantly to the $2N_k$ lots of Fourier amplitude terms S_k and C_k that need fitting to estimate the driving light-curve. This slows down PyceCREAM's performance relative to the other two algorithms. To produce the posterior distributions for these parameters PyceCREAM uses the S_k and C_k parameters, subject to the priors in Table 1.1, to generate the driving light-curve for each iteration of the MCMC sampler. The driving light-curve is then used to generate fits for the lagged light-curve data sets at each λ using Eq. (1.20) and the logΔF_ν and log$\bar{F_\nu}(\lambda)$ parameters. The transfer function is similarly generated using the parameters cos$i$ and log$M\dot{m}$. For a more detailed explanation of the technique used by PyceCREAM please see Appendix A.0.2.

CHAPTER 2

Comprehensive Comparison of RM Algorithms

In this section we provide a comprehensive comparison of the three most commonly used RM algorithms: Javelin, PyceCREAM and PyROA. As far as we know this will be the first study to directly compare the performance of these algorithms on real observational data. This is especially true for PyROA which, at the time of writing, is a recent algorithm and is therefore largely untested on real astronomical data. A comparison of the performance of these algorithms should help inform future RM campaigns about their relative strengths and limitations and therefore help observers select software more appropriate for their analysis. To assess their performance we tested the algorithms on published, high quality RM data-sets for the object NGC 4151.

It is important to run several algorithms on a given data-set to ensure that any bias in the results as a result of limitations or assumptions made in particular algorithms can be identified. It is clear from Section 1.4 that the RM algorithms discussed operate using very different methods meaning our comparison will be useful as it will help to indicate how dependent the results are on the methods of the specific algorithms used. In addition to this our comparison uses data-sets spanning all RM regimes meaning we will help to get an indication of how each algorithm performs in each regime. This will be particularly interesting for PyceCREAM in the accretion disc regime.

2.1 The Data

To compare the performance of the algorithms in all three RM regimes, RM studies spanning the accretion disc, BLR and torus were selected. For accretion disc RM the Edelson et al (2019) study was selected. This campaign made observations spanning the UV and optical from 1928$\mathring{A}$ to 5468$\mathring{A}$ monitoring the W2, M2, W1, U, B and V bands. For BLR RM the De Rosa et al (2018) study was selected. This study collated primarily spectroscopic observations and was supplemented with photometric observations. We selected the 5100$\mathring{A}$ continuum data as the accretion disc light-curve and the Hβ emission line data as the BLR light-curve. For infrared RM of the torus the Koshida et al (2014) study was selected. We selected the V band light-curve as the accretion disc continuum and the K band light-curve as the torus emission as they were the shortest cadence data sets obtained. The key information of each of these data-sets for NGC 4151 is summarised below in Table 2.1. As can be seen, each data-set is high quality being comprised of short cadences and long observing periods relative to their expected lags. It should be

Study	Type of RM	Mean cadence (days)	Duration of campaign (days)	Expected lag (days)
Edelson et al 2019	Accretion disc	0.249	69.245	$0.96^{+0.51}_{-0.50}$
De Rosa et al 2018	BLR	0.899	128.285	$6.50^{+0.99}_{-1.39}$
Koshida et al 2014	Torus	5.520	211.620	$53.90^{+1.7}_{-2.4}$

Table 2.1: A summary of the properties of the data-sets used in the investigation for NGC 4151. The mean cadence and campaign duration is averaged over the filters used in each data-set. The expected lag is taken from the CCF analysis done in the respective studies. The values for Koshida et al (2014) are taken from the first observing epoch and the mean differential lag for the Edelson et al (2019) data is taken with respect to the V band.

mentioned that observations for NGC 4151 in Koshida et al (2014) were made over eight separate observing epochs. The following analysis is done with the first observing epoch only. Koshida et al (2014) also performed subtraction of the accretion disc contamination of the K band with different assumptions for the power law scaling parameter α_ν in the expected thin-disc relation $f_\nu \propto \nu^{\alpha_\nu}$. For the following analysis, we use the standard $\alpha_\nu = \frac{1}{3}$ estimates.

The following analysis used the shortest wavelength input light-curve as the driving light-curve for Javelin and PyROA, namely the W2, V and 5100$\mathring{A}$ continuum bands for the Edelson et al (2019), Koshida et al (2014) and De Rosa et al (2018) data-sets respectively. The lag estimates are defined as the 50^{th} percentiles of the posterior distributions and

the upper and lower uncertainties as the 84^{th} and 16^{th} percentiles respectively ran with 10,000 iterations for the MCMC sampler.

2.2 Analysis and Results

2.2.1 Javelin

Table 2.2 shows the differential lag estimates obtained in the three RM regimes by Javelin, PyROA and PyceCREAM as well as the ICCF (Peterson et al. 1998) methods used in De Rosa et al (2018) and Edelson et al (2019) and the CCF methods used in Koshida et al (2014).

Data-set	Filter	Differential Lag Estimate (days)			
		Javelin	*PyROA*	*PyceCREAM*	*Cross-Correlation*
Koshida et al 2014	K	$56.47^{+1.19}_{-6.91}$	$45.08^{+1.04}_{-1.07}$	$48.60^{+0.77}_{-0.40}$	$53.90^{+1.70}_{-2.40}$
De Rosa et al 2018	Hβ	$6.61^{+1.03}_{-0.94}$	$6.86^{+0.24}_{-0.24}$	$6.03^{+0.72}_{-0.54}$	$6.50^{+0.99}_{-1.39}$
Edelson et al 2019	M2	$0.485^{+0.608}_{-0.314}$	$0.080^{+0.070}_{-0.050}$	$0.094^{+0.156}_{-0.128}$	$0.055^{+0.248}_{-0.239}$
	W1	$0.902^{+0.852}_{-0.537}$	$0.110^{+0.090}_{-0.070}$	$0.203^{+0.183}_{-0.149}$	$-0.011^{+0.251}_{-0.264}$
	U	$1.547^{+0.585}_{-0.560}$	$0.450^{+0.110}_{-0.130}$	$0.490^{+0.242}_{-0.206}$	$0.679^{+0.239}_{-0.239}$
	B	$2.003^{+0.957}_{-0.605}$	$0.390^{+0.180}_{-0.350}$	$0.830^{+0.326}_{-0.272}$	$0.877^{+0.326}_{-0.352}$
	V	$1.282^{+1.424}_{-0.871}$	$0.440^{+0.270}_{-0.310}$	$1.270^{+0.412}_{-0.359}$	$0.960^{+0.505}_{-0.497}$

Table 2.2: A summary of the lag estimates and uncertainties obtained by Javelin, PyROA and PyceCREAM along with cross-correlation analysis for NGC 4151. The data-sets used are Koshida et al (2014), De Rosa et al (2018) and Edelson et al (2019) and the differential lags are determined with respect to the V, 5100$\mathring{A}$ continuum band and W2 bands for each data-set respectively. Here the lag estimates obtained by cross-correlation methods are taken straight from the above studies and are defined as the peak of the cross-correlation functions derived. These results were derived using PyROA's Dirac delta transfer function and PyceCREAM's accretion disc transfer function.

The Javelin lag estimates generated good light-curve fits with narrow distributions for the torus and BLR regimes indicating good convergence. An example of the light-curve fit obtained for the De Rosa et al (2018) data-set is shown in Figure 2.1 and the remaining fits are shown in Figures B.2 and B.3. It should be mentioned that when Javelin is run with its default settings, allowing the MCMC sampler to explore the full parameter space, it has a tendency to generate messy distributions with multiple peaks. An example of the posterior lag distribution obtained for the De Rosa et al (2018) data-set with an unconstrained MCMC sampler is shown in Appendix Figure B.1 which had two large 'alias' peaks. These arise due to the limited cadence and finite duration of the light-curve data. The RM algorithm will always find a fitting solution by shifting the lagged light-curve into

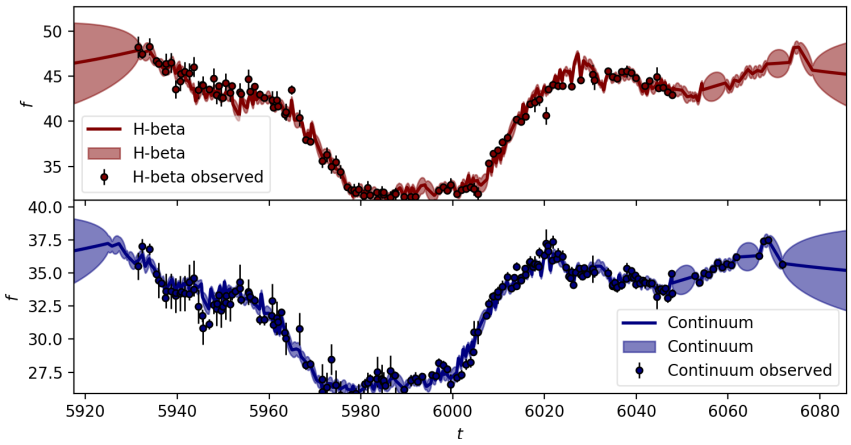

Figure 2.1: Javelin fits obtained for the 5100$\mathring{A}$ continuum and Hβ light-curves for NGC 4151 from De Rosa et al (2018). Flux units are in mJ

the two data gaps at the extremities of the light-curves where there is no data present to object to the fit. These aliasing errors therefore exist for all finite time series and so Javelin's susceptibility to them is not a unique flaw.

To deal with the issue of aliasing, Javelin allows the user to impose hard boundaries on the lag parameter space explored by the MCMC sampler. By fixing the MCMC sampler to only explore lags within the time duration of the light-curve data, most aliasing can be removed provided there are no significant data gaps within the observing period. PyROA and PyceCREAM have similar solutions to aliasing by allowing the user to specify uniform priors on the lag parameters. However, Javelin often requires lag-limits narrower than those needed to address the problem of aliasing in order to obtain more constrained lag distributions. To generate Figure 2.1, limits to the lag space between 0-10 days were imposed. This is due to a tendency found during our investigations for Javelin to occasionally produce under-constrained fits with characteristic wide, flat distributions. This is demonstrated later in the thesis for the lag distribution obtained for 3C 273 in Figure B.13. This is likely a consequence of the fact that Javelin bases its fit on a Gaussian Process which, as a non-parametric process, can incorporate an arbitrarily large number of effective parameters into its fit (see Wang, J, 2020). This can make Gaussian Processes' susceptible to forming overly flexible fits (in the case of Javelin, by shortening the decorrelation timescale τ_d and broadening the variability magnitude $\hat{\sigma}$). This weakness in the algorithm was mentioned previously in Section 1.4.2 and motivates the preliminary correction step described above which mitigates the problem.

A subtle consideration that Javelin does not take into account is the fact that the

stated photometric error-bars present in input light-curve data is likely underestimated. This is due to the likely presence of unaccounted systematic error introduced by physical effects both known (e.g. induced aperture effects in the spectra, see Yu Z. et al 2020) and unknown which are very difficult to account for in the error analysis. Javelin does not leave room for these effects and uses the unchanged input error-bars in its fit. Underestimating the error-bars could have a significant effect on the fit as having larger error-bars gives the algorithm more flexibility to fit the data. In order to test the sensitivity of Javelin's lag estimation to the size of the error-bars, we incrementally increased the scale of the error-bars for the De Rosa et al (2018) data-set for NGC 4151 and observed Javelin's associated estimate for the lag. The results are shown in Figure 2.2.

Javelin's lag estimate was found to be remarkably consistent as the errors were increased,

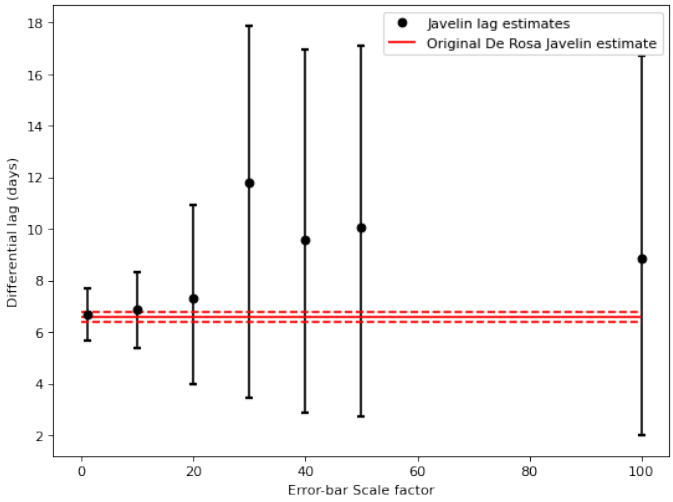

Figure 2.2: Posterior lag distributions obtained by Javelin for the 5100$\mathring{A}$ continuum and Hβ light-curves for NGC 4151 from De Rosa et al (2018). Here the MCMC sampler is allowed to explore the full parameter space.

requiring the error-bars to be $\sim \times 20$ their original value to get a value outside the uncertainty on the original estimate. As such, the result indicates that the scale of the error-bars on light-curve data has little effect on the lag estimation of Javelin. Javelin's stability to large increases in the error-bars is an advantage as it means the algorithm is little effected by the unknown error despite the fact it doesn't take account of it. However, as the error-bars were scaled, the uncertainty on the lag estimate increased and became asymmetric as the error-bars became large which is an undesirable effect. This indicates that underestimation of the error-bars is likely having a significant effect on the error analysis on the lag estimate for Javelin. Similar observations were made by Edelson et

al (2019) who observed that Javelin returned uncertainties ~ 2.5 times smaller than the cross-correlation techniques used.

2.2.2 PyROA

For the analysis on the De Rosa et al (2018) and the Koshida et al (2014) data-sets, PyROA was used with its default Dirac delta transfer function which assumes an equal degree of blurring for each light-curve in the data-set controlled by the Gaussian window function width parameter Δ. For the accretion disc RM Edelson et al (2019) data-set, the analysis was done both with the Dirac delta and a Log-Gaussian transfer function to assess the significance of using PyROA's different transfer functions. The Log-Gaussian transfer function was selected in the expectation that it would generate more realistic lag estimates for accretion disc RM due to the fact that it enforces causality and reflects the asymmetry expected for the thin disc transfer function (1.12). The PyROA fits and lag distributions obtained for the Koshida et al (2014) results with both strong blurring (ie. wide Gaussian window function width prior $10 \leq \Delta \leq 30$) and weak blurring (ie. narrow Gaussian window function width prior $0.01 \leq \Delta \leq 10$) are shown in Figure 2.3 with the remaining fits in the Appendix Figures B.4 and B.5. We also found no significant difference between the PyROA lag estimates made on the Edelson et al (2019) data with the Log-Gaussian transfer function as shown in the Appendix B.6.

2.2.3 PyceCREAM

To perform the following analysis, PyceCREAM's accretion disc transfer function was used to fit the accretion disc continuum bands whilst the top-hat transfer function was used to fit the emission line and torus bands. For the use of the accretion disc transfer function, the default PyceCREAM parameters were used including assuming a SMBH mass $M = 1 \times 10^7 M_\odot$, a fixed mass accretion rate $\dot{m} = 0.1 M_\odot$ per year and a face-on, thin accretion disc with $i = 0$, $\beta = \frac{4}{3}$ and efficiency $\eta = 0.1$. To compare this performance to the top-hat transfer function, the analysis was repeated only with the top-hat transfer function in use. PyceCREAM outputs absolute lag estimates as opposed to differential lag estimates as it infers its own driving light-curve. To make the PyceCREAM lag estimates consistent with the PyROA and Javelin results, we convert PyceCREAM's absolute lag estimates to differential lag estimates with respect to the lag of the shortest wavelength input filter. The PyceCREAM light-curve fit for the Edelson et al (2019) data is shown

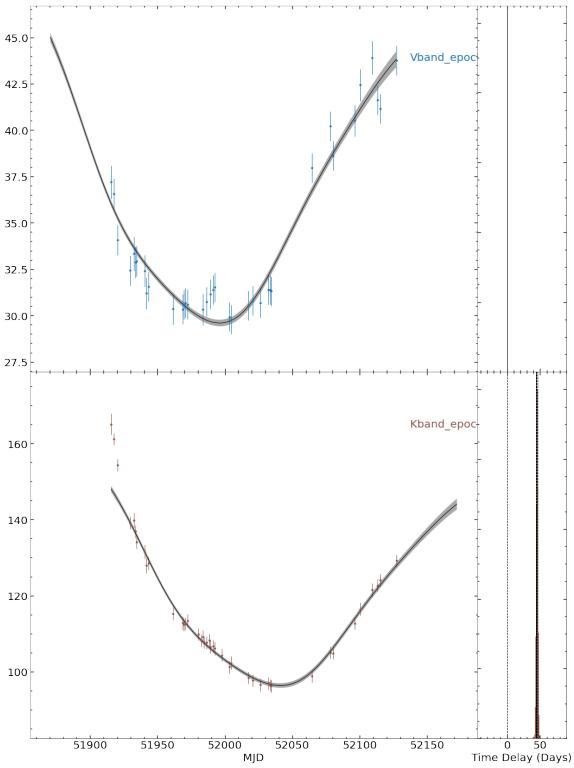

(a) PyROA fit with strong blurring prior $10 \leq \Delta \leq 30$

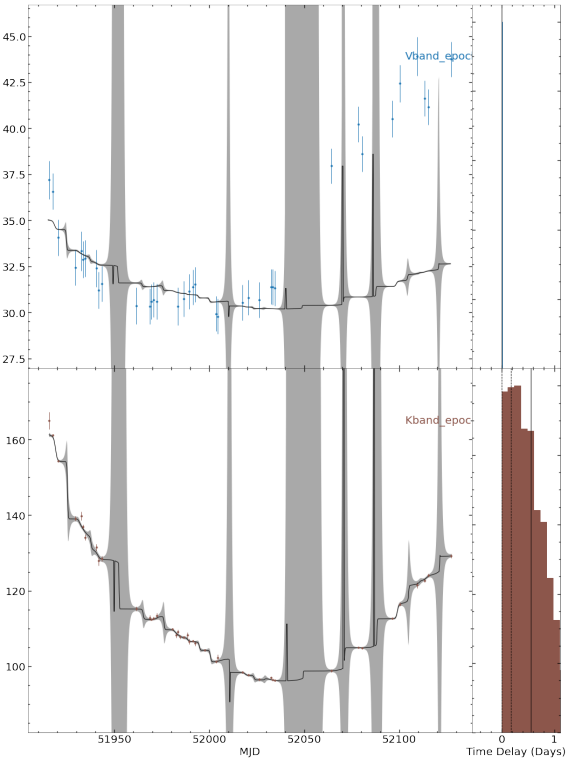

(b) PyROA fit with weak blurring prior $0.01 \leq \Delta \leq 10$

Figure 2.3: PyROA fits obtained for the V and K bands for NGC 4151 from Koshida et al (2014). Flux units are in mJ

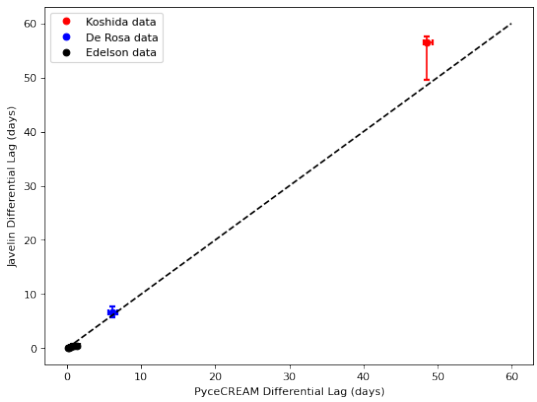

(a) Differential lag estimates for all three data-sets. Here the dashed line $y = x$ corresponds to total agreement between PyceCREAM and Javelin

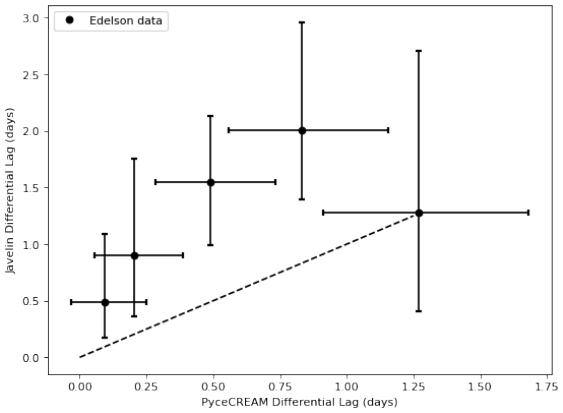

(b) Differential lag estimates for the Edelson et al (2019) data. Here the dashed line $y = x$ corresponds to total agreement between PyceCREAM and Javelin.

Figure 2.4: Differential Lag results for NGC 4151 using PyceCREAM and Javelin taken from Koshida et al (2014), De Rosa et al (2018) and Edelson et al (2019).

in Figure 2.6 with the characteristic thin accretion disc transfer functions shown. The remaining fits are in the Appendix Figures B.7 and B.8.

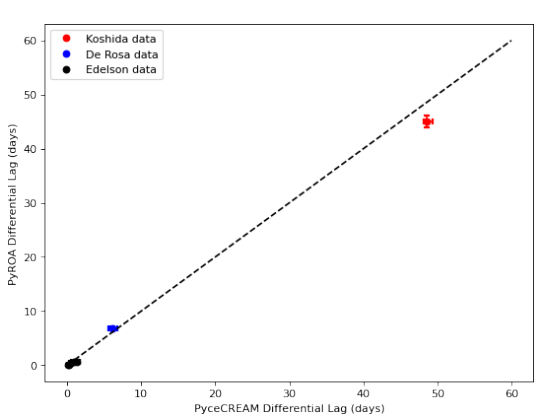

(a) Differential lag estimates for all three data-sets. Here the dashed line $y = x$ corresponds to total agreement between PyceCREAM and PyROA

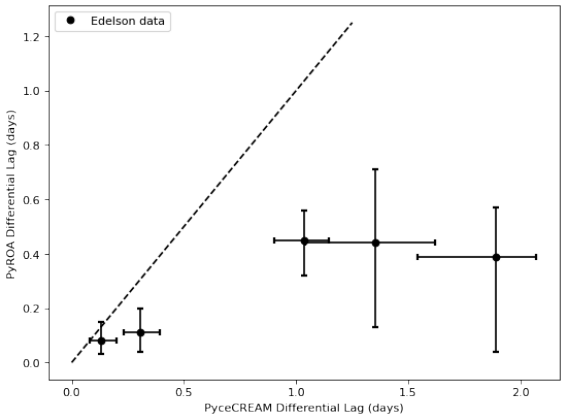

(b) Differential lag estimates for the Edelson et al (2019) data. Here the dashed line $y = x$ corresponds to total agreement between PyceCREAM and PyROA.

Figure 2.5: Differential Lag results for NGC 4151 using PyceCREAM and PyROA taken from Koshida et al (2014), De Rosa et al (2018) and Edelson et al (2019).

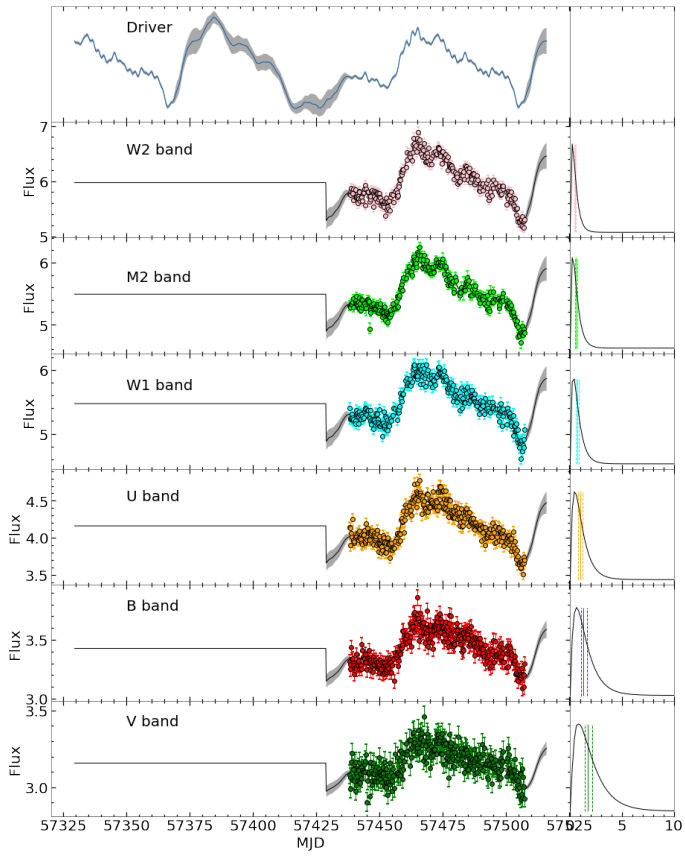

Figure 2.6: PyceCREAM fits obtained for the W2, M2, W1, U, B and V bands for NGC 4151 from Edelson et al (2019) with the accretion disc transfer function. Flux units are in mJ

It should be mentioned that when attempting to run the entire Koshida et al (2014) light-curve data for the V and K bands, PyceCREAM had a significantly longer convergence time than Javelin and PyROA. This was as a result of the long Fourier series employed by the algorithm for the long time-span Koshida et al (2014) data-set as the number of Fourier terms N_k (defined in Eq. (A.0.19)) is controlled by the recurrence time T_{rec}. This means PyceCREAM's Fourier series had to be manually truncated by setting $\omega_{high} = 0.4$.

2.3 Discussion

As shown in Table 2.2, the lag estimates obtained by the modern RM algorithms are approximately the same order as those obtained by the cross-correlation methods which indicates that the modern RM algorithms have generally good agreement with the traditional methods. We found good agreement between all algorithms in the BLR regime however Javelin overestimated with respect to PyROA and PyceCREAM in the torus and accretion disc regimes. This could be an indication that the limits we specified in the lag space were too wide, producing wide, under-constrained lag distributions extending too far into longer lags thereby biasing the estimates to be larger than expected. This is further indicated by the large uncertainties obtained by Javelin (particularly in the accretion disc regime) which were larger than the uncertainty estimates made by PyROA even though Javelin likely underestimates the photometric error-bars with respect to PyROA. Alternatively, the disagreement between Javelin and PyROA in the torus regime could be attributed to the difficulties encountered by PyROA in interpolating across the relatively poor cadence in the Koshida et al (2014) data (which had an average cadence $\sim 10\%$ of the lag). To allow PyROA to more easily interpolate across the gaps, and avoid the over-fitting seen in Figure 2.3(b), we increased the prior on the width of the Gaussian window function to $10 \leq \Delta \leq 30$ days to create a more strongly blurred fit in Figure 2.3(a). This may have decreased the accuracy in the lag estimation due to the smoother fit being less sensitive to shorter timescale variability in the data.

The erroneous fit produced by PyROA in Figure 2.3(b) used the default Gaussian window function uniform prior width $0.01 \leq \Delta \leq 10$ days for the Dirac delta transfer function and indicates some over-fitting of the data which resulted in a lag estimate strongly biased towards zero days. Over-fitting would result in the model fitting noise inherent in the data-set which would be expected to bias the lag estimate towards zero as white noise

time series would become indistinguishable from each-other. The over-fitting is likely a consequence of the relatively poor cadence present in the Koshida et al (2014) data-set which provided PyROA with a large incentive to over-fit the data in order to minimise the BIC by minimising the χ^2 term so as to compensate for the large regions of the fit lacking data. As is clear from Eq. (A.0.11) and (A.0.13), the number of effective parameters (which determines the smoothness of the fit) is controlled by the Gaussian window width Δ. In this case the default prior for the Gaussian window width $0.01 \leq \Delta \leq 10$ was too small for the Occam's razor term in the BIC to provide much resistance in encouraging a smoother fit. The susceptibility of PyROA to over-fitting compared to Javelin and PyceCREAM is likely due to the differences in their fitting techniques. Javelin and PyceCREAM both fit models of AGN variability to the data (ie. a DRW and the thin disc model respectively) whilst PyROA fits the data directly (essentially using a weighted mean). As such, PyROA may be more prone to over-fitting poorly sampled data. Our results suggest that the correction for over-fitting in PyROA is to increase the degree of blurring in the fit.

The worst agreement between the algorithms was found in the accretion disc regime as seen in Figures 2.4, 2.5 and Appendix B.6. This may be as a result of the poor suitability of the Dirac delta and top-hat transfer functions used by PyROA and Javelin in the accretion disc RM regime. Javelin uses the top-hat transfer function to offset the complexity introduced into the fitting procedure by the presence of inverse matrices in the fit (evident in Eq. A.0.6) to run a so-called 'fast method' (see Rybicki, G. B. & Press, W. H. 1995). Javelins dependence on this 'fast method' improves its functionality but hampers the physical meaningfulness of its model. This can be expected to be most significant for accretion disc RM where a physically motivated transfer function can be derived from (1.12) which, as shown in Figure 1.5, is characterised by an asymmetric shape fundamentally different to the top-hat.

Interestingly, PyROA showed no significant difference in the lag estimates obtained by the Dirac delta transfer function and the more physically meaningful Log-Gaussian transfer function for the Edelson et al (2019) data as seen in Figure B.6. In addition, we found no significant change in the PyceCREAM lag estimates between using the accretion disc and top-hat transfer functions. This makes it unlikely that the inconsistencies in the lag estimates made by Javelin and PyROA with respect to PyceCREAM in the accretion disc RM regime is due to the inconsistencies of their transfer functions with

the expected thin accretion disc transfer function. It also indicates that the increased versatility of PyROA through being able to accommodate multiple transfer functions is not very significant. Instead, the difference is likely due to the fact PyceCREAM infers a driving light-curve whilst PyROA and Javelin must assume that the shortest wavelength input light-curve is the driver (in this case the W2 band). This would also explain the fact PyceCREAM overestimated the lags for the Edelson et al (2019) data with respect to the PyROA results. By assuming the driving light-curve, which originates from near the centre of the disc, occupies the W2 band, PyROA would estimate smaller accretion disc sizes than PyceCREAM which makes the more physically reasonable assumption that the driving light-curve is in the X-ray band and therefore the W2 emitting region of the disc exists at larger distances from the SMBH.

Naively, we would expect that PyceCREAM would give the most accurate lag estimates in the accretion disc RM regime due to its strong considerations for the thin disc model. This is also suggested by the greater consistency between the PyceCREAM and ICCF results compared with Javelin and PyROA. The markedly better performance of Javelin and PyROA in the BLR and (to some extent) the torus regimes indicates that the lack of ability by these algorithms to infer driving light-curves is less significant on these larger scales where the continuum emission from the accretion disc as a whole can be well approximated as a driving light-curve.

2.4 Summary

In this chapter we set out to compare the performance of the RM algorithms Javelin, PyceCREAM and PyROA on the same high-quality, published data-sets spanning all three RM regimes. This is with the intention of informing future RM campaigns on the suitability of the algorithms in each RM regime and the significance of their limitations.

- All lag estimates were consistent in the BLR regime but were inconsistent in the other regimes. The largest disagreement was in the accretion disk regime which we attribute to PyceCREAM's unique ability to infer its own driving light-curve which would have the most significant effect on these smaller length scales.

- The disagreement between Javelin and the other two algorithms is likely a consequence of Javelin returning under-constrained fits. The disagreement in the torus regime may also be attributed to the difficulties faced by PyROA in interpolating

over the large cadence.

- No significant difference was found in lag estimates made by PyROA and PyCeCREAM using different transfer functions.

CHAPTER 3

Accretion disc Reverberation Mapping for 3C 273 and 1H 2106-099

In this section the results of the first accretion disc RM campaigns on the AGN 3C 273 and 1H 2106-099 are analysed and discussed. The results of this analysis are of scientific importance as it will be the first time RM is used to probe the accretion disc structure of these two AGN. In particular, 3C 273 is of historical importance due to its role as the first discovered quasar and has been heavily observed since its discovery meaning the unique insights provided by this study will be a valuable addition to the wealth of literature on this object. Conversely, the relative lack of previous observational data on 1H 2106-099 makes this study valuable as it will be (as far as I know) the first in-depth insight into the accretion disc structure of this object. Obtaining insight into the structure of the accretion discs of these objects is of physical significance as it will indicate how well they each conform to the thin disc model. Differences between the results of this analysis and the expected thin disc relationship will be significant as it could indicate new accretion disc physics. In addition, the scale of the obtained lag measurements relative to the predicted values could provide insight into the commonly observed 'accretion disc size problem'.

As a result of the analysis carried out below, we also hope to make lag predictions for the JHK near-infrared bands for both objects which can be tested by future near-infrared RM campaigns. For 3C 273, there is also discussion in the literature about the significance of the jet emission in the optical spectrum. Therefore, a secondary aim of the RM analysis on this object is to address this with new data. In addition to its

scientific importance, this investigation (as far as I know) will be the first time PyROA, PyceCREAM and Javelin have all been run on new RM data meaning it will serve as a unique comparison of the relative performance of these algorithms. The result of these comparisons should be of practical importance for informing future RM campaigns. The analysis done in this chapter is part of a planned publication. For the following analysis, we assume cosmological parameters $H_0 = 70 \mathrm{km} s^{-1} \mathrm{Mp} c^{-1}$, $\Omega_m = 0.3$ and $\Omega_\lambda = 0.7$.

3.1 Target Selection

3C 273 was selected for this study as it is the brightest nearby quasar which previous studies (e.g. Sturm et al 2018; Kaspi et al 2000) have found to have large total length scales making it an attractive target for accretion disc RM. During the course of observations, well structured light-curves for the AGN 1H 2106-099 were also obtained thereby meriting its inclusion into this study. 3C 273 and 1H 2106-099 have very different properties to each other with 3C 273 existing as a more distant, more luminous Quasar than the Seyfert 1 galaxy 1H 2106-099. In addition, 3C 273 possesses a radio jet whilst 1H 2106-099 has been observed as a strong X-ray emitter. These stark differences make this study useful in comparing the accretion disc structure of different types of AGN as well as the performances of the RM algorithms in different luminosity and variability regimes. Some basic properties of both sources are summarised in Table 3.1.

Object	Redshift z	Black Hole Mass ($M_\odot$)	Bolometric Luminosity (ergs^{-1})
3C 273	0.158	8.9×10^8	$10^{46.66}$
1H 2106-099	0.027	2.3×10^7	$10^{45.10}$

Table 3.1: A summary of the properties of 3C 273 and 1H 2106-099. Here the SMBH mass and bolometric luminosity estimates are obtained from Landt et al (2011).

3.2 The Observations

The observational data for this study were obtained from the Las Cumbres Observatory (LCO) (Brown et al 2013). LCO is a global network of 25 telescopes which can provide almost continual monitoring making it uniquely well suited for time domain astronomy campaigns. Our data-set was collected by 1m telescopes containing a Sinistro camera

instrument which monitored 3C 273 in the Bessell UBV filters, the SDSS g', r', i' filters and the Pan-STARRS zs filter. The source 1H 2106-099 was similarly monitored in the Bessell U filter, the SDSS g', r', i' filters and the Pan-STARRS zs filter. This provided observational data spanning the UV to the near infrared over an observer wavelength range $3500\mathring{A} - 8700\mathring{A}$. The full light-curve data for both objects is shown in Figure 3.1 and Table 3.2 summarises the properties of the two data-sets. As can be seen, the light-curve data

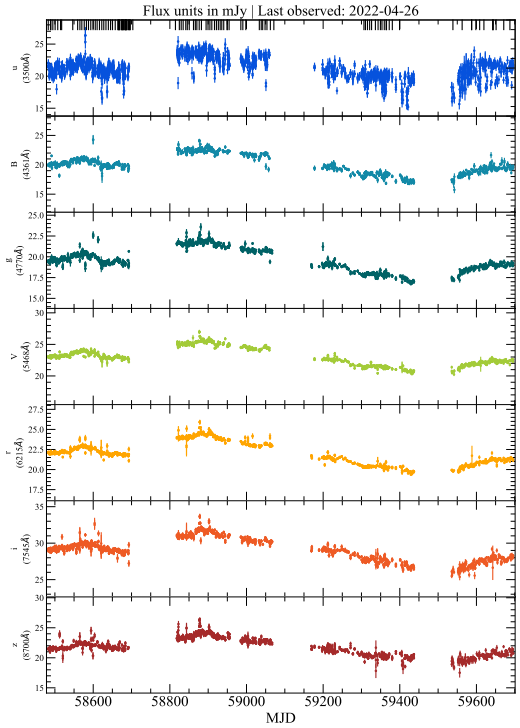

(a) The full selection of 3C 273 light-curves observed between January 2019 to April 2022.

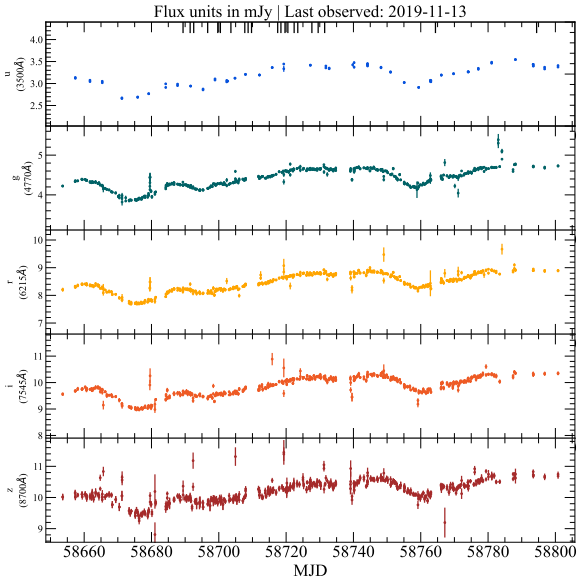

(b) The full selection of 1H 2106-099 light-curves observed between June 2019 to November 2019.

Figure 3.1: The complete light-curve data for 3C 273 and 1H 2106-099. Flux units are in mJy and wavelengths are quoted in observer frame.

Object	Mean Cadence (days)	Observing Period (days)	Number of observations
3C 273	0.583	1212.9	2096
1H 2106-099	0.553	146.4	491

Table 3.2: A summary of the properties of the 3C 273 and 1H 2106-099 light-curve data. The values are averaged over each of the filters.

obtained in this investigation is very high cadence (with $\sim 75\%$ of the 3C 273 data and $\sim 50\%$ of the griz 1H 2106-099 data having mean cadences of less than five minutes) and spans long observing periods relative to the expected lags of the order of days to weeks.

Figure 3.2 shows the optical and near-infrared spectrum of 3C 273 taken from Landt et al (2011) in rest frame wavelength. Included are the LCO filter wavelength centroids and widths used to monitor 3C 273 in our campaign in order to give an indication of the parts of the spectrum sampled by our light-curves. It should be mentioned that the observed down-turn in the flux at the UV end of the spectrum is simply a feature of the diminished sensitivity of the spectrograph in this wavelength regime. Table 3.3 shows the estimated contamination levels by the BLR and radio jet for the accretion disc flux at each of the LCO filters. This revealed only significant contamination levels for the V

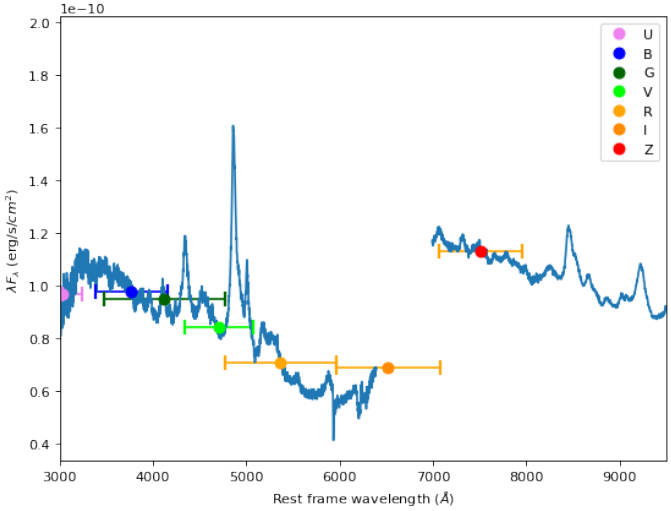

Figure 3.2: Optical and near-infrared spectrum of 3C 273 taken from Landt et al (2011). Shown are the filter centres and widths used to obtain our light-curve data.

Filter	Percentage Contamination
B	2%
G	7%
V	23%
R	9%
Z	28%

Table 3.3: Estimates of the optical and near-infrared contamination for each of the filters used to monitor 3C 273. Here the I band contamination will be dominated by the strong Hα emission line expected to occupy the spectral gap although estimates cannot be obtained due to the gap.

and Z bands although this appears to have had no noticeable effect on the RM results. It should be mentioned that the contamination levels were estimated assuming the LCO filters were equally sensitive across their entire width. This is unlikely as we would expect the sensitivity to diminish towards the edges of the filter width meaning the contamination

estimates in Table 3.3 are upper limits. The source of the V band contamination is the strong Hβ broad emission line evident in Figure 3.2. The Z band contamination likely originates from the jet which we think is likely contaminating the I band at similar levels and is probably the cause of the small bump at $\sim 7400\mathring{A}$ seen in Figure B.9. The I band filter for 3C 273 is also expected to be strongly contaminated by the Hα line visible in the spectrum of 1H 2106-099 in Figure 3.3 which would be located within the spectral gap for 3C 273 due to its larger redshift.

Figure 3.3 shows the optical and near-infrared spectrum of 1H 2106-099 taken from Landt et al (2011) in rest frame wavelength along with the LCO filter wavelength centres and widths. Table 3.4 shows estimates for the contamination levels in each of the measured photometric bands. This revealed significant contamination levels in all filters due to the characteristically strong emission lines in 1H 2106-099. In particular, the R band faces very strong contamination from the large Hα line. The effect this may have on the lag estimates is discussed later. A detailed explanation of our method for estimating the contamination levels using Figure B.9 and B.17 is given in Appendix B.2.1.

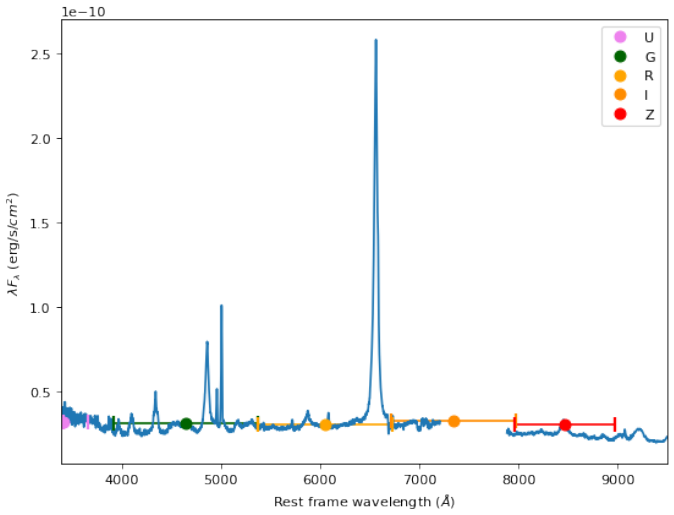

Figure 3.3: Optical and near-infrared spectrum of 1H 2106-099 taken from Landt et al (2011). Shown are the filter centres and widths used to obtain our light-curve data. The strong Hα line is evident.

Filter	Percentage Contamination
U	10%
G	22%
R	75%
Z	21%

Table 3.4: Estimates of the optical contamination for each of the filters used to monitor 1H 2106-099

3.3 3C 273

3.3.1 Theoretical lag estimates

To get an indication of the expected form of the spectrum in 3C 273, we generated simulations of the accretion disc spectrum expected from the thin disc model. An example of the obtained spectrum is shown in Figure 3.4. As can be seen the spectrum is peaked in approximately the short wavelength UV as expected and mimics the standard black-body shape, trailing off at larger radii which are expected to be cooler and therefore emit at lower fluxes and longer wavelengths. The simulation also shows the effect of including/excluding the boundary condition in Eq. (1.4). As expected, the two solutions approach one another for $r >> r_{ISCO}$ but there is significant differences at smaller radii. In particular, without the boundary condition the spectrum is non-zero below r_{ISCO} which is unphysical. The

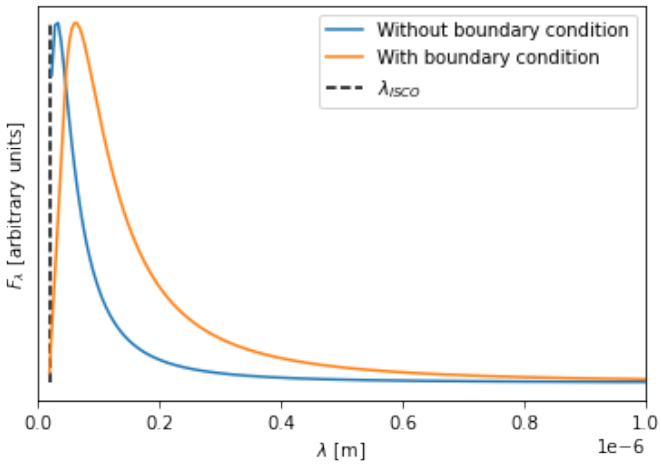

Figure 3.4: A simulation of the expected spectrum for the quasar 3C 273 generated using the thin disc model. Fits with and without the boundary condition are shown. For more information on how this spectrum was generated please see Appendix B.2.2.

simulation was built using Plancks function with the thin disc temperature-radius relation

Eq. (1.4) and Wien's law defined as

$$\lambda_{max} = \frac{hc}{k_B X T}. \tag{3.1}$$

Here h is Planck's constant, k_B is Boltzmann's constant, c is the speed of light and X is a dimensionless scale factor which we set at the standard value $X = 4.96$. See Appendix B.2.2 for a detailed description of how we designed the simulation. Our use of the standard X value may limit the realism of the simulation (see below). In addition, the physical meaningfulness of the simulation will be hampered by the assumption that the entire spectrum of the accretion disc is Planckian. This assumption is likely to be problematic for the inner accretion disc where Compton scattering is expected to be dominant but is probably acceptable for the optical part of the spectrum observed by our study. The simulation was ran with and without the boundary condition term in the thin disc model relation Eq. (1.4).

Figure 3.5 shows the expected spectral locations of the centroid wavelengths of the LCO filters used to monitor 3C 273 in our campaign plotted onto our thin accretion disc simulation. By re-plotting this into a logarithmic form over the spectral range investigated in this campaign, estimates for the accretion disc power law scaling factor β can be obtained using the thin accretion disc relation $\log\lambda F_\lambda \propto \beta \log\lambda$. The expected values of β from the simulation, both with and without the boundary condition term, are presented in Table 3.5. As can be seen, both simulated values are close to the theoretical value of $|\beta| = \frac{4}{3}$. Here, the small difference can probably be attributed to the relatively low resolution of the simulation although a slightly shallower value is expected from the unapproximated simulation as the boundary condition shifts the spectrum peak to longer wavelengths leading to a shallower descent.

Figure 3.6 shows a real logarithmic spectrum taken from Landt et al (2011) for 3C 273. Here the near infrared spectrum has been normalised around the $1\mu m$ wavelength as done in Landt et al (2011). A linear fit is done to the spectrum as shown which generated a measured power law exponent β estimate stated in Table 3.5. The linear fit and uncertainty was determined by scipy 'curve-fit' module. This measured β estimate is shallower than the approximated thin disc model value $|\beta| = \frac{4}{3}$ by more than 5σ. The measured β value is more consistent with the shallower value predicted by the unapproximated thin disc model which seems to be reflected in the RM results (see below). This suggests the simulation is reasonably realistic despite its assumptions. In fact, we believe the uncer-

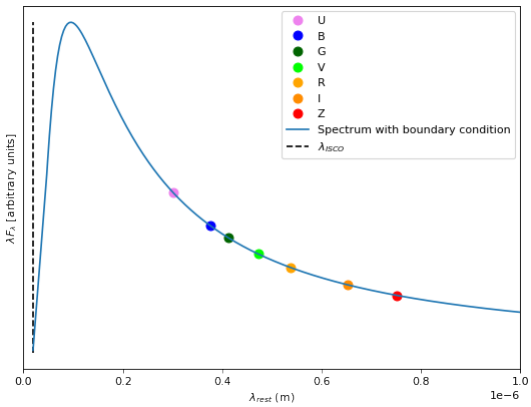

(a) Simulated spectrum with the expected location of the LCO filter rest wavelengths for 3C 273.

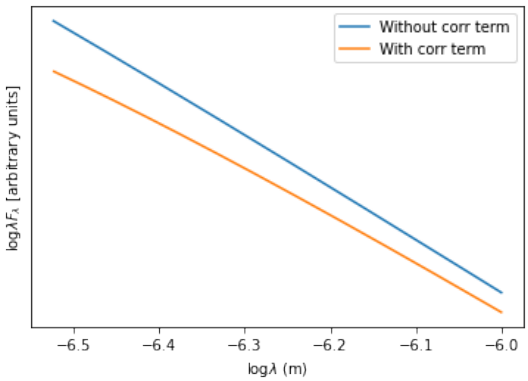

(b) Simulated spectrum for 3C 273 in logarithmic space.

Figure 3.5: Simulated accretion disc spectrum for 3C 273 in linear and logarithmic space.

tainties estimated by 'curve-fit' are likely underestimated as the algorithm did not fully account for the influence of the strong broad emission lines on the linear fit. When the linear fit is repeated allowing the broad emission lines to have a greater influence on the fit we find the uncertainty on the β estimate more than doubles to $|\beta| = 1.02 \pm 0.13$ which is now consistent with the unapproximated thin disc model simulation although the difference with the approximated thin disc value does not seem to be very significant. A more detailed spectral study of 3C 273 with a more sophisticated error analysis would be needed to confirm this result.

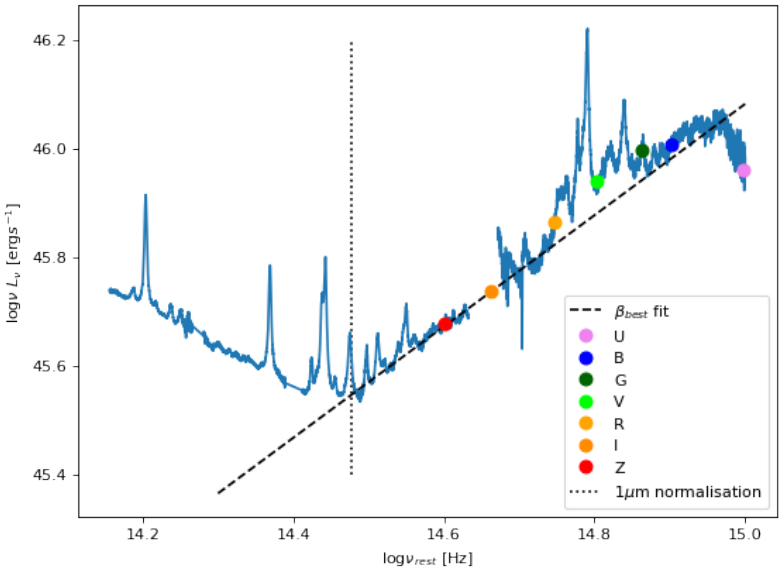

Figure 3.6: Spectrum of 3C 273 taken from Landt et al (2011) plotted in a logarithmic form. A linear function is fit which returns a measured power law exponent $\beta = 1.04 \pm 0.05$

	Spectral value	Simulated value	
		With boundary condition	*Without boundary condition*
$\|\beta\|$	1.04 ± 0.05	1.15	1.29

Table 3.5: A summary of the estimated magnitude of β values obtained from the spectral fit in Figure 3.6 and the simulations in Figure 3.5.

For the following RM analysis, predicted absolute lag estimates were derived for each of the LCO filters used to monitor 3C 273 using the thin accretion disc model. These lag predictions are included in Table 3.6. To do this, the mass accretion rate was estimated from Eq. (1.1) using the bolometric luminosity $L_{bol} = 10^{46.66}\text{erg}s^{-1}$ measured by Landt et al (2011) and the standard efficiency $\eta = 0.1$. Temperature estimates were then obtained for the regions of the accretion disc emitting at each of the LCO monitored wavelengths using Wiens law Eq. (3.1) in rest frame. This was done both with the standard value $X = 4.96$ and with estimated X values tailored to 3C 273 following the approach of Mudd et al (2018) (see Appendix B.2.3 for the derivation of the X values and an explanation of their necessity). This enabled the radial extent of each of the monitored parts of the accretion disc to be estimated using the thin disc temperature-radius relation Eq. (1.4) which was converted to a time lag estimate using Eq. (1.9) by assuming a face-on disc. For this the SMBH mass in Table 3.1 was used and a Schwarzschild black hole was assumed meaning $r_{ISCO} = 3r_g$. The lag estimates were obtained with the inclusion of the boundary condition term because the simulation Figure 3.3 indicated a significantly different accretion disc emission behaviour in the optical without it.

Filter	Lag Prediction (days)	
	$X = 4.96$	X_{new}
U	8.85	8.92
B	12.00	10.54
G	13.57	11.46
V	16.37	13.09
R	19.50	15.06
I	25.40	18.66
Z	30.83	22.04

Table 3.6: Absolute lag predictions for the regions of the accretion disc in 3C 273 emitting predominantly in each of the LCO filters. Two sets of predictions are obtained using the standard $X = 4.96$ and a new set of X values derived following the approach of Mudd et al (2018).

3.3.2 Algorithm results

As can be seen in Figure 3.1(a), the light-curve for 3C 273 was divided into four distinct observing epochs due to seasonal interruptions in the campaign. To obtain more accurate lag estimates, we decided to analyse the epochs separately so as to remove the large data gaps from the light-curve fits (which Chapter 4 indicates could increase the uncertainty of lag estimation). A clear long timescale trend can also be seen in the light-curve which has also been detected by previous campaigns (e.g. Zhang et al 2019). Linear detrending was done to the third and fourth epochs in Figure 3.1(a) by subtracting fitted linear polynomials from the data in order that any biasing effects on lag estimation could be removed. This could not be done satisfactorily for the first and second epochs due to their non-trivial trends. Linear detrending was unnecessary for the use of Javelin but was still done for the sake of consistency with the rest of the analysis. The U band data-set in Figure 3.1(a) was also excluded from the following analysis due to problematic fits obtained during preliminary analysis. This is likely a result of its excessively noisy nature. For the following analysis each of the differential lag values is made with respect to the B filter which, as the shortest wavelength input light-curve, is assumed as the driving light-curve.

PyROA

The differential lag estimates and uncertainties derived from PyROA for each of the filters used to monitor 3C 273 and across all four epochs is shown in Table 3.7 which also includes the lag predictions converted into differential form. The lag estimates were obtained using the default Dirac delta transfer function with a wide Gaussian window width uniform prior $20 \leq \Delta \leq 30$ days to impose a strong degree of blurring (see below for explanation). The uniform lag prior was set at $0 \leq \tau \leq 100$ days to include up to $4\times$ the largest lag prediction in order to accomodate the potential appearance of the 'accretion disc size problem' which can inflate predicted lags up to $2-4\times$ their expected value. For each of the light-curves, the lag parameter Markov chains were initialised at the standard predicted values corresponding to the second column in Table 3.6 so as to achieve faster convergence. Ultimately there was no significant difference between the lag estimates in Table 3.7 and those obtained using the default initialisation values of 0 days. The PyROA lag estimates were obtained using 50,000 iterations in the MCMC sampler to ensure good convergence as demonstrated in the narrow distributions in Figure 3.7.

Filter	Lag Estimates (days)				Lag Prediction (days)	
	Epoch 1	*Epoch 2*	*Epoch 3*	*Epoch 4*	$X = 4.96$	X_{new}
B	0	0	0	0	0	0
G	$1.85^{+0.98}_{-0.98}$	$1.33^{+1.08}_{-0.97}$	$4.00^{+1.77}_{-1.96}$	$52.86^{+4.07}_{-6.04}$	1.57	0.92
V	$3.00^{+1.13}_{-1.02}$	$2.26^{+2.02}_{-1.60}$	$7.15^{+1.79}_{-1.84}$	$62.25^{+5.26}_{-13.67}$	4.37	2.55
R	$5.03^{+2.86}_{-0.92}$	$2.31^{+6.18}_{-1.41}$	$15.02^{+1.71}_{-2.07}$	$92.21^{+3.70}_{-6.13}$	7.50	4.52
I	$8.10^{+5.43}_{-1.07}$	$6.28^{+11.26}_{-1.64}$	$17.94^{+2.94}_{-2.37}$	$94.62^{+3.51}_{-7.21}$	13.40	8.12
Z	$9.66^{+4.76}_{-1.45}$	$6.22^{+12.80}_{-1.50}$	$33.19^{+2.09}_{-2.36}$	$98.99^{+0.77}_{-2.96}$	18.83	11.50

Table 3.7: Differential lag estimates obtained by PyROA with respect to the B band over all four observing epochs. Also included are the differential lag predictions

The fourth epoch generated unrealistically large lag estimates which is likely a result of the lack of any clear features in this epoch for PyROA to anchor onto. This would present difficulty for the fitting of this epoch and the lag estimates associated with this fit. The second epoch generated lag estimates which are consistent with the X_{new} predictions but only as a result of its large uncertainties. In addition, the distributions obtained for the second epoch had multiple peaks which indicates poor convergence. The first epoch generated reasonable lag estimates consistent with the standard $X = 4.96$ predictions at the upper end of its uncertainty limits but which are more consistent with the X_{new} lag predictions. Reasonable lag estimates were also obtained by the third epoch which, whilst inconsistent with both sets of lag predictions, are completely consistent with the commonly observed 'accretion disc size problem' where accretion disc RM campaigns regularly obtain lag estimates a factor $\sim 2 - 4$ larger than predicted. We consider the lag estimates obtained by the third epoch to be more reliable due to the fact that most of the lag distributions output by the first epoch data-set contained secondary peaks located at the approximate values of the lag estimates obtained from the third epoch. This indicates that the algorithm converged better with the third epoch data-set and that the first epoch data-set returned secondary solutions which are consistent with the third epoch lag estimates. In addition to this, our inability to detrend the first and second epochs may mean some biasing effects are present in their lag estimates (although the first epoch does appear stationary). Performing the subsequent analysis with the first epoch lag estimates returned results which are completely inconsistent with the rest of the analysis which is a further indication of its unreliability. The third epoch has the longest observing period meaning, based on our conclusion from Chapter 4, it can be expected to give the most accurate lag estimates. This appears to be the case based on the fact the relative

uncertainties obtained by the third epoch are on average smaller than the other epochs. For these reasons, the following 3C 273 analysis is done using the third epoch but with the recognition that the results from the first epoch are reasonable albeit less reliable. The fit and corner plots generated by PyROA for the third epoch are shown in Figures 3.7 and B.12 respectively. It should be mentioned that the fit in Figure 3.7 was done by initialising the lag for the Z band at its preferred lag of 30 days. This had no effect on the lag estimates but produced clearer corner plots.

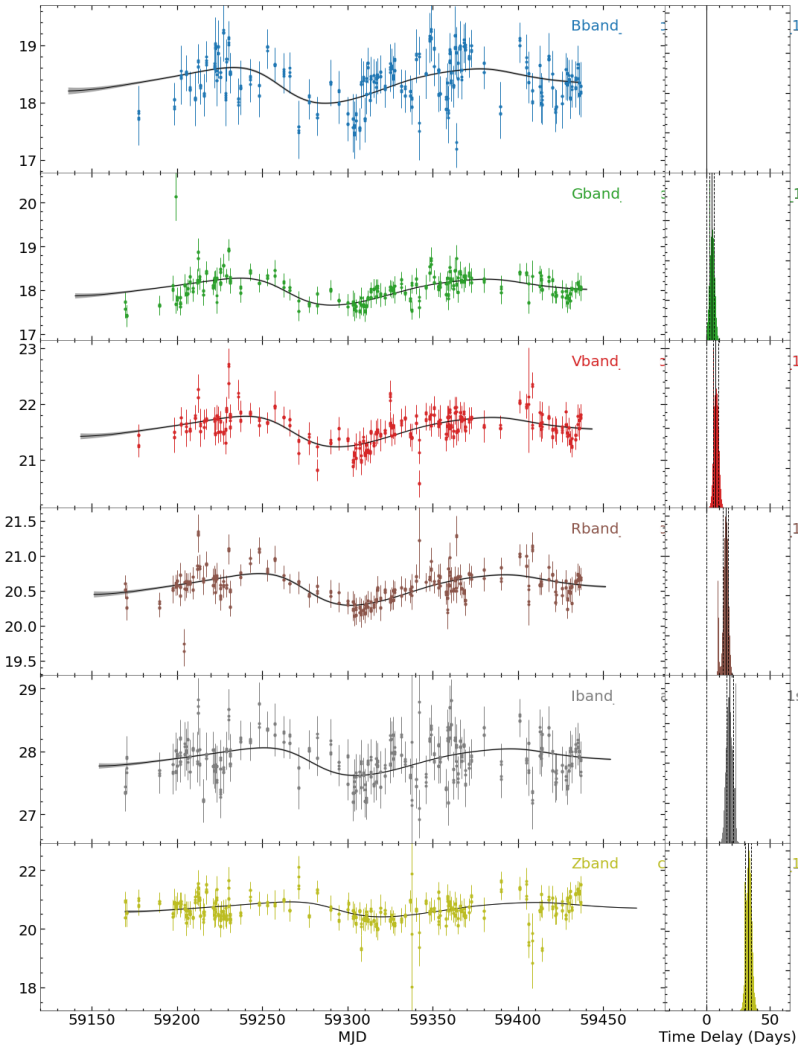

Figure 3.7: PyROA fit to the bgriz detrended, third epoch light-curves obtained for 3C 273. Flux values are in mJy.

It should be mentioned that the PyROA fits obtained in Figure 3.7 required a strong blurring prior. When the default Gaussian window width uniform prior $0.01 \leq \Delta \leq 10$ days was used, fits hugging much closer to the data were obtained which generated erroneously small inter-band lag estimates for several filters. This indicates that there is a

biasing effect present in the fits which is more significant at lesser blurring. To assess the significance of this biasing effect across the different filters, PyROA was run separately on the bgv and the riz light-curves with the Dirac delta transfer function with the default blurring prior. The lag Markov chain for each light-curve was initialised to start halfway between the alias peak and the expected peaks from Figure 3.7 to allow them equal opportunity to converge to either peak. The results for the fits are shown in Appendix Figure B.15. Interestingly, the MCMC chains for the bgv fits converged to the expected lags whilst the riz fits converged to the alias peaks. This suggests that the biasing effect is stronger for the longer wavelength filters.

A physical explanation for this biasing effect could be the presence of optical contamination from the jet emission in 3C 273. If significant, this would be expected to bias the differential lags towards zero as the jet would vary in flux almost simultaneously across its optical bands (see Ghisellini et al 2017). Paltani et al (1998) found that the optical and UV light-curve data from 3C 273 was well described by decomposing it into two components of variability. The B component is a shorter timescale variability component which dominates the UV and short wavelength optical which Paltani et al (1998) attributes to emission from the accretion disc. The R component is a longer timescale variability component which dominates the infrared and near-infrared optical which Paltani et al (1998) attributes to emission from the jet. The SED's estimated by Paltani et al (1998) for the B and R components demonstrate that the I and Z optical bands monitored in our campaign would be expected to have the strongest contamination from the jet. This could naively explain the stronger biasing effect we detected for the I and Z filters. However, Paltani et al (1998) estimated the timescale of variability for the B component as ≤ 2 years with the R component being significantly longer. In fact, estimates for the variability timescale of the R component could not be obtained as they did not measure a full period over their 10 year data-set. This means even if the R component is strongly contaminating our I and Z light-curves, as the high contamination estimates in Table 3.3 suggests, it will almost certainly not introduce any variability over the short observing period of the third epoch and so should have no real effect on the lag estimates obtained. Another possible explanation for the bias could be a result of intra-day jet variability detected in optical measurements of 3C 273 by Xiong et al (2017) which, if present in our light-curves would bias the lag estimates towards zero. However this is unlikely to be significant for reasons discussed in Appendix B.2.5.

To investigate the origin of the trend seen in our light-curve data, we fit the quasi-periodic variability with Sine functions which returned periods ~ 3 years which is much shorter than Paltani et al (1998)'s expected variability timescale of the R component but is much more similar to the estimated timescale of the B component (albeit a little longer). In fact, spectral observations of 3C 273 by Yuan et al (2022) found that the continuum accretion disc emission had quasi-periodic variability on a timescale $\sim 3.39 \pm 1.13$ years in good agreement with our trend fits. This suggests that the origin of the trends in our light-curve data is from the accretion disc which is further supported by the apparent identical trend present in our U band light-curve which should have no significant jet component. See Appendix B.2.4 for a detailed explanation of this procedure.

To investigate the behaviour of the trend across the four different epochs, the optical 3C 273 spectrum taken from Landt et al (2011) was normalised to each epoch of the photometric light-curve data in Figure 3.1(a). To do this, the spectrum was normalised to the mean flux from the B band (selected due to its low contamination estimate) and the mean fluxes of the remaining six filters were plotted onto the normalised spectrum. This was done for all four epochs. The normalised spectra obtained for the four epochs is shown in Figure 3.8. As can be seen the photometric data maps well onto the spectrum. Plotting the photometric data points into a logarithmic form using 'lmfit' allowed estimates to be obtained for the power law exponent β from the thin disc relation $\lambda f_\lambda \propto \lambda^{-\beta}$ for all four epochs. These results are shown in Table 3.8. It should be mentioned that the linear fits obtained in Figure 3.8 were done with the exclusion of the I band which is assumed to be anomalous due to the RM results and the bolometric luminosity estimates explained in the Discussion.

Epoch	β estimate
1	0.91 ± 0.09
2	0.93 ± 0.08
3	0.89 ± 0.10
4	0.96 ± 0.09

Table 3.8: Estimates for the exponent β from the thin disc power law $\lambda f_\lambda \propto \lambda^{-\beta}$ by normalising the spectrum from Landt et al (2011) around the photometric light-curve data for each epoch in Figure 3.1(a).

As can be seen the β estimates from this photometric approach are all consistent with the shallower β values estimated from the PyROA RM results (see Discussion) and the spectral fit when the uncertainties are considered and are all inconsistent with the

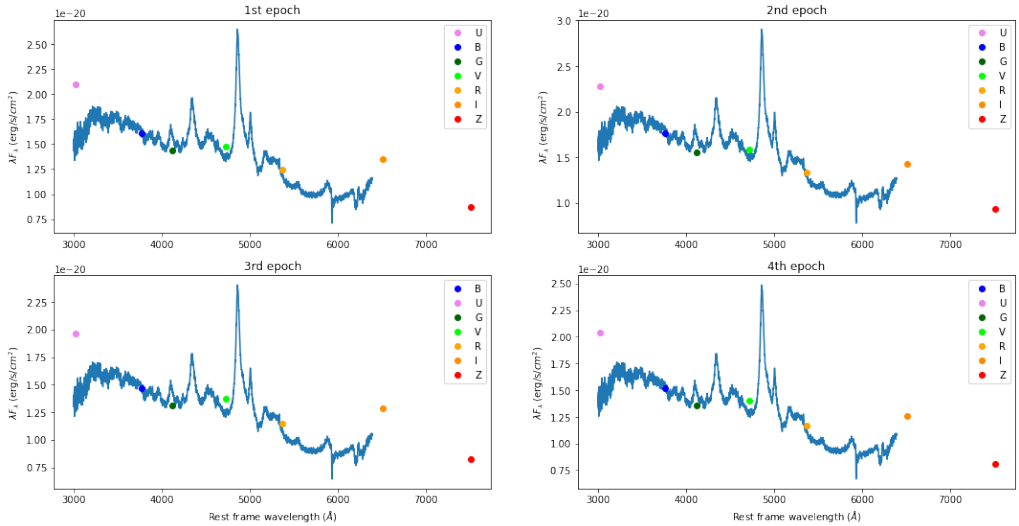

Figure 3.8: Normalising the optical spectrum from Landt et al (2011) onto our photometric light-curve data using the B band. This was done for all four epochs.

classic thin disc model value $\beta = \frac{4}{3}$ by a significant $\sim 4\sigma$ although the uncertainties are likely underestimated. Therefore, the results in Table 3.8 seem to prefer a shallower β value as obtained elsewhere in the analysis although, as before, it is not clear whether the difference with the approximated thin disk value is significant. Table 3.8 also indicates that the third epoch has the strongest jet contamination as it generated the smallest β magnitude which corresponds to the greatest 'redder when brighter' (RWB) behaviour. This is despite the fact that we considered the third epoch to have generated the most reliable RM results which were fully consistent with the spectral analysis and the simulation (which had no considerations for the jet). As such these results, along with the spectral power laws derived from the RM results (see Discussion), are a further indication that jet contamination would not have any significant effect on the analysis. Interestingly, the distribution of the β estimates across the four epochs closely tracks the form of the trend in our light-curve data. This further indicates that the trend does not originate from long-timescale jet variability but acts to drown-out the jet signal thereby explaining why epochs high in the trend demonstrated less RWB behaviour.

A more likely explanation for the bias in the PyROA lag estimates with default blurring is a result of PyROA over-fitting the light-curve data. Figure B.11 shows the magnitude of the residuals for the B band light-curve data with respect to the model PyROA fit in Figure 3.7. As can be seen, the residuals show no discernible pattern and appear as white noise meaning the apparent intra-day variability seen in our 3C 273 light-curves is likely to be majority noise. As a result, the erroneous PyROA fit we obtained with

the default blurring likely resulted in the algorithm fitting noise and returning lag estimates biased towards zero as a result of the model fits approaching a white noise form and becoming indistinguishable from each-other. Appendix Table B.2 shows the ratio of the amplitude of the model variability fit in Figure 3.7 to the average magnitude of the residuals for each of the six data-sets. As can be seen, the magnitude of these residuals is similar in scale to the amplitude of the variability fit by the algorithm which is a consequence of the relatively featureless form of the 3C 273 light-curve data in our study. As a result, the scale of the noise appears significant compared to our estimate of the magnitude of the real variability which means PyROA would face a strong penalty from the χ^2 term in its BIC function for not fitting the noise. This explains PyROA's tendency to overfit and justifies the strong blurring used in Figure 3.7 to discourage the fitting of noise. Table B.2 also shows that the relative magnitude of the noise is larger for the I and Z bands which could explain the greater lag bias we detected for these light-curves.

Javelin

The differential lag estimates and uncertainties derived from Javelin for each of the filters used to monitor 3C 273 is shown in Table 3.9 which also includes the predicted lag values converted into differential form. For the sake of consistency the following analysis is

Filter	Lag Estimate (days)		Lag Prediction (days)	
	PyROA	*Javelin*	$X = 4.96$	X_{new}
B	0	0	0	0
G	$4.00^{+1.77}_{-1.96}$	$3.16^{+0.40}_{-0.60}$	1.57	0.92
V	$7.15^{+1.79}_{-1.84}$	$6.89^{+1.53}_{-3.29}$	4.37	2.55
R	$15.02^{+1.71}_{-2.07}$	$15.96^{+3.30}_{-9.49}$	7.50	4.52
I	$17.94^{+2.94}_{-2.37}$	$15.30^{+15.40}_{-7.63}$	13.40	8.12
Z	$33.19^{+2.09}_{-2.36}$	$39.65^{+3.13}_{-6.36}$	18.83	11.50

Table 3.9: Differential lag estimates obtained by Javelin and PyROA with respect to the B band. Also included are both sets of differential lag predictions.

carried out on the third observing epoch of our light-curve data. The lag estimates were obtained using the 'Rmap' mode of Javelin using a restricted parameter lag space between $0 - 4\times$ the predicted lags so as to accommodate the potential emergence of the 'accretion disc size problem' as done for the PyROA analysis. Following the approach of Mudd et al (2018), we also restricted the decorrelation timescale parameter to $50 - 300$ days to make it consistent with the typical decorrelation timescales found in (SDSS, Macleod et

al 2010). These restrictions to the parameter space were necessary to help provide a more constrained fit which is an especially important consideration in our case due to the large parameter space introduced by six light-curves (17 parameters). Due to problems with convergence in our preliminary fits, we decided to run the following analysis with a large 100,000 iterations in the MCMC sampler which is double the amount used for the PyROA analysis. Figure 3.9 shows the fits and the distributions are in the Appendix Figure B.13.

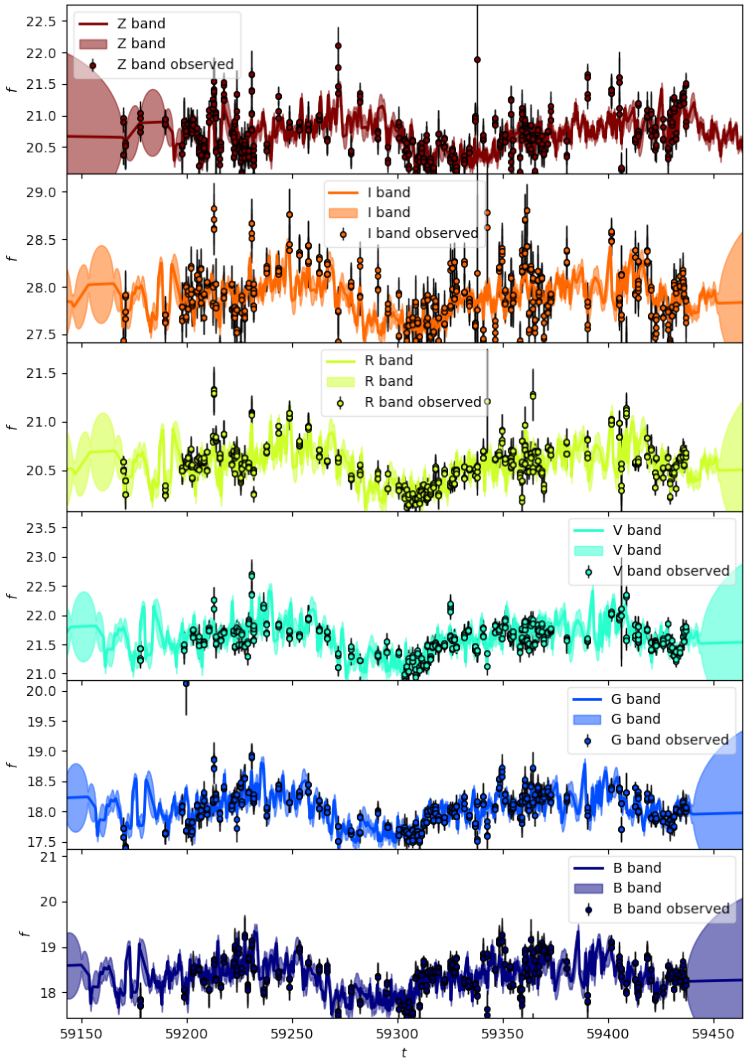

Figure 3.9: Javelin fit to the bgriz detrended, third epoch light-curves obtained for 3C 273. Flux values are in mJy.

PyceCREAM Results

RM analysis was attempted with the 3C 273 light-curve data using PyceCREAM however erroneously flat fits with unphysically small lag estimates were obtained. This is a likely consequence of the relatively featureless form of our 3C 273 light-curve data. The lack of variability seen in 3C 273 over our observing period is not too surprising considering its large luminosity meaning it can be expected to be larger than most quasars at its redshift and therefore have longer timescale variability. Our results should be contrasted with the successful PyceCREAM fits to 3C 120 done by Hlabathe, et al, (2020) which had very well structured light-curve data and similarly the case for 1H 2106-099 discussed in the next subsection.

3.3.3 Discussion

Figure 3.10 shows the differential lags and residuals obtained by PyROA with respect to the B band for the third epoch plotted against the rest frame centroid wavelengths of the LCO filters used to monitor 3C 273. Also shown is the expected power law $\tau \propto \lambda^{\beta}$ fitted to the data points with scipy 'curve-fit' with a classic thin disc model exponent $\beta = \frac{4}{3}$. The fit was obtained by weighting the data points according to how large the uncertainties were. As can be seen the measured lags are consistent with the classic thin disc model once error-bars are taken into consideration. However, once the fit was repeated allowing β to vary, the fitting software found a preferred power law fit to the PyROA data with a shallower exponent $\beta = 1.01 \pm 0.39$. This is remarkably consistent with the β value measured from the spectrum in Figure 3.6 and has greater consistency with the unapproximated thin disc model β value from the simulation (with the boundary condition) than the approximated value although the difference does not seem very significant. The magnitude of the lags estimated by PyROA for the third epoch in Table 3.7 are a factor $\sim 2-3$ larger than the standard $X = 4.96$ predictions and are $\sim 3-4\times$ larger the lags predicted by the X_{new} values. Therefore, if 3C 273 conforms to the thin disc model, the results of the third epoch suggest that it likely displays the widely observed 'accretion disc size problem'. To obtain lag estimates consistent with the PyROA estimates, a value $X \sim 7.4$ would be required.

The fits obtained in Figure 3.10 were extrapolated into the JHK bands so that differential lag predictions with respect to the B band could be made for the dust forming regions of the outer accretion disc. Lag predictions were obtained for both the approxi-

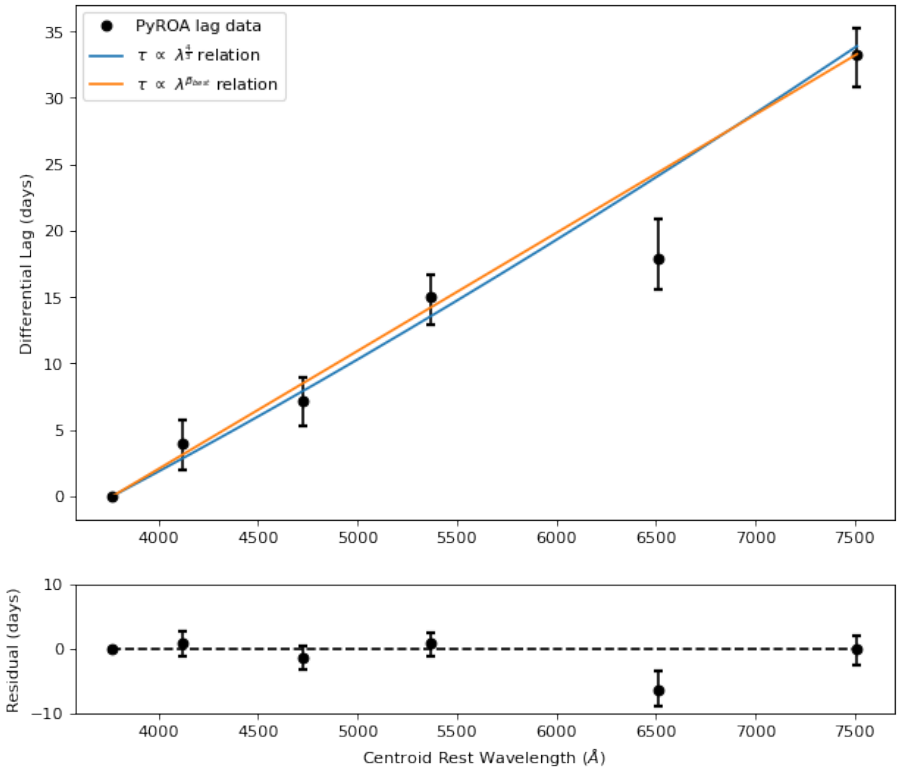

Figure 3.10: $\tau \propto \lambda^{\beta}$ power laws fit to the PyROA lag estimates both with the thin disc model $\beta = \frac{4}{3}$ value and a best-fit value $\beta = 1.01 \pm 0.39$. The residuals are given with respect to the best-fit power law.

mated thin-disc power law with $\beta = \frac{4}{3}$ and the best-fit power law $\beta = 1.01 \pm 0.39$. The predictions are shown in Table 3.10 which have been converted to absolute lag predictions derived by estimating the absolute B band lag using $X = 7.4$ to scale the accretion disc to make it consistent with the PyROA RM results. These predictions will allow comparisons with the results of upcoming near infrared RM campaigns on 3C 273 and should help provide a preference between the approximated thin disc value $\beta = \frac{4}{3}$ and our estimated unapproximated thin disc value $\beta \sim 1$.

Figure 3.12 shows the differential lags and residuals obtained by Javelin and PyROA with respect to the B band plotted against the rest frame centroid wavelengths of the filters used to monitor 3C 273. As done with the PyROA analysis, a classic thin disc power law with exponent $\beta = \frac{4}{3}$ and a best-fit power law with an unfixed β were fit to the data points using scipy 'curve-fit' weighted by the uncertainties. As can be seen, the measured lags fit well to the classic thin disc model once error-bars are considered. Interestingly, the plotting software preferred a power law fit with a steeper exponent $\beta = 1.59 \pm 0.29$ for the Javelin data which is still consistent with the classic thin disc model within its uncertainty

Filter	Lag Prediction (days)			
	PyROA		*Javelin and PyROA*	
	$\beta = \frac{4}{3}$	$\beta \sim 1.01$	$\beta = \frac{4}{3}$	$\beta \sim 1.16$
J	110.2	99.4	115.2	108.9
H	161.2	136.1	167.7	153.0
K	235.1	184.6	243.7	214.0

Table 3.10: Absolute lag predictions for the JHK emitting regions of the accretion disc in 3C 273 interpolated from Figures 3.11 and B.14 for the PyROA and the combined PyROA and Javelin RM results. The lag predictions were converted to absolute form by estimating the absolute lag of the B band as ~ 21.6 days using $X = 7.4$ and ~ 24.0 using $X = 8.0$ to scale the accretion disc to make it consistent with the PyROA and the combined PyROA and Javelin RM results respectively.

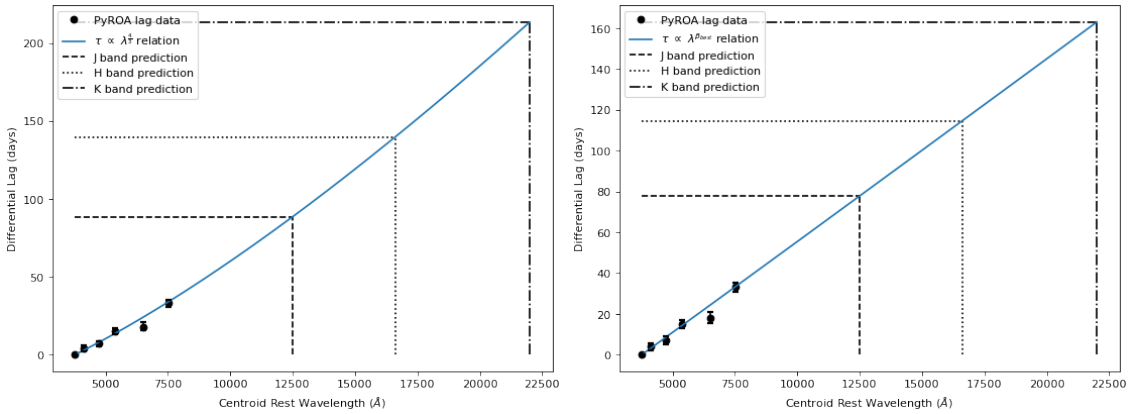

(a) Extrapolation of the thin disc $\beta = \frac{4}{3}$ power law.

(b) Extrapolation of the best-fit $\beta \sim 1.01$ power law.

Figure 3.11: Extrapolations of the classic thin disc and best-fit power laws fit to the PyROA RM results into the near-infrared JHK regime. This allowed lag predictions in Table 3.10 to be made.

range. However, this value is inconsistent with the shallower β values preferred by the PyROA RM results, the spectral fit, the photometric method and the simulation.

With both the PyROA and Javelin results, the plotting software fit a power law (weighted by the uncertainties) to Figure 3.12 with a shallower exponent $\beta = 1.16 \pm 0.25$ which is consistent with both the shallower β values obtained by the previous analysis and with the approximated thin disc model within its uncertainty range. In particular, this value is very close to the unapproximated thin disc model estimate from the simulation with the inclusion of the boundary condition term. The magnitude of the lag estimates returned by Javelin in Table 3.9 are a factor $\sim 1.5-2$ larger than the lags predicted by the standard $X = 4.96$ method and a factor $\sim 3-4$ larger than those predicted using the X_{new} values. Therefore, if 3C 273 conforms to the thin disc model, the Javelin results agree with

the PyROA results in indicating that it likely displays the 'accretion disc size problem'. To obtain lag predictions which reflect the Javelin results, a value $X \sim 8.6$ would be required. As was done with the PyROA analysis, the thin disc and best-fit power law fits in Figure 3.12 were extrapolated into the JHK regime so as to obtain lag predictions for the dust forming parts of the accretion disc as shown in Figure B.14. The lag predictions for the combined Javelin and PyROA results for both $\beta = \frac{4}{3}$ and $\beta = 1.16 \pm 0.25$ are shown in Table 3.10. To convert these to absolute lag values, the absolute B band lag was estimated using $X = 8$ to scale the accretion disc to make it consistent with the combined PyROA and Javelin results. This X value was averaged over the $X \sim 7.4$ and $X \sim 8.6$ values returned for the PyROA and Javelin RM results respectively.

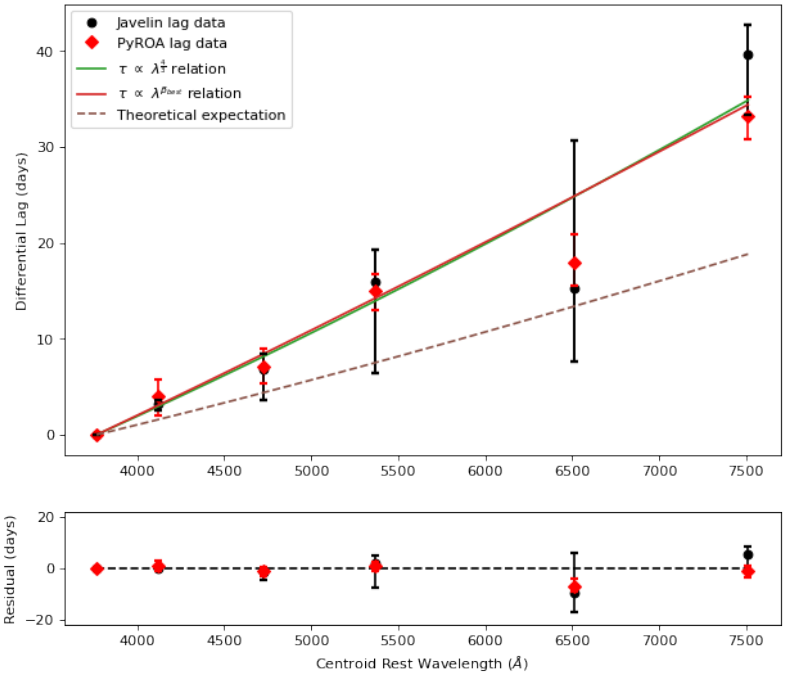

Figure 3.12: $\tau \propto \lambda^{\beta}$ power laws fit to the combined Javelin and PyROA lag estimates both with the thin disc model $\beta = \frac{4}{3}$ value and a best-fit value $\beta = 1.16 \pm 0.25$. The residuals are given with respect to the best-fit power law. Also shown is the theoretical power law expected from the lag predictions using $X = 4.96$.

It should also be mentioned that none of the bias apparent in the PyROA lag estimates with default blurring were present in the Javelin fits. This is probably due to the preliminary fits done to the driving light-curve in Javelin which calibrates the decorrelation timescale to be the same order as the median sampling interval of the data. This would act to discourage Javelin from over-fitting the noise as likely happened in PyROA. Our restriction of the decorrelation timescale to $50 - 300$ days also likely helped on this front.

It is also clear from Table 3.9 that Javelin returned lag estimates with much larger uncertainties than the PyROA estimates which are as a result of the poorer convergence in the Javelin lag distributions despite the much larger number of iterations used. This matches observations made in Chapter 2.

The fits obtained in Figures 3.10 and 3.12 were done with the exclusion of the I band data point. This was because this data point appeared anomalously small which is most obvious from the residuals. The anomaly is unlikely to come from contamination as the main source in 3C 273 which can bias lags to smaller values is the jet which is unlikely to have any significant effect on lag estimates (see below). The model fits for the I band in Figures 3.7 and 3.9 appears to slightly lag behind the data which indicates the anomaly could be a fitting issue. Table B.2 reveals that the I band light-curve has the largest average noise magnitude relative to the amplitude of the fitted signal meaning a likely source of the anomaly is the significant noise in this data-set obscuring the light-curve signal. However the estimated significance of the noise in the I band is similar to that in the Z band meaning we are probably not fully accounting for the cause of the apparent anomaly.

Bolometric luminosity estimates were derived for each of the bgriz filters in the complete light-curve data in Figure 3.1(a). This was done by scaling the unapproximated 3C 273 simulated accretion disc spectrum in Figure 3.3 to the average flux in each light-curve in Figure 3.1(a). The bolometric luminosities were estimated by integrating the area under the resultant curves and are shown in Table 3.11. As can be seen, the approximate estimates all fall within a factor$\sim$ 1.5 the value measured in Landt et al (2011) (given in Table 3.1) except for the value estimated by normalising to the I band flux which is a factor ~ 2 larger. Interestingly, the filters providing the largest bolometric luminosity estimates coincide with the most heavily contaminated filters in Table 3.3 (with the exception of the I band for which no contamination estimates could be obtained). This heavily implies that the I band flux has significant contamination which most likely originates from the jet. These findings show a possible method of obtaining crude contamination estimates in the absence of spectral data.

The results of the spectral fit in Figure 3.6, the photometric investigation shown in Figure 3.8 and the PyROA and combined PyROA and Javelin RM results all indicate that the expected spectral power law $\lambda f_\lambda \propto \lambda^{-\beta}$ followed by the accretion disc of 3C 273 has a slightly shallower exponent $\beta \sim 1$ than expected by the approximated thin disc model

Filter	L_{bol} (ergs^{-1})
B	5.9×10^{46}
G	5.8×10^{46}
V	7.0×10^{46}
R	6.8×10^{46}
I	9.4×10^{46}
Z	7.2×10^{46}

Table 3.11: Bolometric luminosity estimated made for 3C 273 using each of the LCO filters used in the campaign. An estimate $L_{bol} = 4.57 \times 10^{46}ergs^{-1}$ was obtained in Landt et al (2011).

where $\beta = \frac{4}{3}$ although the difference may not be very significant. This finding is consistent with our more physically correct unapproximated thin disc model simulation (with the inclusion of the boundary condition) which is in agreement with the RM results and the spectral fit within the updated uncertainty range and has a particularly close agreement with the combined PyROA and Javelin RM results. Interestingly Fausnaugh et al (2016) found a similar best-fit $\beta \sim 1$ value for the accretion disc power law during their investigations of NGC 5548. The Javelin RM results alone preferred a steeper β value inconsistent with the the rest of the analysis but still consistent with the approximated thin disc model. Due to the close agreement found by the rest of the analysis and the poorer convergence seen in the Javelin posterior distributions, we think the shallower $\beta \sim 1$ fit is more reliable. This value is inconsistent with the findings of Figaredo et al (2020) which, by fitting power laws to the optical bvrz bands of 3C 273, estimated an exponent value $\beta = 1.34 \pm 0.06$ in agreement with the classic thin disc model. The results of our RM analysis are just about consistent with the findings of Figaredo et al (2020) within the upper limits of their uncertainty range. However, if our simulation is correct, our analysis has a stronger agreement with the unapproximated thin disc model which takes account of the boundary condition at r_{ISCO} although it is not clear how significant the difference is with the approximated model. As such we think it is likely that 3C 273 conforms to the thin disc model but that this agreement could become obscured when disregarding the boundary condition.

If 3C 273 conforms to the thin disc model, the magnitude of the lag estimates obtained by PyROA and Javelin indicates that it displays the 'accretion disc size problem'. This is a widely observed phenomena in both accretion disc RM studies (e.g. Cackett et al, 2018; Fausnaugh et al, 2016) and surveys (e.g. Mudd et al 2018) whereby the scale of

the accretion disc is a factor $\sim 2-3$ larger than predicted. This is consistent with our PyROA and Javelin lag estimates which are a magnitude $\sim 2-3$ larger than the standard lag prediction with $X = 4.96$ and are a factor $\sim 3-4$ larger than the predictions made with X_{new}. The 'accretion disc size problem' indicates either that our understanding of how the radius scales with wavelength in the accretion disc is wrong or that some of the assumptions made in obtaining the lag estimates are incorrect (e.g. mass accretion rate or efficiency). The results of our RM lag estimates suggests that the 'accretion disc size problem' manifests itself as a linear scaling of the entire accretion disc. A comparison of the lag predictions obtained using the standard approach $X = 4.96$ to the new approach using estimating X_{new} values outlined in Mudd et al (2018) reveals that the standard approach yielded lag predictions more similar to the estimates obtained by PyROA and Javelin. However the likely presence of the 'accretion disc size problem' means that neither set of lag predictions were consistent with the estimates. As such, 3C 273 appears to be a special case and we do not form any conclusions on which method of lag prediction is superior until they are tested on standard AGN not displaying the 'accretion disc size problem'.

Analysis carried out on 3C 273 by Sturm et al (2018) as part of the GRAVITY collaboration obtained an estimated absolute lag to the Paα emitting part of the BLR of 145 ± 35 days which they took as an estimate for the mean radius of the BLR. Using the 'Failed Radiatively Accelerated Dust-driven Outflow' (FRADO) model of the formation of the BLR explained by Czerny et al (2015), we obtained an absolute mean lag estimate for the BLR of 173.3 ± 11.3 days using our PyROA RM results by interpolating our best fit power law Figure 3.11(b). Similar absolute lag estimates for the BLR of 191.4 ± 22.6 days are obtained using the best-fit combined PyROA and Javelin RM results in Figure B.14(b). This should be contrasted with the mean BLR lag estimates obtained using the PyROA and combined PyROA and Javelin RM results with approximated thin disc model fits ($\beta = \frac{4}{3}$) in Figures 3.11(a) and B.14(a) which gave absolute lag estimates 217.4 ± 17.7 and 215.4 ± 28.4 days respectively. Therefore we obtain mean BLR lag estimates consistent with the values measured by Sturm et al (2018) when using our shallower $\beta \sim 1$ power laws and get inconsistent estimates when using the standard $\beta = \frac{4}{3}$ power laws. This provides another independent indication that the spectral power law of the accretion disc in 3C 273 is shallower than predicted by the approximated thin disc model in agreement with the spectral fit, the PyROA and combined PyROA RM results and the photometric

investigation. For a more detailed explanation of how we derived these lag estimates please see Appendix B.2.6.

A point of discussion in the literature on 3C 273 is the significance of the emission from the jet in the optical spectrum. Black-body modelling and synchrotron emission models fit to the SED of 3C 273 by Yuan et al (2022) suggest that the optical continuum emission is dominated by the accretion disc thermal emission indicating an insignificant jet contribution. However the spectral observations made in Yuan et al (2022) only extended up to rest wavelengths $\sim 5500\mathring{A}$ meaning they did not monitor the near infrared optical region which would be expected to be the most heavily contaminated by the jet according to Paltani et al (1998). In addition to the findings of Paltani et al (1998) discussed previously, broad line RM data analysed by Zhang et al (2018) revealed the presence of very long timescale trends in the continuum light-curves of 3C 273 which were not present in the the emission line light-curves. This observation is consistent with a significantly contaminating jet at optical wavelengths introducing long timescale variability. Attempts to quantify the extent of the long timescale jet contamination in the optical were done by Li et al (2020) by modelling the disc and jet variability as DRW's with Gaussian transfer functions and fitting these models to measured optical continuum, radio and Hβ emission line light-curves using a Bayesian approach which closely follows the approach of Javelin. The fitted V band light-curve along with the expected decomposed accretion disc and jet variability they derived is reproduced in Figure 3.13 which shows the long-timescale accretion disk variability has a larger magnitude than the long timescale jet variability. Based on this analysis they concluded that the jet contributes a minimum of $\sim$ 10% of

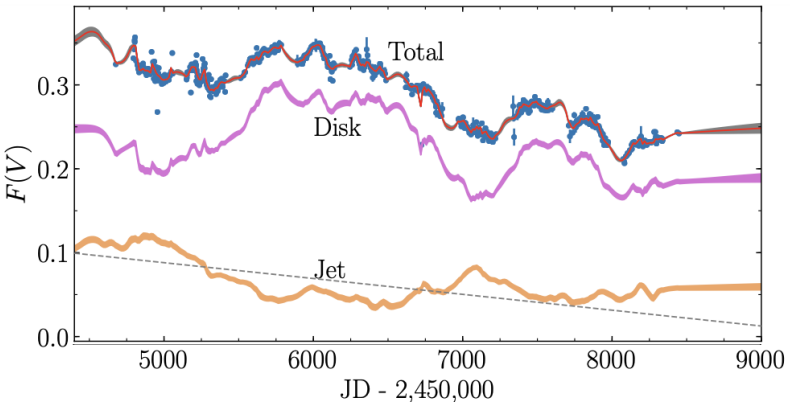

Figure 3.13: V band light-curve fit decomposed into the accretion disc and jet variability components for 3C 273 taken from Li et al (2020).

the optical emission when in its low state (with the accretion disc in its high state) and a

maximum of $\sim 40\%$ of the optical emission when in its high state (and the accretion disc in its low state). This is consistent with our contamination estimate for the Z band of $\sim 28\%$ which is not caused by strong emission lines and so we attribute to the jet. This estimate was based on thin disc model fits to the spectrum in Figure B.9 and is detailed in Appendix B.2.1. However we detected no significant jet contamination for the bvr optical bands which is consistent with the findings of Paltani et al (1998) and Yuan et al (2022) by indicating the jet has no significant component at the shorter wavelength optical.

Our conclusion from the previous section that the trend observed in our 3C 273 light-curves most likely originates from the accretion disc, as a result of the inconsistency with the predicted timescale of the R component by Paltani et al (1998) and the presence of this trend in the U band, does not contradict the findings of Li et al (2020). The apparent timescale of the long term variable jet component in Figure 3.13 seems to be upwards of $\sim$ 3000 days (similar to the timescale for the trend seen in Zhang et al 2018) which is in-line with the predicted variability timescale of the R component in Paltani et al (1998) of over $\sim$ 10 years. Over the much shorter observing period of our study, no significant long-timescale jet variability would be detected. As such, the trends in our light-curves in Figure 3.1(a) could easily be attributed to the shorter timescale structure seen in the accretion disc component in Figure 3.13. Importantly, even with the significant contamination estimates made by Li et al (2020), we found no significant effect on our RM lag estimates. As such, our results are broadly consistent with the findings of Yan-Roi Li et al (2020), Paltani et al (1998) and Yuan et al (2022).

3.4 1H 2106-099

3.4.1 Theoretical lag estimates

We generated a simulation of the accretion disc spectrum expected from the thin disc model for 1H 2106-099 following the approach done for 3C 273. This was done assuming a SMBH mass $M = 2.3 \times 10^7 M_\odot$ and bolometric luminosity $L_{bol} = 10^{45.1} \mathrm{ergs}^{-1}$ (both taken from Landt et al 2011) and assuming a standard efficiency $\eta = 0.1$. Figure 3.14(a) shows the expected spectral locations of the centroid wavelengths of the LCO filters used to monitor 1H 2106-099 in our campaign using our thin accretion disc simulation. By replotting this in a logarithmic form over the spectral range investigated in this campaign, estimates for the accretion disc power law exponent β can be obtained using the thin

accretion disc relation $\lambda f_\lambda \propto -\beta \log\lambda$ as done for 3C 273. The expected values from the simulation both with and without the boundary condition are presented in Table 3.12. As can be seen, both simulations generated expected values of β close to the classic thin disc value $\beta = \frac{4}{3}$. The simulated black-body curve for 1H 2106-099 is narrower and more sharply peaked at shorter wavelengths than 3C 273. This is to be expected as 1H 2106-099 has a less massive SMBH than 3C 273 meaning its accretion disc has a smaller r_{ISCO} and so would emit at shorter wavelengths. In fact, the simulation predicts the innermost region of the accretion disc in 1H 2106-099 would emit in the X-rays which is consistent with observations of 1H 2106-099 as a strong X-ray emitter.

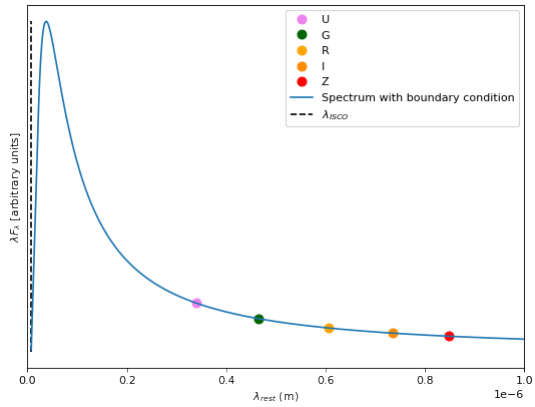

(a) Simulated spectrum with the expected location of the LCO filter rest wavelengths for 1H 2106-099.

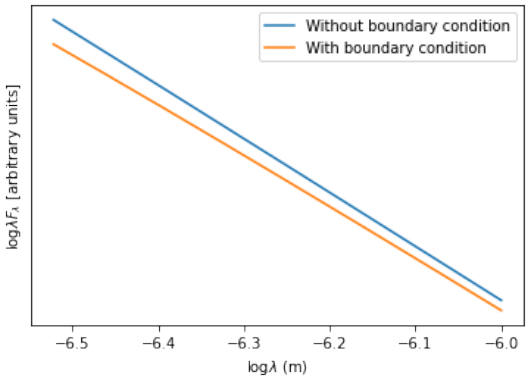

(b) Simulated spectrum for 1H 2106-099 in logarithmic space.

Figure 3.14: Simulated accretion disc spectrum for 1H 2106-099 in linear and logarithmic space.

Figure 3.15 shows a similarly plotted real logarithmic spectrum for 1H 2106-099 taken from Landt et al (2011) where the near-infrared spectrum has been normalised around the 1μm wavelength as done in Landt et al (2011). A linear fit is done to the part of the spectrum spanning the riz LCO filters which generated a measured β value stated in Table 3.12. Here the fit and the associated uncertainty is generated by 'lmfit'. This value for the power law exponent strongly agrees with the standard thin-disc value and is in fact closer to the approximated simulation than the unapproximated simulation although the scale of the difference between the two is much less than in 3C 273. However, it is clear from Figure 3.15 that the part of the spectrum spanned by the g and u LCO filters diverges significantly from the thin disc model relationship. This strange spectral behaviour could signify significant host galaxy contamination of the ug filters which would have the expected effect of flattening the spectrum however we believe this is inconsistent

with the obtained RM results (see later).

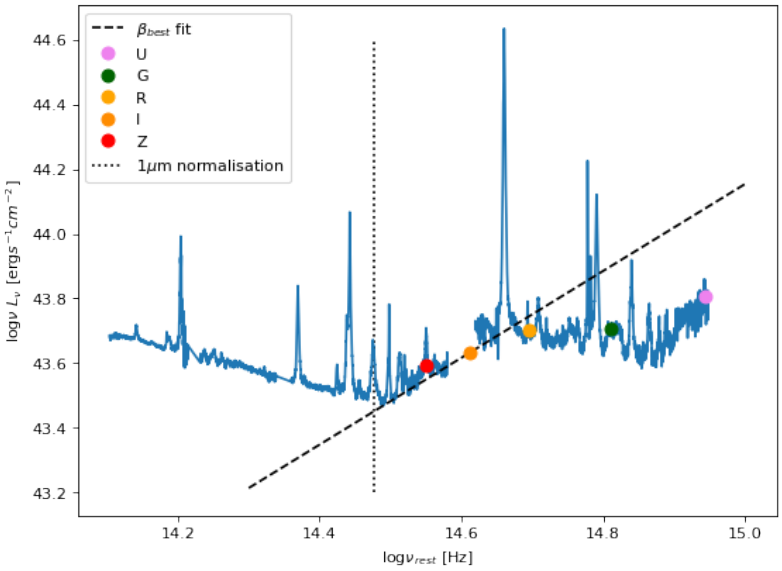

Figure 3.15: Spectrum of 1H 2106-099 taken from Landt et al (2011) plotted in a logarithmic form. A linear function is fit to the riz filters which returns a measured power law exponent $\beta = 1.38 \pm 0.22$

	Spectral value	Simulated value	
		With boundary condition	*Without boundary condition*
$\lvert\beta\rvert$	1.38 ± 0.22	1.26	1.32

Table 3.12: A summary of the estimated magnitude of β values obtained from the spectral fit in Figure 3.13 and the simulations in Figure 3.12.

For the following RM analysis, predicted absolute lag estimates were derived for each of the LCO filters used to monitor 1H 2106-099 using the unapproximated thin accretion disc model. This was done following the approach used for 3C 273 both with the standard $X = 4.96$ value and with new X_{new} values estimated following the approach of Mudd et al (2018). As with the simulation, an estimated SMBH mass $M = 2.3 \times 10^7 M_\odot$ and bolometric luminosity $L_{bol} = 10^{45.1}$ (taken from Landt et al 2011) were used as well as the standard efficiency $\eta = 0.1$. The lag predictions for both treatments of X are shown in Table 3.13 and the estimated X_{new} values for each filter are shown in Table B.4. The X values obtained for 1H 2106-099 are smaller than those obtained for 3C 273. This is to be expected for the less steeply declining 3C 273 spectrum simulated in Figure 3.3 which indicates annuli emitting more strongly over a range of wavelengths. As such, a larger proportionality constant would be needed to convert from the picture of annuli emitting

Filter	Lag Prediction (days)	
	$X = 4.96$	X_{new}
U	0.96	0.67
G	1.46	0.98
R	2.09	1.37
I	2.71	1.75
Z	3.28	2.10

Table 3.13: Absolute lag predictions for the regions of the accretion disc in 1H 2106-099 emitting predominantly in each of the LCO filters. Two sets of predictions are obtained using the standard $X = 4.96$ and a new set of X values derived following the approach of Mudd et al (2018).

at fixed wavelengths to the black-body annuli picture.

3.4.2 Algorithm Results

PyROA Results

The differential lag estimates and uncertainties derived from PyROA for each of the filters used to monitor 1H 2106-099 is shown in Table 3.14 which also includes the predicted lag values converted into differential form. Table 3.14 shows two sets of lag estimates both with and without the discontinuity apparent in Figure 3.19 (see Discussion). Each of the lag estimates is made with respect to the U filter which is assumed as the driving light-curve. The lag estimates were obtained using the default Dirac delta transfer function with the default Gaussian window width uniform prior set at $0.01 \leq \Delta \leq 10$ days to set a standard degree of blurring. The uniform lag prior was set between $0 \leq \tau \leq 10$ days to accommodate the potential appearance of the 'accretion disc size problem'. The PyROA analysis was done with 50,000 iterations in the MCMC sampler to ensure good convergence. The fits and corner plots obtained are shown in Figures 3.16 and B.19 respectively. A good fit is obtained with the sharp lag distributions indicating a good convergence with very little scatter magnitude with respect to the model fit as shown in Table B.5.

Javelin Results

The differential lag estimates and uncertainties derived from Javelin for each of the LCO griz filters used to monitor 1H 2106-099 is shown in Table 3.15 which also includes the predicted lag values converted into differential form. Table 3.15 also includes two sets of

Filter	Lag Estimates (days)		Lag Prediction (days)	
	Unshifted	*Shifted*	$X = 4.96$	X_{new}
U	0	0	0	0
G	$0.07^{+0.10}_{-0.05}$	$0.36^{+0.10}_{-0.05}$	0.50	0.31
R	$1.42^{+0.11}_{-0.08}$	$0.78^{+0.11}_{-0.08}$	1.13	0.70
I	$1.90^{+0.11}_{-0.09}$	$1.18^{+0.11}_{-0.09}$	1.75	1.08
Z	$2.25^{+0.13}_{-0.12}$	$1.55^{+0.13}_{-0.12}$	2.32	1.43

Table 3.14: Differential lag estimates for the regions of the accretion disc in 1H 2106-099 emitting predominantly in each of the LCO filters. Estimates were obtained for the unshifted and shifted power laws represented in Figures 3.19 and 3.20 respectively. Two sets of predictions are obtained using the standard $X = 4.96$ and a new set of X values derived following the approach of Mudd et al (2018).

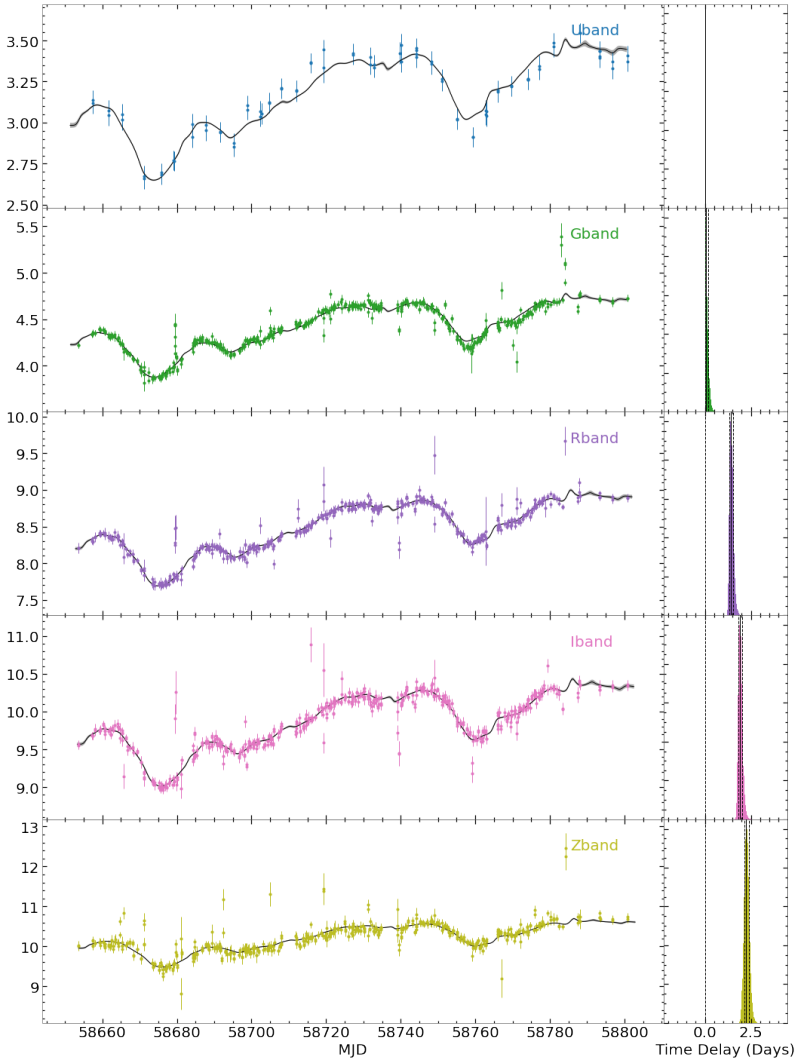

Figure 3.16: PyROA fit to the light-curves obtained for 1H 2106-099. Flux values are in mJy.

lag estimates both with and without the discontinuity seen in Figure 3.22 (see Discussion). Each of the lag estimates is made with respect to the G filter which is assumed as the driving light-curve. The lag estimates were obtained using a parameter lag space restricted between $0 - 10$ days so as to accommodate the potential emergence of the 'accretion disc size problem'. The following analysis was run with a large 100,000 iterations in the MCMC sampler which is double the amount used for the PyROA analysis. Figure 3.17 and B.22 shows the fits and distributions obtained from the analysis.

Filter	Lag Estimate (days)				Lag Prediction (days)	
	Unshifted		*Shifted*		*X=4.96*	X_{new}
	PyROA	*Javelin*	*PyROA*	*Javelin*		
G	0	0	0	0	0	0
R	$1.35^{+0.15}_{-0.09}$	$1.78^{+0.03}_{-0.07}$	$0.42^{+0.15}_{-0.09}$	$0.42^{+0.03}_{-0.07}$	0.63	0.39
I	$1.83^{+0.15}_{-0.10}$	$2.56^{+0.05}_{-0.73}$	$0.82^{+0.15}_{-0.10}$	$1.20^{+0.05}_{-0.73}$	1.25	0.77
Z	$2.18^{+0.16}_{-0.13}$	$2.57^{+0.29}_{-0.05}$	$1.19^{+0.16}_{-0.13}$	$1.21^{+0.29}_{-0.05}$	1.82	1.12

Table 3.15: Differential lag estimates for the regions of the accretion disc in 1H 2106-099 emitting predominantly in the griz LCO filters. Estimates were obtained for the unshifted and shifted power laws corresponding to Figures 3.23 and 3.22. Two sets of predictions are obtained using the standard $X = 4.96$ and a new set of X values derived following the approach of Mudd et al (2018).

It should be mentioned that the U band was excluded from this analysis due to erroneous U band fits we obtained which generated results completely inconsistent with the rest of the analysis when running the full ugriz data-set. These erroneous fits and distributions along with the lag estimates and analysis is shown in Appendix B.3.1. We attribute this to a poor convergence due to the presence of bimodal distributions which likely effected the U band light-curve the most due to its poor cadence making it the least constrained data-set. This poor data-set appears to have had the largest effect on Javelin which can be explained from our analysis in Chapter 2 where we found Javelin to have had the greatest difficulty in converging out of the three algorithms (for the same limits placed on the lag space) meaning it could be expected to be the most susceptible to under-constrained data-sets. By excluding the U band we obtained no apparent erroneous fits and improved distributions. Whilst many are still bimodal, the secondary peaks are less significant and closer in parameter space to the primary peaks.

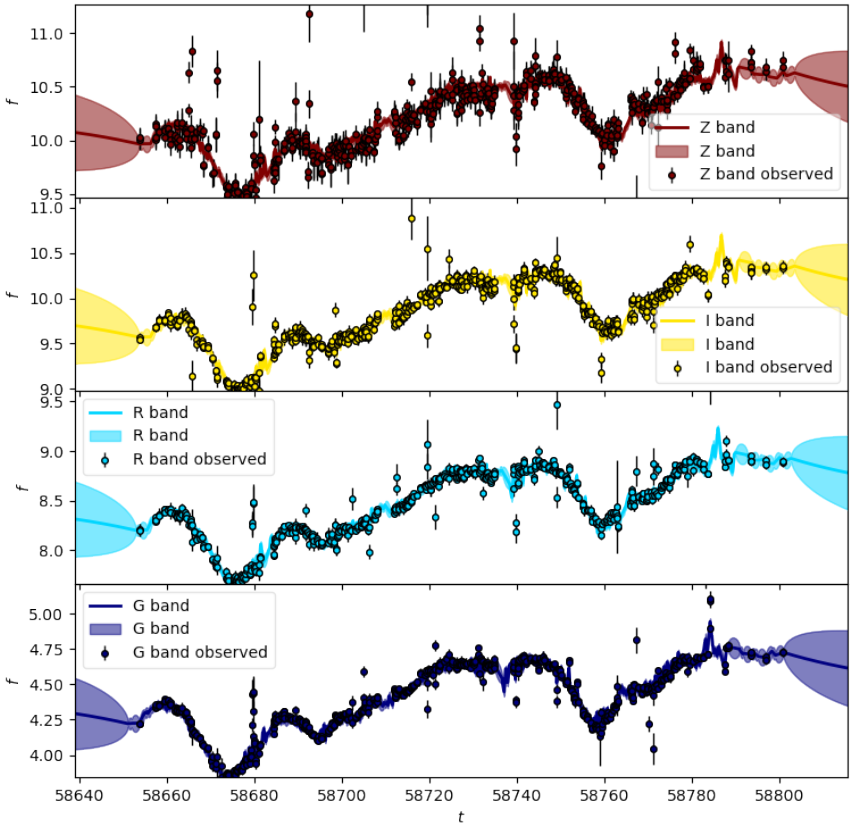

Figure 3.17: Javelin fit to the light-curves obtained for 1H 2106-099 with the exclusion of the U band. Flux values are in mJy.

PyceCREAM Results

The absolute lag estimates and uncertainties derived from PyceCREAM for each of the LCO ugriz filters used to monitor 1H 2106-099 is shown in Table 3.16 which also includes the predicted lag values. The lag esitmates were obtained using the accretion disc transfer function mode of PyceCREAM with the lag parameter space restricted between 0-50 days. The default PyceCREAM assumption of a face-on accretion disc with a mass accretion rate $\dot{m} = 0.1 M_{\odot}$ per year and standard efficiency $\eta = 0.1$ as well as a spectral power law with thin disc exponent $\beta = \frac{4}{3}$ were used. When running the algorithm, the Fourier series was truncated at the default Fourier frequency $\omega_{high} = 0.5$ and the SMBH mass $M = 2.3 \times 10^7 M_{\odot}$ was used and $z = 0.027$. The following analysis was run with 5000 iterations in the MCMC sampler which obtained good convergence as indicated by the well peaked distributions in Figure B.24. Figure 3.18 shows the corresponding fits.

Filter	Lag Estimate (days)	Lag Prediction (days)	
		X=4.96	X_{new}
U	$1.54^{+0.07}_{-0.09}$	0.96	0.67
G	$2.32^{+0.10}_{-0.14}$	1.46	0.98
R	$3.30^{+0.14}_{-0.21}$	2.09	1.37
I	$4.27^{+0.18}_{-0.27}$	2.71	1.75
Z	$5.17^{+0.21}_{-0.33}$	3.28	2.10

Table 3.16: Absolute lag estimates for the regions of the accretion disc in 1H 2106-099 emitting predominantly in the ugriz LCO filters obtained by PyceCREAM. Two sets of predictions are obtained using the standard $X = 4.96$ and a new set of X values derived following the approach of Mudd et al (2018).

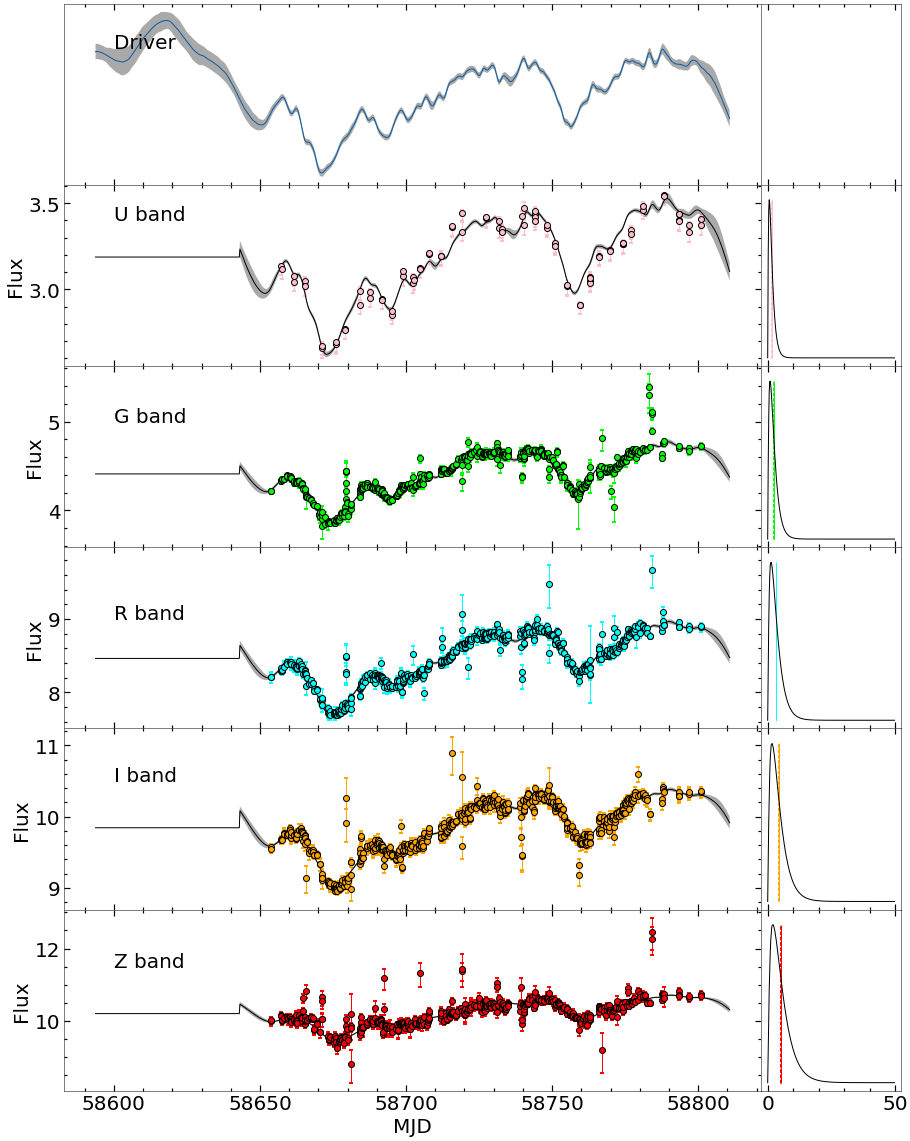

Figure 3.18: PyceCREAM fit to the light-curves obtained for 1H 2106-099. Flux values are in mJy.

3.4.3 Discussion

Figure 3.19 shows the differential lag estimates obtained by PyROA with respect to the U band plotted against the rest frame centroid wavelengths of the filters used to monitor 1H 2106-099. As is immediately clear, it appears as if the complete lag estimates conform to two power laws with the riz and ug data points respectively fitting well to different power laws against the expectations of a continuous $\tau \propto \lambda^{\beta}$ relation. To fit the lag estimates associated with the riz filters, the data points were replotted in a logarithmic space and fit by a linear function as shown in Figure B.18 which output an estimated value for the power law exponent $\beta = 1.37 \pm 0.36$ and generated the power law fit in Figure 3.19. This approach was used due to the large uncertainties obtained when fitting the power law directly due to the lack of data points to constrain the fit. As a result, the power law fit for the riz filters conforms closely to the thin-disc model as expected by the spectral fit in Figure 3.15. As can be seen, the ug data points also fit well to the thin disc power law albeit one with a different amplitude to that fit to the riz data points.

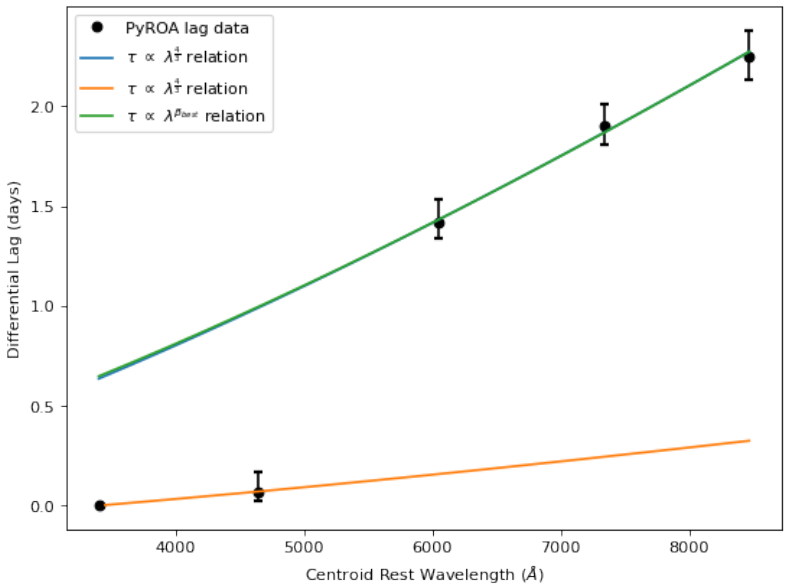

Figure 3.19: $\tau \propto \lambda^{\beta}$ power laws fit to the PyROA lag estimates. As can be seen two separate thin disc power laws can be fit to the riz and ug data points with $\beta = 1.37 \pm 0.36$ and $\beta = \frac{4}{3}$ respectively.

The PyROA RM results reflect the strange spectrum obtained in Figure 3.15 by indicating that the riz filters conform closely to the thin disc model and that the ug filters differ from this relation. One possible explanation for the discontinuity in the RM results could be the presence of significant contamination in the ug filters to flatten the spectrum

for these filters and bias their corresponding lags. However, we expect significant broad-line contamination of the ug bands to decrease their differential lags with respect to the riz filters (as the BLR exists further from the SMBH than the accretion disc) which is the opposite to the direction of the bias seen in Figure 3.19. Similarly, whilst broad-line contamination of the riz filters would account for the correct direction of the bias, we did not detect any more significant contamination in the Z filter than in the G. Broad emission line contamination of the riz filters would also not explain the flattened spectrum obtained for the ug filters in Figure 3.15. In addition, the differential lags for the riz filters fit well to a continuous thin disc power law which would not be expected if the BLR contamination introduced a significant bias of the lags due to the large differences in the BLR contamination level across the riz filters indicated by Table 3.4.

Nevertheless, the discontinuity seen in Figures 3.15 and 3.19 could be a result of an unidentified contamination of the ug filters. In this case, the discontinuity would not be physically present in the accretion disc which, as a result of the spectral fit in Figure 3.15, would reasonably be expected to closely follow the thin disc model. Therefore, if the discontinuity is erroneous, the data points in Figure 3.19 would be expected to fit a continuous thin disc power law. This scenario is represented in Figure 3.20 where the differential lags for the riz filters with respect to the U band have been shifted down by a constant value of 0.64 days to obtain the best-fit continuous power law from Figure 3.19 through the U band data point. This enables new differential lag estimates to be obtained under the assumption that the discontinuity is erroneous which are shown in Table 3.14. In this scenario, the anomalous G band lag is attributed to the biasing effect with the new lag estimate coming from the assumption that the unbiased estimate lies on the thin disc power law as shown as the circled point in Figure 3.20. As can be seen, these new lag estimates are remarkably consistent with the predictions made using the X_{new} values but are inconsistently small compared to the predictions with the standard $X = 4.96$ value. As such these results indicate that, if the discontinuity in the lag estimates is erroneous, 1H 2106-099 likely does not display the 'accretion disc size problem' and that the lag predictions made following the new treatment of X outlined in Mudd et al (2018) is more accurate than the traditional approach for AGN without the 'accretion disc size problem'.

Figure 3.21 show the riz filters best-fit power laws for the shifted and unshifted cases extrapolated into the JHK regime. This enabled us to obtain differential lag predictions for the JHK bands in the scenarios where the discontinuity in the RM results is erroneous

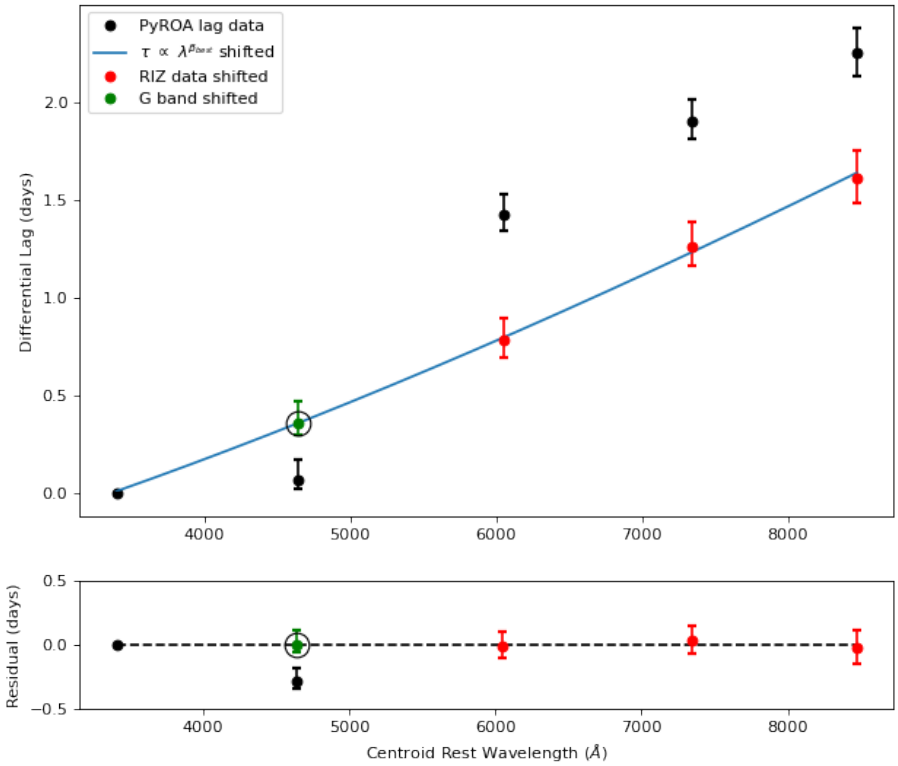

Figure 3.20: The scenario where the discontinuity in the lag estimates is assumed to be erroneous. Here the riz data points have been shifted down by the U band residual and the best fit power law $\tau \propto \lambda^{\beta}$ with $\beta = 1.37 \pm 0.36$ is shown. The anomalous G lag is assumed to be as a result of the biasing effect and so is shifted onto the thin disc power law.

(Figure 3.21(a)) and physically real (Figure 3.21(b)) as shown in Table 3.17. The two sets of predictions are very similar meaning it is unlikely we will be able to differentiate between the two scenarios in the near-infrared RM campaigns.

Filter	Lag Prediction (days)	
	Shifted	*Unshifted*
J	3.24	3.88
H	5.08	5.72
K	7.77	8.41

Table 3.17: Differential lag predictions for the JHK emitting regions of the accretion disc in 1H 2106-099 interpolated from Figure 3.21 using the PyROA RM results. Predictions for the original results in Figure 3.21(a) and the shifted results in Figure 3.21(b) are shown. The lag predictions are made with respect to the U band.

Figure 3.22 shows the differential lag estimates obtained by Javelin with respect to the G band plotted against the centroid griz wavelengths. Again, the same discontinuity between the g and riz filters is obtained. Also shown are thin disc and best-fit power

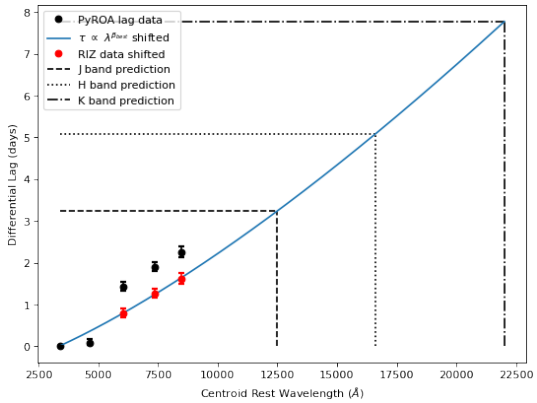

(a) Extrapolation of the shifted power law corresponding to Figure 4.30.

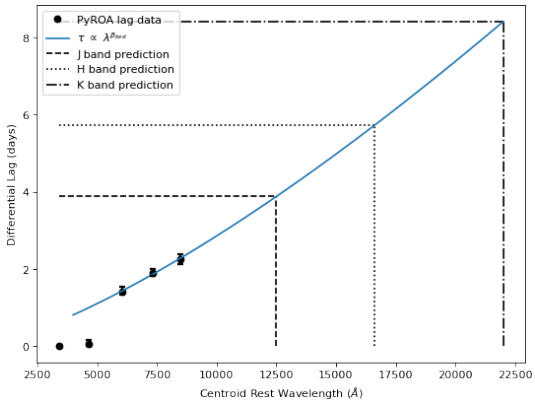

(b) Extrapolation of the unshifted power law corresponding to Figure 4.29.

Figure 3.21: Extrapolations of the shifted and unshifted best-fit power law fit to the riz PyROA RM results into the JHK regime corresponding to Figures 3.16 and 3.15 respectively. Here $\beta_{best} = 1.37 \pm 0.36$. This allowed lag predictions in Table 3.16 to be made.

laws fitted to the riz data-points. The best-fit power law exponent was derived by fitting a linear function to the logarithmic relation of the riz filters as done in Figure B.18 for PyROA. This generated a preferred exponent value $\beta = 1.12 \pm 0.20$ which is consistent with the expected thin disc relation and the preceding analysis when the uncertainty is taken into consideration (although it is still less consistent than the PyROA RM results).

Following the approach done in the PyROA analysis, Figure 3.23 shows the $\tau - \lambda$ re-

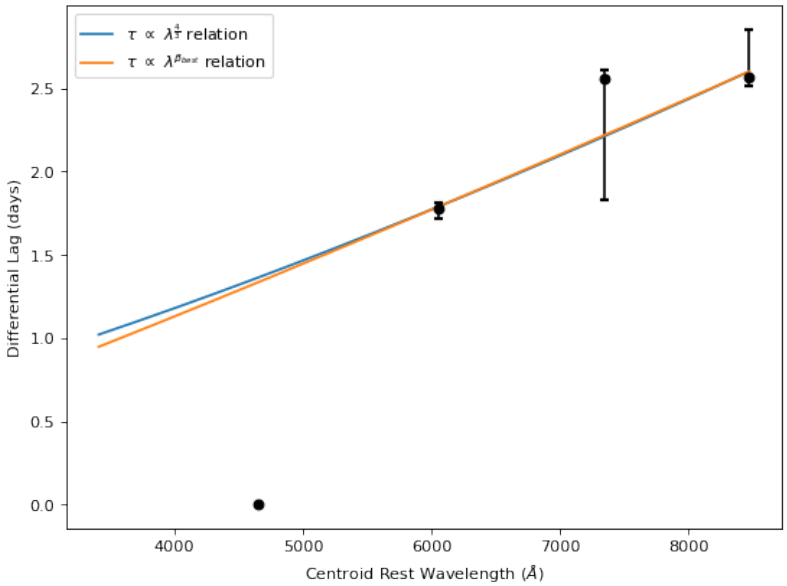

Figure 3.22: $\tau \propto \lambda^{\beta}$ power laws fit to the Javelin lag estimates. We have fitted the best-fit $\beta = 1.12 \pm 0.20$ and the thin disc model $\beta = \frac{4}{3}$ respectively.

lation with the riz data points shifted down by a constant value of 1.33 days so as to

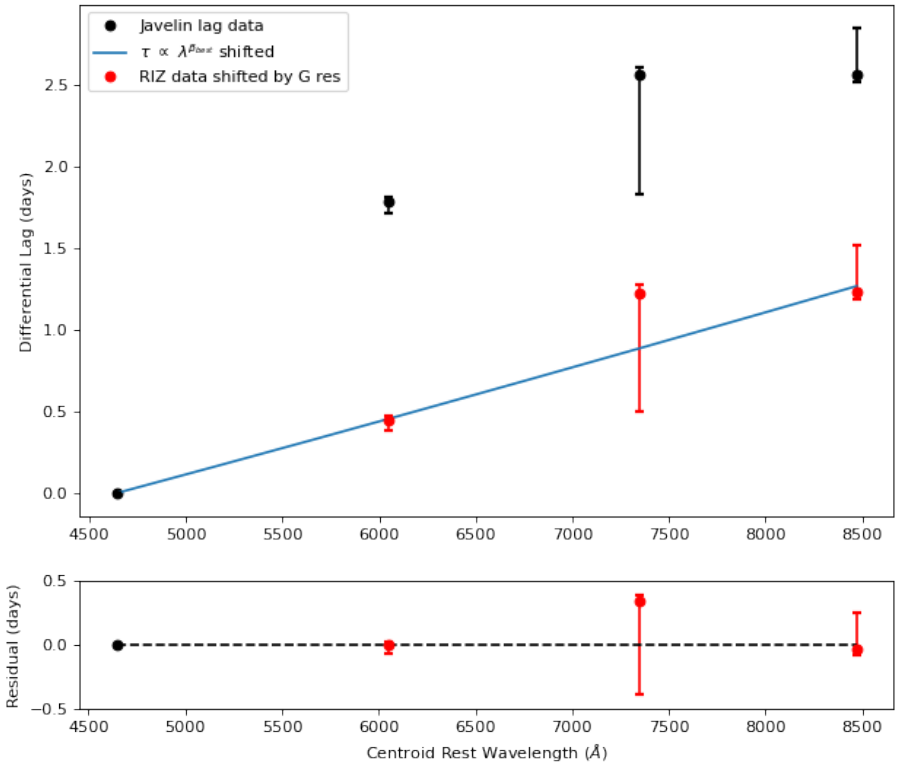

Figure 3.23: The scenario where the discontinuity in the lag estimates is assumed to be erroneous. Here the riz data points have been shifted down by the G band residual and the best fit power law $\tau \propto \lambda^{\beta}$ with $\beta = 1.12 \pm 0.20$ is shown.

get a continuous best-fit power law through the G data point. This is done to represent the realistic differential lags expected in the scenario that the discontinuity seen in Figure 3.22 is erroneous. This generated expected differential lags with respect to the G band which are consistent with those obtained from the PyROA analysis and those predicted using the X_{new} values as shown in Table 3.15. As such, the conclusion from the PyROA analysis that 1H 2106-099 does not likely display the 'accretion disc size problem' (in the event that the discontinuity is erroneous) is supported by Javelin. So too is the indication that the lag predictions made with the X_{new} values are more accurate than those made following the traditional approach of $X = 4.96$ for AGN not displaying the 'accretion disc size problem'. As done for the PyROA analysis, the power laws fit in the scenarios that the discontinuity between the g and riz filters is erroneous and physically reflected in the accretion disc are extrapolated so as to obtain lag predictions in the JHK regime as shown in Figure B.23. In both cases the thin disc and best-fit power laws with $\beta = 1.12 \pm 0.20$ are fit and the lag predictions for the best-fit power laws are shown in Table B.7. As can be seen the sets of predictions made using the thin disc and best-fit power laws are very

similar over these wavelengths and the predictions obtained by Javelin are consistent with those made by PyROA in the previous analysis.

Table 3.18 shows the bolometric luminosity estimates made by normalising the simulation for the accretion disc spectrum for 1H 2106-099 onto each of the ugriz photometric data-sets as done for 3C 273. As can be seen, the estimates obtained for all ugriz filters are all within $\sim 2\times$ the value obtained in Landt et al (2011) (stated in Table 3.1). This is a significant difference and indicates that the discontinuity in the lag estimates could be a result of contamination resulting in an erroneously large bolometric luminosity estimate.

Filter	L_{bol} (ergs^{-1})
U	6.7×10^{44}
G	9.9×10^{44}
R	2.0×10^{45}
I	2.5×10^{45}
Z	2.7×10^{45}

Table 3.18: Bolometric luminosity estimated made for 1H 2106-099 using each of the LCO filters used in the campaign. An estimate $L_{bol} = 1.3 \times 10^{45}ergs^{-1}$ was obtained in Landt et al (2011).

Figure 3.24 shows the absolute lags and residuals obtained by PyceCREAM plotted against the rest frame centroid wavelengths of the ugriz filters. As can be seen, the obtained lag estimates show a perfect thin disc relationship with best-fit $\beta = 1.34 \pm 0.01$ and does not reproduce the discontinuity obtained in the PyROA and Javelin RM results. However, this is not surprising as PyceCREAM's accretion disc transfer function mode fits a thin disc relationship by definition meaning the thin disc relationship obtained does not say much about the structure of the accretion disc. The magnitude of the lag estimates obtained by PyceCREAM are a factor ~ 2 larger than the predictions made with $X = 4.96$ and a factor $\sim 2 - 3$ larger than the predictions made with the X_{new} values and the shifted Javelin and PyROA lag estimates. This would indicate that 1H 2106-099 displays the 'accretion disc size problem' in contrast to the shifted PyROA and Javelin RM results. This fits in with observations made in Chapter 2 about the tendency of PyceCREAM to produce larger lag estimates than PyROA. This is on account of PyceCREAM's ability to derive its own driving light-curve and the likely effect this has on the algorithm assuming a scaled up accretion disc with respect to the other algorithms. Interestingly the PyceCREAM lag estimates are more similar in magnitude to the PyROA and Javelin unshifted riz lag estimates being a factor $\sim 0.5 - 1$ smaller. Since PyceCREAM

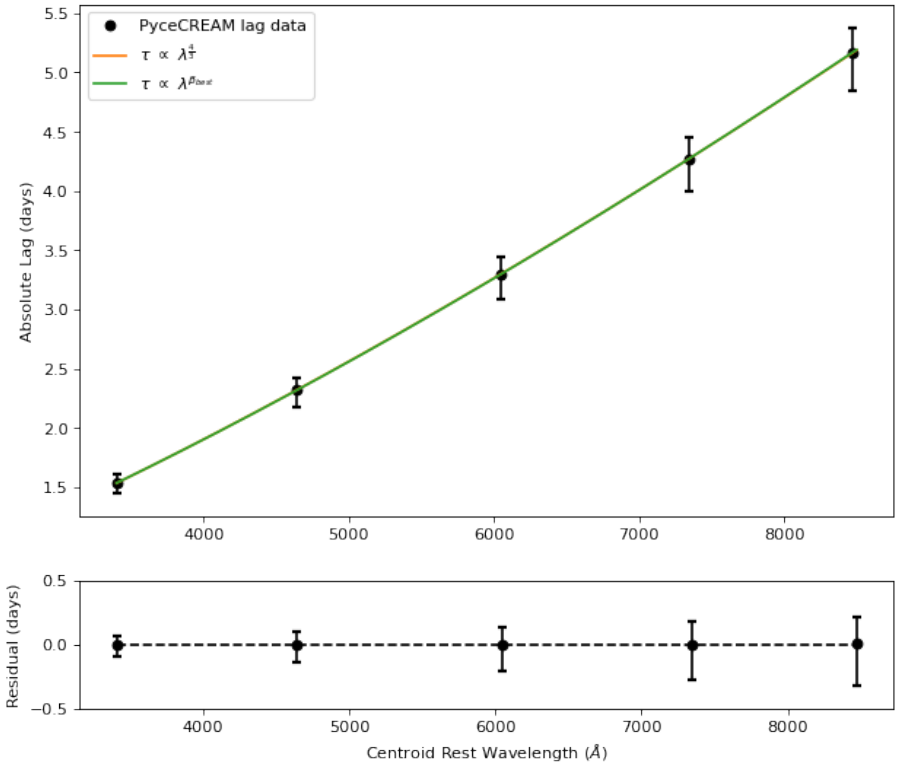

Figure 3.24: $\tau \propto \lambda^{\beta}$ power laws fit to the PyceCREAM lag estimates with $\beta = \frac{4}{3}$ and a best-fit $\beta = 1.34 \pm 0.01$.

forces an accretion disc spectral fit it will be unable to detect the discontinuity apparent in the PyROA and Javelin results. If this discontinuity is anomalous, as indicated by the erroneous bolometric luminosity estimates in Table 3.18, the PyceCREAM results may therefore be more accurate than the Javelin and PyROA estimates.

To test this we derived a second set of bolometric luminosity estimates for 1H 2106-099 using the lag estimates in Table 3.16. This is possible for the PyceCREAM results as the algorithm returns absolute lag estimates rather than differential lag estimates. These bolometric luminosity estimates were obtained by reversing the method with which we obtained our lag predictions using the absolute lag estimates for each filter as the input and a value $X \sim 6.9$ to scale the accretion disc to make it consistent with the larger lag estimates made by PyceCREAM. This returned consistent bolometric luminosity estimates for each of the lags in Table 3.16 with an average value $L_{bol} = 1.26 \times 10^{45} \text{erg} s^{-1}$ which is almost exactly the same as the value measured in Landt et al (2011). This indicates that the PyceCREAM results are accurate and that the discontinuity seen in the PyROA and Javelin results is likely anomalous.

Overall, the consistency in the bolometric luminosity estimate derived from the Pyce-

CREAM RM results indicates that the discontinuity seen in our PyROA and Javelin lag estimates is likely a result of contamination. This also suggests that 1H 2106-099 displays the 'accretion disc size problem' like 3C 273 although this is not clear due to the strong consistency in the shifted PyROA and Javelin lag estimates with the lag predictions made with the X_{new} values (which these results indicate could be a more accurate method than the standard approach with $X = 4.96$). However, without being able to identify a potential source for this contamination, there is a possibility that the observed discontinuity could reflect a discontinuity in the structure of the accretion disc in contrast to the continuous thin disc model adhered to by 3C 273. Our PyROA and Javelin analysis revealed that the ug and riz data points each fit well to thin disc power laws $\tau \propto \lambda^{\frac{4}{3}}$ but with different amplitudes. This could suggest that the ug and riz emitting regions of the accretion disc could exist in disconnected rings. A model similar to this is put forward by Nixon et al (2012) which argues that accretion discs tilted with respect to the rotation axis of their spinning SMBH would likely break apart into separate rings under the stress. In the absence of any more evidence this explanation is just conjecture but is is hoped the physicality of the discontinuity in the 1H 2106-099 data will be tested by upcoming near-infrared RM campaigns.

As done for the PyROA and Javelin analysis, the best-fit thin disc relationship obtained by PyceCREAM was extrapolated into the JHK regime as shown in Figure B.25. This enabled lag predictions to be made for the JHK bands stated in Table B.6. It is hoped that future near-infrared RM campaigns on 1H 2106-099 would help provide a preference between the thin accretion disc indicated by the PyROA and Javelin RM results or the scaled up accretion disc indicated by the PyceCREAM results.

As explained in the Introduction, the traditional theory for light-curve reprocessing in the accretion disc of AGN follows the lamp-post model and typically assumes the driving light-curve occupies the X-ray regime. However, accretion disc RM of NGC 5548 carried out by Fausnaugh et al (2017) with PyceCREAM revealed a poor match between the model driving light-cure and the measured hard and soft X-ray light-curve data suggesting the driving light-curve may not be in the X-ray regime. Similar investigations of NGC 5548 by Gardner and Done (2017) revealed that reprocessing of the measured hard X-ray light-curve data into the optical regime produced light-curves with too short a lag and too much short timescale variability. Instead, Gardner and Done (2017) suggest the far UV as an alternative for the driving light-curve. To test the suitability of the UV regime

as the driving light-curve in 1H 2106-099, we superimposed the model driving light-curve obtained by PyceCREAM in Figure 3.18 onto the measured U band data after normalising the U band data around a common offset and scale as the driving light-curve as shown in Figure 3.25. As can be seen, a relatively poor match is obtained with the majority of the U band data points existing outside the uncertainty limits of the model driver. In particular, the U band data appears to lag with respect to the driver. This does not necessarily rule out the UV as the driver particularly as the far-UV regime identified by Gardner and Done (2017) was not sampled in our investigation and, being at a shorter wavelength than our U data-set, would be expected to be more consistent with the model driver.

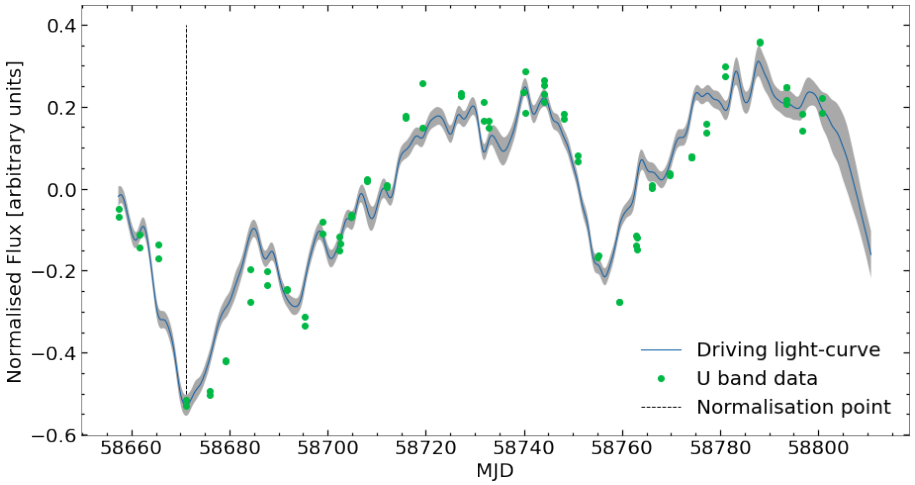

Figure 3.25: 1H 2106-099 U band data-set superimposed onto the model driver from PyceCREAM. As can be seen a relatively poor match is obtained.

It is apparent that the results obtained for 3C 273 and 1H 2106-099 using Javelin are less consistent with the rest of the analysis than the results obtained using PyROA. In addition, the Javelin lag estimates generally had larger uncertainties. This is likely a problem of convergence, despite the fact Javelin was run with double the number of iterations as PyROA, which is suggested by the wide distributions obtained for 3C 273 and the bimodal distributions obtained for 1H 2106-099. This reinforces the convergence problem highlighted for Javelin in Chapter 2. A key reason for this is likely the fact that Javelin fits top-hat transfer functions which introduces two additional parameters per light-curve compared to the Dirac delta fits performed by PyROA. A Dirac delta transfer function forces the algorithm to maintain a consistent shape for all the light-curves in the set which will impose greater constraints on the fit compared to a top-hat transfer function. Javelin's Gaussian process method may also contribute to the poorer constraints although it would

be largely mitigated by the preliminary fitting done to calibrate the parameters (as explained in Chapter 2).

This problem appears to have been exacerbated in 3C 273 due to the relatively featureless form of the light-curve data which would further loosen the constraints on the fit. For 1H 2106-099, the problem appears to be linked to the U band data-set which, as a result of its poor cadence, would also provide a lack of constraints on the fit. Our PyROA 3C 273 analysis also reproduced the over-fitting problem we found in Chapter 2 which we attributed to the large magnitude of the noise in our light-curves relative to the fitted signal in Figure 3.7. As in Chapter 2, we found the solution to this over-fitting was to increase the blurring by widening the Gaussian window width Δ. Therefore it appears that for less well-structured and poorly sampled light-curves, PyROA outperforms Javelin provided a large degree of blurring is placed on the PyROA fit. To get an improved performance with Javelin, it helps to add additional constraints to the fit as we tried to do with restrictions to the lag and decorrelation timescale spaces. With improved computing power, running Javelin with more iterations would also help it to converge better.

Our 1H 2106-099 analysis reproduced PyceCREAM's preference for a scaled up accretion disc relative to PyROA which we attributed to its ability to infer a driving light-curve. The strong agreement obtained by the bolometric luminosity derived from the PyceCREAM lag estimates with the value measured by Landt et al (2011) also agrees with out conclusion in Chapter 2 that PyceCREAM appears to be more suitable in the accretion disc RM regime than Javelin and PyROA. These results also indicate that the forced thin disc spectral fit done by PyceCREAM may make the algorithm less strongly effected by contamination in the light-curve data compared to PyROA and Javelin.

3.5 Summary:

In this Chapter we performed the first accretion disc RM analysis of 3C 273 and 1H 2106-099 with the algorithms Javelin, PyceCREAM and PyROA. We used the lag estimates obtained to investigate the accretion disc structure to compare to previous findings and to obtain lag predictions for the near-infrared JHK bands to be tested by upcoming RM campaigns. We also explored the performances of the three algorithms for both sets of light-curve data.

- We found a slightly shallower spectral power law exponent $\beta \sim 1$ than expected for

3C 273 which is nevertheless consistent with our unapproximated thin disc model simulation. This suggests 3C 273 conforms to the thin disc model and appears to display an accretion disc with a factor $\sim 2-3$ larger than expected.

- We found jet contamination estimates in the optical as well as timescales for the accretion disc and radio jet in 3C 273 consistent with previous findings.

- We found an unexpected discontinuity in the PyROA and Javelin lag results and spectrum of 1H 2106-099 which, if real, could indicate a discontinuous accretion disc.

- Our results suggest the discontinuity is anomalous and that the PyceCREAM lag estimates are most accurate, indicating the accretion disc in 1H 2106-099 is a factor ~ 2 larger than expected. However this is not entirely clear as we also estimate PyROA and Javelin lags, corrected for the discontinuity, in close agreement with predictions from the thin disc model.

- We found a problem of convergence with Javelin with the relatively featureless 3C 273 light-curves and the poor cadence U band in 1H 2106-099. We also found a tendency for PyROA to over-fit the 3C 273 data-set which was corrected by imposing a strong degree of blurring on the fit. Both these findings are consistent with our conclusion from Chapter 2.

CHAPTER 4

Design of RM Campaigns

With the arrival of the new Vera C. Rubin telescope the astronomical community is expected to receive a large influx of new RM data over the coming years. However, to my knowledge, currently no formal considerations have been made about how best to optimise the selection criteria of these data to make them most compatible for analysis by modern RM algorithms. To take full advantage of the new data to be collected, and to inform in general the ideal design of a RM campaign, it is therefore important to tailor the data selection criteria to minimise the uncertainties on the lag estimates made by RM algorithms. In particular, the two most relevant selection criteria for observing campaigns to consider are the length of the observing period and the cadence (ie. the time separation between consecutive observations).

To obtain accurate lag estimates it is preferable for the observing period to be long as this means the expected lag can be sampled more often and the chances to catch pronounced variability features are increased. In addition, it is preferable for observing campaigns to have shorter cadence data as this means the expected lag period can be sampled more intensely. However, due to resource constraints, RM campaigns must often prioritise one of these criteria over the other, choosing either longer observing periods less frequently sampled or shorter observing periods more frequently sampled. In this chapter we will attempt to make the first determinations about the dependence of the uncertainties on lag estimates made by modern RM algorithms to the length of the observing period and

the average cadence of the light-curve data. This will be done with the aim of informing future RM campaigns about the data criteria they should be selecting for to get the most accurate results for analysis.

4.1 The data-sets

The following investigation is based on the dust RM campaigns Koshida et al (2014) and Minezaki et al (2019). These studies use the near-infrared K band as the torus emission and the V band and a combination of the I and R bands for the accretion disc emission for Koshida et al (2014) and Minezaki et al (2019) respectively.

Koshida et al (2014) is comprised of a sample of 17 type 1 AGN's observed by the multicolour imaging photometer (MIP) located on the MAGNUM telescope, Hawaii. This data-set is relatively homogeneous, being entirely comprised of Seyfert 1 galaxies located at low redshifts $0.002 \leq z \leq 0.04$. All 17 objects were incorporated into my investigation. Minezaki et al (2019) was a larger study comprised of a sample of 31 type 1 AGN's also observed by the MIP mounted on the MAGNUM telescope. From this sample, Minezaki et al (2019) were only able to detect an optical lag with respect to the K band for 25 objects. Of these objects, 3 produced inconclusive lag estimates from CCF analysis. Therefore, I incorporated the remaining 22 objects for which successful lag estimates could be obtained into my investigation. Minezaki et al (2019) is a higher redshift survey than Koshida et al (2014) and is more diverse, being comprised of AGN with larger redshift ranges $0.06 \leq z \leq 0.6$ and luminosity ~ 1.5 orders of magnitude greater in range than Koshida et al (2014).

Both studies obtained their lag estimates using a CCF method and the 'Rmap' mode of Javelin. For the purposes of investigating modern RM algorithms, we selected the lag estimates and uncertainties obtained by Javelin for analysis. We quote all lag estimates in the observer frame so that our results are consistent with the expected findings of observers. An additional consideration relevant for both studies is the accretion disc contamination subtraction. For the following analysis, we use the lag estimates derived from the $\beta = \frac{1}{3}$ subtraction as this exponent value is consistent with the thin disc model and so is a more standard choice.

By including both data-sets, we help ensure our investigation has a large amount of data relative to the near-infrared RM data available. We also introduce a large variety of AGN redshift and luminosity properties into the study. This should help reduce the

likelihood of bias appearing from an over-representation of a particular kind of AGN. The diversity of the combined data-set is shown in Figure 4.1 which demonstrates that our investigation will be sensitive to a large range of lag values ranging from $\sim 25 - 300$ days. However, it should be noted that this sensitivity decreases at larger lags likely due to the difficulty in obtaining good quality light-curve data at higher redshifts. Including both

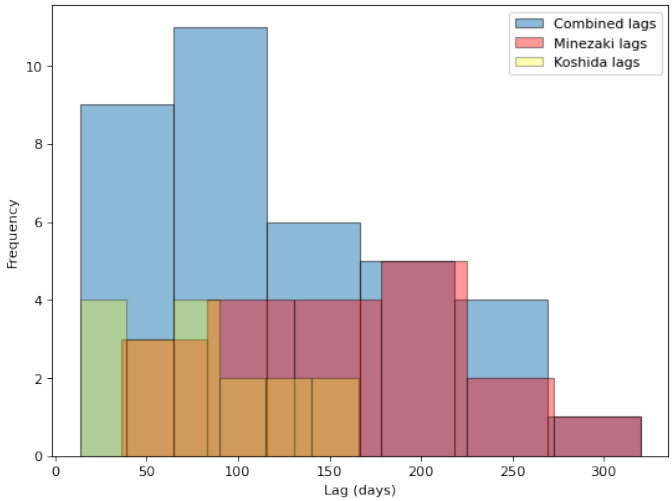

Figure 4.1: A histogram of the lag estimates contained within the Koshida et al (2014) and the Minezaki et al (2019) studies as well as the combined data-set. A large range of estimated lags is obtained by combining the two studies although the sensitivity drops off at longer lag estimates

high and low redshift AGN will also provide a useful comparison for the dependencies of the uncertainties on lag estimates in both redshift regimes. Our investigation could therefore help inform the selection of data during the transition to higher redshift campaigns.

4.2 Method

For the measure of the uncertainty in the lag estimate we decided to use the error relative to the magnitude of the lag estimate output by Javelin rather than the absolute lag uncertainty. Relative error is a more attractive parameter to measure lag uncertainty than absolute error as it is a more meaningful expression of the significance of the uncertainty on the measurement. In addition to this, our combined data-set showed a strong linear correlation between the magnitude of the estimated lag and the scale of the absolute error on that estimate as shown in Figure 4.2. This is likely a result of the Malmquist bias which means the higher redshift Minezaki et al (2019) survey is biased to select for larger, more luminous objects that generate longer lags in RM campaigns which, if not compensated

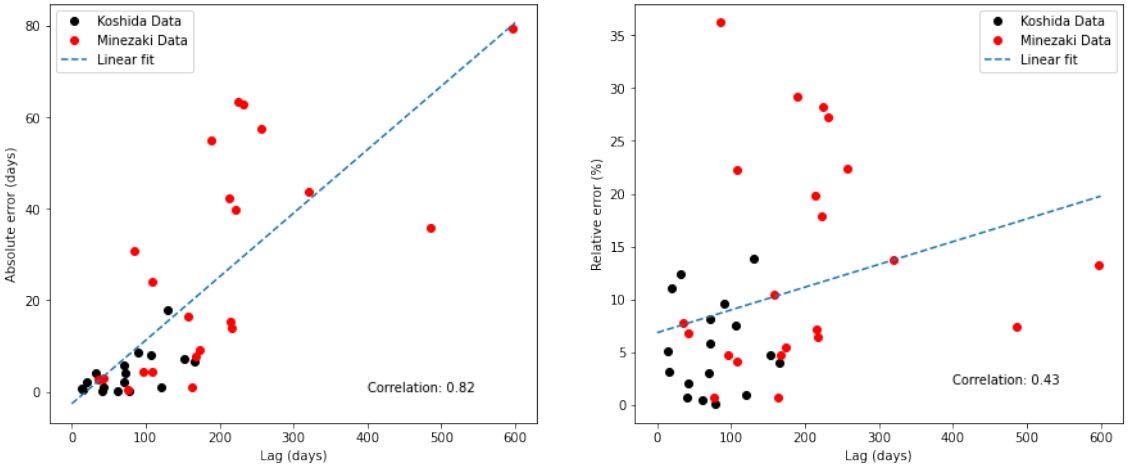

Figure 4.2: A demonstration of the correlation found between Javelin lag estimates and absolute/relative error estimates for Koshida et al (2014) and Minezaki et al (2019) datasets. The weakened correlation and fitted gradient with relative error justifies its use as the parameter for lag uncertainty. The correlations are determined by Spearman's rank.

adequately by an increased length of the observing period, would be expected to give less certain lag estimates. Figure 4.2 suggests that the use of relative error weakens the effect of the Malmquist bias on the uncertainty estimate meaning we can more effectively compare AGN across different redshift regimes. Observers should be aware of this effect during the transition to higher redshift campaigns.

For the investigation, we decided to use the length of the light-curve relative to the estimated lag as a parameter (which we represent as γ) rather than using the length of the observing period. This parameter is defined as

$$\gamma = \frac{t_N - t_0}{\tau}, \tag{4.1}$$

where $t_N - t_0$ is the length of the observing period for a light-curve consisting of N data points with an expected lag of τ. The light-curve length relative to the expected lag is a more meaningful parameter for measuring the uncertainty on lag estimates because the length of the observing period can be expected to have an effect on the uncertainty in lag estimates only in so far as it is relative to the expected lag. Having longer light-curve data relative to an expected lag means the expected lag is sampled more often and so more accurate estimates on the lag is expected.

Similarly, we decided to use the expected lag relative to the average cadence of the light-curve as a parameter (which we represent as ϵ) for the investigation rather than the

absolute average cadence. This parameter is defined as

$$\epsilon = \frac{\tau}{\langle t_n - t_{n-1} \rangle}, \tag{4.2}$$

where $\langle t_n - t_{n-1} \rangle$ is the average cadence in the light-curve data. The expected lag relative to the average cadence is a more meaningful parameter for measuring the uncertainty on lag estimates than the absolute average cadence which is expected to have an effect on the uncertainty in lag estimates only in so far as it is relative to the expected lag. Having shorter average cadences relative to the expected lag means the expected lag period is more heavily sampled and so more accurate lag estimates are expected.

We also decided to include parameters to account for the influence of data gaps on the uncertainties of lag estimates. Both the frequency and size of the data gaps would decrease the proportion of the light-curve covered by data and so we decided to introduce two new parameters to account for these variables. We define the density of data gaps (represented as ρ) as the number of gaps relative to the length of the observing period. Similarly, we define the average gap size relative to the light-curve length (represented as δ).

A subtlety that should be addressed is the distinction between data gaps and regular cadence in the light-curve data. To quantitatively define this we generated histograms of the time separation between consecutive observation for each object in our study. We defined two definitions for the boundary between gaps and cadence corresponding to the upper 1σ and 2σ boundaries for the histograms. This was done to determine how sensitive the following analysis would be to the subjective choice of how many σ to define the gaps in relation to. In addition, the following analysis was also run with a third definition of gaps defined as all inter-data time separations greater than 20 days applied uniformly across all objects. This is to act as a control case to assess the effectiveness of the statistical definition of gaps defined above. A detailed explanation of our method for defining gaps is given in Appendix B.4.1.

One final complexity introduced by the Koshida et al (2014) data-set is the fact that 10 out of the 17 objects in this study had lag estimates which were determined as weighted means over the estimates from multiple observing epochs. This would introduce an additional dependence on the uncertainties of the lag estimates. The multi-epoch data was kept in the study and was treated as single continuous light-curves where the data in overlapping regions were only included once. The light-curve length for the multi-epoch

data was determined as a sum of the length of the individual epochs and the remaining parameters were averaged over all epochs.

4.3 Analysis and Results

The following analysis is focused on investigating the relation between the relative error on lag estimates and the γ and ϵ parameters. We focus on the correlation of these parameters with the relative error and the form of their trend. Determining the strength of the correlation gives an indication of which of the two parameters RM campaigns should prioritise to reduce the relative error. We use Spearman's rank from the 'stats' module in 'scipy' as a measure of the correlation strength. Obtaining a reasonable fit to the relation of the γ and ϵ parameters with relative error will help us to determine estimates for the optimum parameter values which yield the lowest relative errors beyond which diminishing returns are obtained (the so-called 'sweet spot'). Having a reasonable fit to these relations would also allow RM campaigns to estimate the relative errors they can expect from light-curves of a particular length and cadence relative to an expected lag. Figures 4.3 and 4.4 show the obtained relations between the relative error and the light-curve length relative to the expected lag (ie. γ) and the expected lag relative to the average cadence (ie. ϵ) respectively using 1σ gap definition as detailed in the Appendix. We chose the 1σ definition arbitrarily as we found no significant difference between the 1σ and 2σ definitions as seen in Figure B.29 in the Appendix. The expected negative correlations were obtained and the trends also indicate asymptotes with both axes which makes intuitive sense. An asymptote with the y-axis is to be expected as the relative error would tend to infinity in the limit that the light-curve length tends to zero or the average cadence tends to infinity (ie. the limit where no data is present). Likewise, an asymptote with the x-axis is to be expected as the relative error would not be expected to ever reach zero. The magnitude of the obtained correlations would suggest that the light-curve length relative to the expected lag has a larger effect on the relative error than the lag relative to the average cadence. Figures 4.3 and 4.4 are fit with a logarithmic function of the form $y = \ln\left(\frac{|x+a|^2}{|x-b|^2}\right)$. This function was selected as a logarithmic function matches the asymptotic expectations mentioned above. It should be mentioned that the function diverges from the expected asymptote outside the data range but was selected as it appears to fit the 'sweet spot' well. However, as this investigation is based on real data, there is likely significant covariance between the parameters. Examples of these covariances are demonstrated in Figure 4.5.

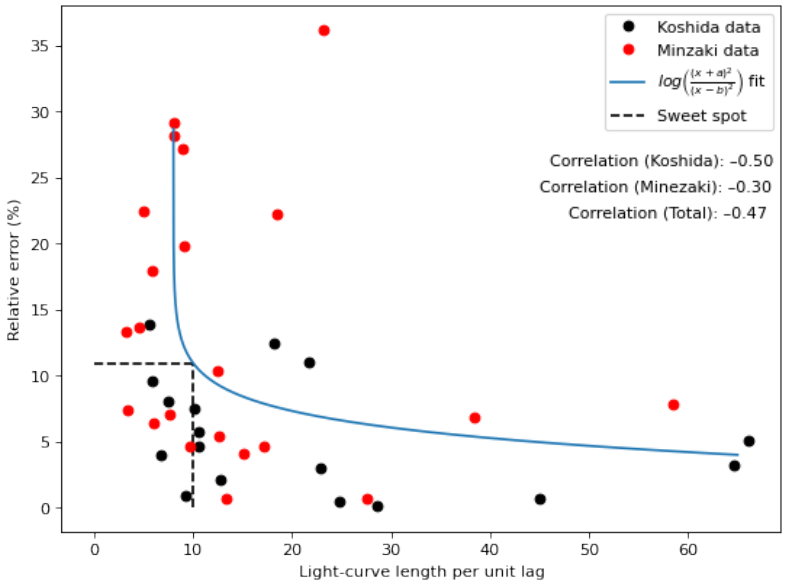

Figure 4.3: The derived relationship between the relative error on Javelin lag estimates and the 'light-curve length relative to the expected lag' (parameter γ) for the Koshida et al (2014) and Minezaki et al (2019) data-sets. The Spearman's rank correlation measurements are shown. A logarithmic function is fit to the data and the 'sweet spot' is derived as the location where the gradient of the function is -1.

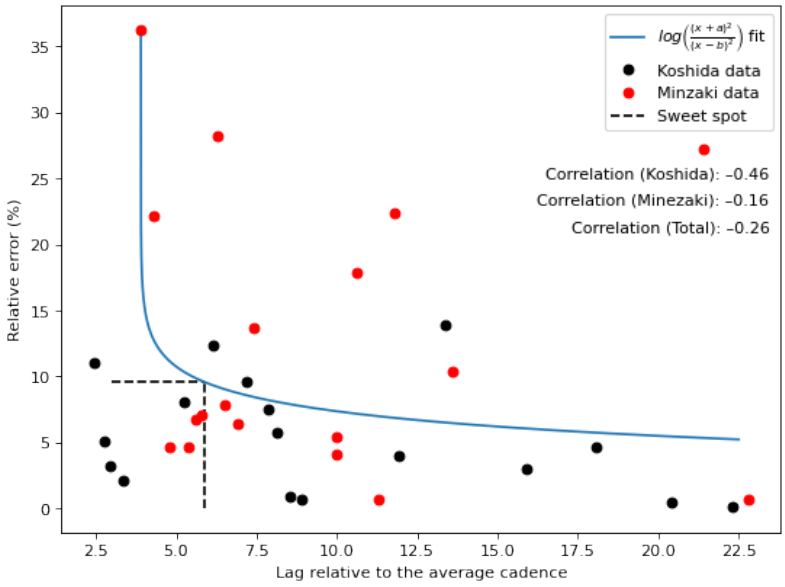

Figure 4.4: The derived relationship between the relative error on Javelin lag estimates and the 'lag relative to the average cadence' (parameter ϵ) for the 1σ gap definition. A logarithmic function is fit to the data and the 'sweet spot' is shown.

In particular, we found significant correlation between the average cadence and light-curve length with the γ and ϵ parameters. This highlights the fact that longer light-curve lengths relative to expected lags can be obtained by either having longer observing periods

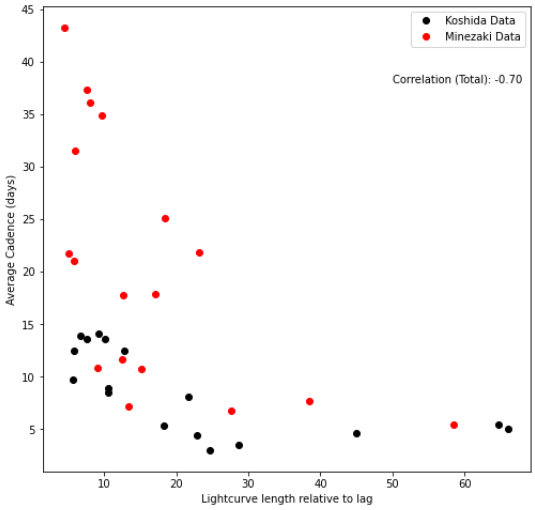

(a) The covariant relationship between the average cadence with the γ parameter for the Koshida et al (2014) and Minezaki et al (2019) data-sets with the 1σ gap definition given in the Appendix.

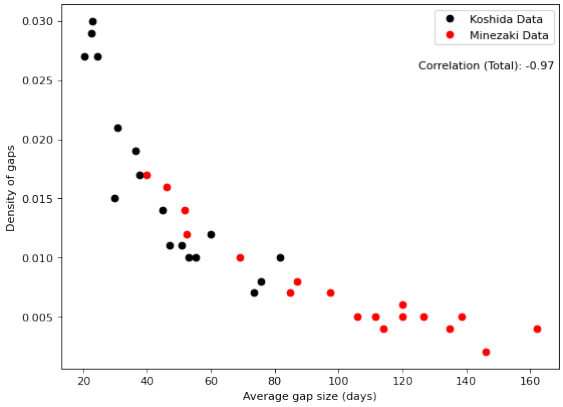

(b) The covariant relationship between the average gap size and gap density parameter for the Koshida et al (2014) and Minezaki et al (2019) data-sets. Here the results are shown for the 1σ gap definition defined in Section 4.2.

Figure 4.5: Examples of covariant relationships between light-curve parameters.

for a given lag or by having shorter expected lags for a given light-curve length (which can be expected to be more densely sampled). Similarly, longer expected lags relative to the average cadence can be obtained by having shorter cadence data for a given expected lag or by having longer lags for a given cadence (which can be expected to require longer observing periods).

In order to get a more meaningful conclusion we decided to produce sub-samples from the combined data-set where one or the other of the γ or ϵ parameters is controlled. This was done using the 1σ gap definition. The first sub-sample was produced by sampling Figure 4.6 along a narrow vertical slice of ± 1.5 δ units which selects objects with approximately the same number of data points sampling their expected lag periods. The first sub-sample was used to determine the dependence of relative error on the light-curve length relative to the lag whilst keeping the effect of cadence on the relative error approximately controlled. The second sub-sample was produced by sampling Figure 4.6 along a narrow horizontal slice of ± 2 γ units which selects objects with approximately the same sampling frequency of the expected lag in their observing period. The second sub-sample was used to determine the dependence of relative error on the expected lag relative to the average cadence whilst keeping the effect of light-curve length on the relative error approximately controlled. The slices in Figure 4.6 were made in the densest part of the

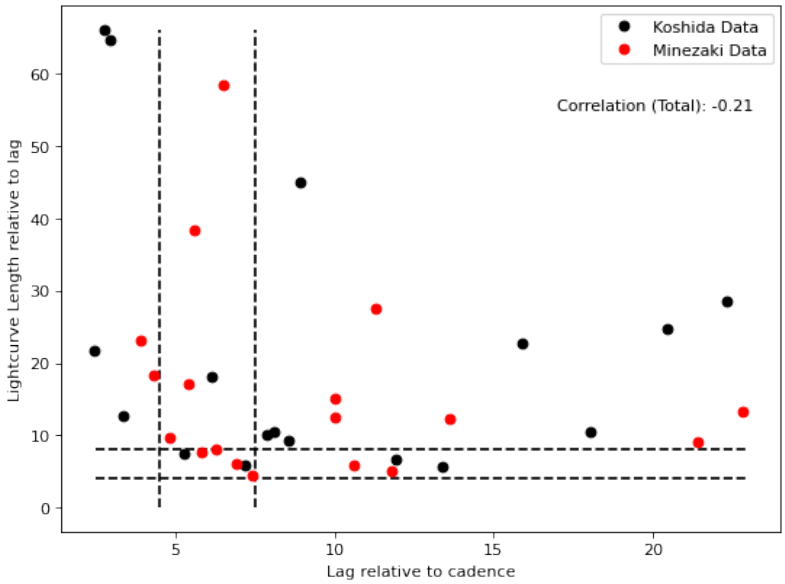

Figure 4.6: The covariant relationship between the 'light-curve length relative to expected lag' and the 'lag relative to expected cadence' parameters for the Koshida et al (2014) and Minezaki et al (2019) data-sets. Here the results are shown for the 1σ gap definition defined in Section 3.2 and the Spearman's rank correlation measurements are shown. The dashed lines indicate the sub-samples selected for Figure B.32

parameter space in order to maximise the amount of data in the sub-samples. The width of these slices were determined so that approximately the same number of data points would be selected for each sub-sample as the number of data points would likely effect the strength of the correlations obtained. It should also be noted that all the objects from the Koshida et al (2014) data-set selected had 1 epoch meaning the sub-sample controls for the number of epochs.

The resulting sub-samples generated truncated versions of Figures 4.3 and 4.4. We found a weak negative correlation with relative error still apparent for the γ parameter but got no significant correlation for ϵ. Therefore these results agree with the conclusion from the full data-set in suggesting that having longer observing periods relative to the expected lag is more important in reducing the relative error on lag estimates in RM campaigns than having more densely sampled lag periods.

To get an indication of the trend between the γ and ϵ parameters with the relative error, we decided to use the full data-sets due to the lack of data in the sub-samples. The logarithmic functions in Figures 4.3 and 4.4 were fit to the data with some difficulty (due to the scatter) using 'scipy' curve-fit module. We define the 'sweet spot' to be the parameter values which correspond to a gradient of magnitude 1 for the fitted function

in Figures 4.3 and 4.4. Beyond this point increases (decreases) in the light-curve length (average cadence) will give diminishing returns because decreasing the relative error by the same amount will require greater increases (decreases) in the length of the observing period (average cadence). The 'sweet spot' in Figure 4.3 corresponds to a light-curve length $\sim 10\times$ the expected lag which has an associated relative error of $\sim 11\%$. Likewise, the 'sweet spot' in Figure 4.4 corresponds to an average cadence $\sim 6\times$ smaller than the expected lag which has an associated relative error of $\sim 10\%$.

4.4 Discussion

Figure B.29-B.31 shows a large difference between the results obtained using the statistical definition of gaps and the definition of gaps being larger than 20 days. The statistical definition generated clearer trends with a stronger correlation. This highlights the unsuitability of using a blanket gap definition which would likely introduce gaps into the cadence definition and thereby increase the scatter to obscure the trend. Interestingly, no significant difference in correlation was found between the 1σ and 2σ definitions of gaps which indicates that our statistical definition is reasonably stable to subjective choices. This provided the motivation for continuing the analysis done in the previous section with just the 1σ definitions.

We obtained significantly weaker correlations for the Minezaki et al (2019) data-set than Koshida et al (2014) for all relative error relations. This is likely a result of the fact that Minezaki et al (2019) covered a much larger range of redshift and luminosity meaning it likely contains unidentified parameters which vary between different types of AGN, which are largely controlled for in the more homogeneous Koshida et al 2014 study, and act to introduce scatter into the relations. This scatter is more significant for the cadence relation in Figure 4.4 than the light-curve length relation in Figure 4.3 meaning it may have effected our final conclusion regarding the relative importance of these two parameters.

Both the data-sets investigated are obtained from near-infrared RM campaigns which would likely make the data atypical compared to other RM regimes. In particular, infrared RM can be expected to detect longer lags than the other regimes which means it is likely that the combined data-set is biased to have longer observing periods and longer average cadences. As such, the relative unimportance found between the ϵ parameter and the relative error could be a result of the fact that the data-set did not sample small

enough cadences for there to be a significant effect on the relative error. This effect can be expected to be more pronounced for higher redshift surveys which would be expected to detect even longer lags and could provide another explanation for the significantly weaker correlations found in the Minezaki et al (2019) data-set. To generalise the results of this investigation, future investigations should include both accretion disc and BLR RM studies. As a result of the fact real RM data was used in this study, there is significant covariance between the parameters due to our consequent inability to control all variables. There is also a strong possibility that unidentified variables also exist in the data. Whilst efforts were made to control the covariance between the γ and ϵ parameters in the final analysis, this was done in a crude way due to the small sample size which meant neither parameter was fully controlled for in the sub-samples taken. Both of these issues could be addressed by future investigations incorporating synthetic data into their study. This would allow parameters to be definitely controlled and an arbitrarily large number of data points to be generated.

4.5 Summary

In this chapter we attempted to measure the effect of the length and cadence of light-curve data relative to an expected lag on the uncertainty associated with lag estimates made by RM algorithms. This was done using dust RM data-sets with the intention of informing future RM campaigns on selecting the optimal light-curve data. To do this we measured the strength of the light-curve parameters with relative error and fit functions to the relations to estimate their optimum values.

- Our results indicate that the light-curve length relative to the expected lag has a larger influence on the uncertainties of lag estimates than the expected lag relative to the average cadence.

- We estimate the optimum value of the light-curve length to be $\sim 10\times$ the expected lag and the optimum cadence to be $\sim 6\times$ smaller than the expected lag which had associated uncertainties of $\sim 11\%$ and $\sim 10\%$ respectively.

CHAPTER 5

Conclusions

The main aim of the thesis was to perform the first accretion disc reverberation mapping analysis of the AGN 3C 273 and 1H 2106-099 using the RM algorithms Javelin, PyCREAM and PyROA so as to obtain insight into the structure of the accretion disc and to compare the performance of the algorithms in the process. Linear fits to the spectrum of 3C 273, the results of the PyROA and combined PyROA and Javelin RM analysis and the normalising of the spectrum to our photometric light-curve data all independently suggest that the spectral power law in 3C 273 has a slightly shallower exponent $\beta \sim 1$ than expected by the approximated thin disc model value $\beta = \frac{4}{3}$ in contrast to previous findings. This shallower exponent allowed us to obtain predictions for the mean BLR lag which are in better agreement with previous estimates than predictions made with the standard thin disc model value. However, a simulation we created of the accretion disc spectrum in 3C 273 based on the more physically meaningful unapproximated thin disc model (with a boundary condition at r_{ISCO}) returned a shallower exponent with reasonably good agreement with the findings of our analysis. We therefore conclude that 3C 273 likely conforms to the thin disc model in which case it appears to display the 'accretion disc size problem' with a scale $\sim 2 - 3$ larger than expected. The PyROA and Javelin RM results for 1H 2106-099 revealed an unexpected discontinuity which is reflected in the spectrum and which we cannot attribute to any specific contamination. This may indicate a discontinuous accretion disc although we do not have enough evidence to conclude this.

Investigating the possibility that the discontinuity is anomalous, we corrected the Javelin and PyROA results for the discontinuity to obtain lag estimates in near perfect agreement with the unapproximated thin disc model predictions without an up-scaled accretion disc. The PyceCREAM results revealed no discontinuity as the algorithm assumes a continuous thin disc power law although we obtained accurate bolometric luminosity estimates using the PyceCREAM lag estimates indicating these lag estimates may be accurate and that the discontinuity is anomalous. These results suggest 1H 2106-099 has an accretion disc scaled up by a factor ~ 2 larger than expected which we consider to be more accurate than the accretion disc scale suggested by Javelin and PyROA due to the bolometric luminosity findings although this is not entirely clear. Using our results we made lag predictions for the dust forming JHK regimes of the accretion disc both with the standard $\beta = \frac{4}{3}$ and the shallower $\beta \sim 1$ in 3C 273 and with and without the discontinuity in 1H 2106-099. This will allow our conclusions to be tested by upcoming near-infrared RM campaigns. Overall we found the Javelin results to be less constrained than the other algorithms meaning we consider its lag estimates as less reliable.

Our results likely show two more examples of AGN which display the 'accretion disk size problem' which further validates the existence of this phenomenon although this is less clear for 1H 2106-099. We also concluded that both the AGN we investigated conform to the thin disc model meaning our results support the standard description of AGN accretion discs. Future investigations should investigate a wider spectral range in 1H 2106-099 in order to help identify the likely contamination we found. RM should also be done on both sources in the near-infrared JHK bands to test our predictions.

A secondary aim of the thesis was to investigate how the uncertainties on lag estimates made by Javelin depended on the length and cadence of the light-curve data in the dust RM regime. Investigations on two dust RM campaigns suggested that the light-curve length relative to the expected lag has a more significant effect on the size of the uncertainties than the cadence relative to the lag. We estimated the optimum light-curve length to be $\sim 10\times$ the expected lag and the optimum cadence to be $\sim 6\times$ smaller than the expected lag which had associated uncertainties of $\sim 11\%$ and $\sim 10\%$ respectively.

Bibliography

Berton, M. et al 2018, A&A 614, 14

Bridle, A. H., Perley, R. A. 1984, Annual Review of Astronomy and Astrophysics, 22, 319

Brown, T.M. et al. 2013, Publications of the Astronomical Society of the Pacific, Volume 125, Issue 931, pp. 1031

Cackett E. M., Horne K., Winkler H., 2007, MNRAS, 380, 669

Cackett E.M., 2018, ApJ., 857, 53

Chan, J. H.-H., Millon, M., Bonvin, V., Courbin, F., 2020, A&A 636, A52

Collier, S. J., PhD thesis, Univ. St Andrews, *Measuring the Hubble constant from reverberating accretion disks in active galaxies*, 1998

Czerny, B. et al. 2015, Elsevier, 55, 7, pg 1806-1815

De Rosa, G. et al 2018 ApJ 866 133

Denney, K. D., Peterson, B. M., Pogge, R. W., et al. 2010, ApJ, 721, 715

Donnan , F R. , Horne , K. Santisteban , J V H. 2021 , *Bayesian analysis of quasar lightcurves with a running optimal average : new time delay measurements of COSMOGRAIL gravitationally lensed quasars* , Monthly Notices of the Royal Astronomical Society , vol. 508 , no. 4 , pp. 5449–5467

Dutan, I., PhD thesis, Rheinischen Friedrich-Wilhelms-Universitat Bonn, *Jets from Spinning Black Holes in Active Galactic Nuclei*, 2010

Edelson, R. et al 2019 ApJ 870 123

Edge, D.O., Shakeshaft, J.R., McAdam, W.B., Baldwin, J.E., Archer, S. 1959, MemRAS, 68, 37

Fausnaugh, M, M. et al 2016 ApJ 821 56

Fausnaugh, M, M. et al 2017, Continuum Reverberation Mapping of AGN Accretion Disks, Frontiers in Astronomy and Space Sciences, 4

Figaredo, S, C. et al 2020 AJ 159 259

Foreman-Mackey. et al. 2013, PASP 125 306

Gabanyi, K. E., Frey, S., Satyapal, S., Constantin, A., Pfeifle, R. 2019, A&A, 630, L5

Gardner, E., & Done, C. 2017, Monthly Notices of the Royal Astronomical Society, 470, 3591, doi: 10.1093/mnras/stx946

Gaskell, C. M., & Peterson, B. M. 1987, ApJS, 65, 1, doi: 10.1086/191216

Ghisellini, G. et al. 2017, Monthly Notices of the Royal Astronomical Society, 469, 255–266

Gillespie, D. T. 1996, Am. J. Phys., 64, 225

GRAVITY Collaboration, 2020,A&A 636, L5

Grossan, B., Remillard, R. A., Bradt, H. V., Brissenden, R. J., Ohashi, T. k Sakao, T. 1996, Ap.J. 457, 199+

Hastings, W. 1970. *Monte Carlo sampling methods using Markov chains and their application.* Biometrika, 57: 97–109

Hlabathe, S, M,. 2020, Monthly Notices of the Royal Astronomical Society, Volume 497, Issue 3, pg 2910–2929

Ishibashi, W., Courvoisier, T.J.L., 2009, A&A Volume 504, Number 1, 61-66

Jorstad, S. G., Marscher, A. P., Morozova, D. A., et al. 2017, ApJ, 846, 98

Kaspi, S. et al. 2000, Reverberation measurements for 17 quasars and the size-mass-luminosity relations in active galactic nuclei. Astrophys. J. 533, 631–649

Kelly, B. C., Bechtold, J., Siemiginowska, A. 2009, ApJ, 698, 895

Koshida, S. et al 2014 ApJ 788 159

Landt H., Elvis M., Ward M. J. et al. 2011 MNRAS 414 218

Landt H., et al., 2019, MNRAS, 489, 1572

Li, Y.R., Wang, J.M., Ho, L. C., Du, P., & Bai, J.M. 2013, ApJ, 779, 110

Li, Yan-Rong et al, 2016, American Astronomical Society, 831, 2

MacLeod C. L. et al., 2010, ApJ, 721, 1014

McHardy I. M., Koerding E., Knigge C., Uttley P., Fender R. P., 2006, Nature, 444, 730

McHardy I. M. et al., 2014, MNRAS, 444, 1469

Metropolis, N., Rosenbluth, A., Rosenbluth, M., Teller, A., and Teller, E. 1953, *Equations of state calculations by fast computing machines.* J. Chem. Phys., 21(6): 1087–1092

Minezaki, T., et al 2019 ApJ 886 150

Mudd D., Martini P., Zu Y., Kochanek C., Peterson B.M., Kessler R., Davis T.M., Hoormann J.K., King A., Lidman C. 2018, *Quasar accretion disk sizes from continuum reverberation mapping from the dark energy survey*, ApJ, 862:123

Mushotzky, R. F., Marshall, F. E., Boldt, E. A., Holt, S. S., and Serlemitsos, P. J. 1980, Ap. J., 235, 377

Netzer, H. 2015, ARA&A, 53, 365

Newville, M. et al. 2016, Astrophysics Source Code Library, record ascl:1606.014

Niedzwiecki, A., Zdziarski, A., Szanecki, M., 2016, American Astronomical Society, 821, 1

Nixon, C., 2012, American Astronomical Society, 757, 2

Peterson, B. *An introduction to active galactic nuclei*, Cambridge, New York Cambridge University Press, 1997, p. 1-5

Peterson, B. M., Wanders, I., Horne, K., et al. 1998, PASP, 110, 660

Peterson, B. M., Horne, K., 2004, Wiley, 325, 3

Peterson, B., et al. 2004, ApJ, 613, 682

Peterson, B. M., Grier, C. J., Horne, K., et al. 2014, ApJ, 795, 149

Remillard, R. A., PhD thesis, MIT, *The optical identification and spectral analysis of celestial X-ray sources*, 1985

Rybicki, G. B., Press, W. H. 1995 Phys. Rev. Lett. 74, 1060

Salpeter, E.E. 1964, ApJ, 140, 796

Schmidt, M. 1963, Nature, 197, 1040

Schmidt, M., & Green, R. F. 1983, ApJ, 269, 352

Seyfert, C. 1943, ApJ, 97, 28

Shakura, N.I., Sunyaev, R.A., 1973, Astr. Astrophys., 254, 22

Soldi, S. et al 2008, A&A 486, 411-425

Stalevski, M., Jovanovic, P., Popovic, L.C, Baes, M. 2012, MNRAS, 425, 2, 1576-1584

Starkey, D. A., Horne, K., Villforth, C. 2016, MNRAS, 456, 1960

Starkey, D., et al 2017 ApJ 835 65

Sturm, E. et al. 2018, Spatially resolved rotation of the broad-line region of a quasar at sub-parsec scale. Nature 563, 657–660

Terrell, J., 1967, Am.J.Phys., 45, 869

Trotta, R., 2016, *Bayes in the sky: Bayesian inference and model selection in cosmology*, CONTEMPORARY PHYSICS, 49(2), 71–104

Uttley P., McHardy I. M., Papadakis I. E., 2002, MNRAS, 332, 231

Wang, Jie, 2020, arXiv, *An Intuitive Tutorial to Gaussian Processes Regression*, doi: 10.48550/ARXIV.2009.10862

Welsh, W. F. 1999, PASP, 111, 1347

Xiong, D. et al 2017, ApJS 229 21

Yu Z., Kochanek C. S., Peterson B. M., Zu Y., Brandt W. N., Cackett E. M., Fausnaugh M. M., McHardy I. M., 2020,Monthly Notices of the Royal Astronomical Society, Volume 491, Issue 4, Pages 6045–6064

Yuan, Y, H. et al 2022, PASP 134 044102

Zel'dovich, Ya.B., Novikov, I.D. 1964, Sov. Phys. Dokl., 158, 811

Zhang, Zhi-Xiang. et al. 2019, ApJ 876 49

Zu, Y., Kochanek C. S., Peterson B. M., 2011, ApJ, 735, 80

APPENDIX A

Additional Explanation

A.0.1 MCMC

All three of the algorithms under discussion in the thesis use an MCMC approach. It will therefore be useful to briefly summarise the purpose and typical techniques of MCMC. The main purpose of MCMC is to obtain a set of samples of the parameters θ_i from the posterior distribution conditioned on a set of data D. The posterior distribution is defined by Bayes' equation

$$p(\theta|D) = \frac{p(D|\theta)p(\theta)}{p(D)}. \tag{A.0.1}$$

Here $p(D|\theta)$ is the likelihood function and $p(\theta)$ is the prior distribution which reflects prior knowledge about the values of θ. Typically uniform distributions are used to express a lack of prior knowledge about parameter values whilst peaked distributions are used to express preferred values. For the purposes of parameter optimisation, the evidence term $p(D)$ serves simply as a normalisation. For more information please see Trotta (2016).
The most widely used MCMC algorithm is the Metropolis-Hastings algorithm developed by Metropolis, N. et al (1953) and Hastings, W. (1970). This involves initialising at a certain position in the parameter space X_1 and then sampling subsequent proposal positions Y from a transition distribution $Q(X;Y)$ (which acts effectively as a prior). The transition distribution is commonly chosen as a multivariate Gaussian in the parameter

space centred at X_t for the t^{th} step in the Markov chain. The probability of acceptance for the proposal Y is defined as

$$P = \min\left(1, \frac{p(Y|D)}{p(X_t|D)}\frac{Q(X_t;Y)}{Q(Y;X_t)}\right), \tag{A.0.2}$$

and, if accepted, leads to an update in the Markov chain $X_{t+1} = Y$ or otherwise a repeat in the Markov chain $X_{t+1} = X_t$ (Foreman-Mackey et al 2012). In the limit $t \to \infty$ a stationary set of samples representative of the posterior distribution will be obtained. In practice, for the case of RM algorithms, typically at least several thousand iterations are required. MCMC algorithms usually also require a 'burn-in' step during which the sampler is calibrated to move into the correct region of the parameter space before samples are recorded. It should be mentioned that Javelin and PyROA use a different MCMC algorithm called the 'stretch move' algorithm used in the software package 'emcee' developed by Foreman-Mackey et al (2012) whilst PyceCREAM uses another variation of the MCMC algorithm.

A.0.2 RM algorithms

Javelin

The following explanation draws heavily from Zu, Y., Kochanek C. S., Peterson B. M., (2011). Javelin obtains lag estimates by modelling AGN light-curves as damped random walks (DRW) described by the Ornstein-Uhlenbeck (O-U) process

$$dX(t) = -\frac{1}{\tau_d}X(t)dt + \hat{\sigma}\sqrt{dt}\epsilon(t) + bdt, \tag{A.0.3}$$

where for our purposes $X(t)$ is the light-curve flux at time t, τ_d is the characteristic time scale, $\hat{\sigma}$ is the diffusion constant, $\epsilon(t)$ is a temporally uncorrelated unit Gaussian random variable and b is the mean light-curve flux. For further explanation on the O-U process as well as a summary on stochastic differential equations in general please see Gillespie (1996).

The O-U process has an exponential autocovariance function for the driving light-curve signal $s_d(t)$ between times t_i and t_j of the form

$$\langle s_d(t_i)s_d(t_j)\rangle = \frac{\tau_d\hat{\sigma}^2}{2}e^{-\frac{|t_i-t_j|}{\tau_d}}. \tag{A.0.4}$$

The correlation will become insignificant over timescales $|t_i - t_j| >> \tau_d$ meaning the light-curve will appear as white noise on these scales. The parameter τ_d can therefore be interpreted as the decorrelation timescale for the light-curve and $\hat{\sigma}$ can be interpreted as the variability over short timescales. The driver-lagged and lagged-lagged covariance functions are derived by assuming the lagged light-curves are linearly related to the driver by Eq. (1.10). To do this Javelin uses the simple top-hat transfer function Eq. (1.14).

To perform the fit, Javelin decomposes the light-curve data vector into three parts $\underline{y} = \underline{s} + \underline{n} + \mathbf{L}\underline{q}$ as explained above. Javelin fits the light-curves simultaneously using a Gaussian Process by treating the $\underline{s}$ and $\underline{n}$ parameters as random variables with Gaussian probability distributions. The Gaussian distributions $P(\underline{s})$ and $P(\underline{n})$ enable a likelihood to be defined

$$\begin{aligned} P(\underline{y}|\underline{s},\underline{p},\underline{q}) &\propto |SN|^{-\frac{1}{2}} \int \delta(\underline{y} - (\underline{s} + \underline{n} + \mathbf{L}\underline{q})) e^{-\frac{1}{2}(\underline{s}^T \mathbf{S}^{-1} \underline{s})} e^{-\frac{1}{2}(\underline{n}^T \mathbf{N}^{-1} \underline{n})} .\ d^{D_N}\underline{s}\ d^{D_N}\underline{n} \\ &\propto |SN|^{-\frac{1}{2}} \int e^{-\frac{1}{2}(\underline{s}^T \mathbf{S}^{-1} \underline{s})} e^{-\frac{1}{2}(\underline{y}-(\underline{s}+\underline{n}+\mathbf{L}\underline{q})^T \mathbf{N}^{-1} \underline{y}-(\underline{s}+\underline{n}+\mathbf{L}\underline{q}))} .\ d^{D_N}\underline{s}, \end{aligned} \tag{A.0.5}$$

where $\underline{p}$ are the set of parameters τ_d, $\hat{\sigma}$, A and $w \equiv t_2 - t_1$ Javelin will try to optimise for the fit. Maximising this likelihood with respect to $\underline{s}$ and $\underline{q}$ gives the following best-fit constraints for the lightcurve variability and mean

$$\begin{aligned} \hat{\underline{s}} &= \mathbf{S}\mathbf{C}^{-1}(\underline{y} - \mathbf{L}\underline{q}) \\ &= (\mathbf{N}^{-1} + \mathbf{S}^{-1})^{-1}\mathbf{N}^{-1}(\underline{y} - \mathbf{L}\hat{\underline{q}}) \\ \hat{\underline{q}} &= \mathbf{C_q}\mathbf{L}^T\mathbf{C}^{-1}\underline{y}, \end{aligned} \tag{A.0.6}$$

where $\mathbf{C} \equiv \mathbf{S} + \mathbf{N}$ and $\mathbf{C_q} \equiv (\mathbf{L}^T\mathbf{C}^{-1}\mathbf{L})^{-1}$. Here $\hat{\underline{s}}$ determines the optimal fit to the lightcurve data which has an associated uncertainty $\langle \underline{\Delta s}^2 \rangle = \underline{s} - \underline{s}^T \mathbf{C}_\perp \underline{s}$ where $\mathbf{C}_\perp \equiv \mathbf{C}^{-1} - \mathbf{C}^{-1}\mathbf{L}\mathbf{C_q}\mathbf{L}^T\mathbf{C}^{-1}$. This determines the 'error snake' present in Javelin fits. To properly define $\hat{\underline{s}}$ and $\hat{\underline{q}}$, Javelin must optimise the parameters $\underline{p}$ with respect to the data. It does this using the likelihood

$$P(\underline{y}|\underline{p}) \propto |\mathbf{S} + \mathbf{N}|^{-\frac{1}{2}} \sqrt{\mathbf{C_q}} e^{-\frac{1}{2}\underline{y}^T {\mathbf{C}_\perp}^{-1} \underline{y}}, \tag{A.0.7}$$

which is derived by marginalising over the likelihood Eq. (A.0.5) assuming uniform priors for $P(\underline{s})$ and $P(\underline{q})$.

Posterior distributions for the fitting parameters τ_d, $\hat{\sigma}$ and τ_i, w_i and A_i for each

i^{th} light-curve (contained in the covariance matrix of $\underline{\hat{s}}$) are sampled using the 'emcee' MCMC sampler using Eq. (A.0.7) as the likelihood and uniform priors for A_i and w_i. For τ_d and $\hat{\sigma}$, Gaussian priors centred on the best fit values obtained through the preliminary step are chosen with widths chosen to match the upper and lower 1σ confidence regions from the preliminary posterior distributions. Typically, the optimised parameter values are determined as the 50^{th} percentiles of the posterior distributions and the upper and lower uncertainties as the 84^{th} and 16^{th} percentiles respectively. Javelin then plots the fitted light-curves using

$$\underline{s} = \underline{\hat{s}} + \underline{u}, \tag{A.0.8}$$

where $\underline{\hat{s}}$ is the optimal light-curve fit Eq. (A.0.6) using the optimised fitting parameters and $\underline{u}$ is a random Gaussian term added to introduce the appearance of stochasticity to the light-curve. Javelin is able to interpolate between measured data points by appending the data vector $\underline{y}$ with a set of fake data points $\underline{y_f}$ over a grid of unmeasured times.

Javelin has recently been updated with a 'disc Model' mode designed specifically for accretion disc reverberation mapping. In contrast to the original 'Rmap Model' which samples the lag directly as a free parameter, the 'disc Model' samples the lag τ between λ and λ_α emitting regions of the disc indirectly by instead sampling the parameters α and β which are constrained by the classic thin disc equation

$$\tau = \frac{\alpha}{c}\left[\left(\frac{\lambda}{\lambda_\alpha}\right)^{\beta} - 1\right]. \tag{A.0.9}$$

Eq. (A.0.9) is derived from the thin disc relationship $R \propto \lambda^{\beta}$ of Shakura N.I., Sunyaev R.A., (1973) (as outlined in section 1.1.2) and is equivalent to imposing a thin disc prior on the lag. As such, β controls the power law scaling of disc radius with wavelength and α sets the length scale of the disc and corresponds to the radius of the λ_α emitting region for the standard thin disc model (with $\beta = \frac{4}{3}$). For more detail see Mudd et al (2018).

A brief mention should be made to the RM algorithm MICA developed by Li et al (2016) for BLR RM. This takes a non-parametric approach to fitting the light-curve data by using a Gaussian process with a damped random walk kernel following a similar method as used in Javelin. The key distinction is in MICA's treatment of the transfer function as a sum of displaced Gaussian functions allowing arbitrary, complex transfer function shapes to be formed. This is expected to more realistically model the effects of the complex

BLR geometry on the response function than the simple top-hat transfer function used in Javelin. As such MICA could be used as a more sophisticated alternative to Javelin.

PyROA

The following explanation draws heavily from Donnan, F R. et al (2021). PyROA fits each light-curve using a running optimal average (ROA) $X(t)$ which is defined as an optimal inverse-variance weighted average of all the N data points D_i with errorbars σ_i measured at times t_i with an added Gaussian window function. At time t the ROA is defined as

$$X(t) = \frac{\sum_{i=1}^{N} D_i \frac{1}{\sigma_i^2} e^{-\frac{1}{2}\left(\frac{t-t_i}{\Delta}\right)^2}}{\sum_{i=1}^{N} \frac{1}{\sigma_i^2} e^{-\frac{1}{2}\left(\frac{t-t_i}{\Delta}\right)^2}}. \tag{A.0.10}$$

Here the Δ parameter in the weights corresponds to the width of the Gaussian window function and therefore controls how quickly the influence data points have over the fit diminishes with time separation as outlined above. To find a compromise between smoothness and closeness of fit the algorithm minimises the Bayesian Information Criterion (BIC) statistic defined as

$$BIC = -2lnP(D|M) + PlnN. \tag{A.0.11}$$

Here $P(D|M)$ is the likelihood for model M. By assuming Gaussian measurement errors on the data, PyROA defines the likelihood as

$$P(D|M) = \prod_{i=1}^{N} \frac{\sigma_i}{\sqrt{\sigma_i^2 + s_i^2}} e^{-\frac{1}{2}\left(\frac{D_i - f_i}{\sqrt{\sigma_i^2 + s_i^2}}\right)} \tag{A.0.12}$$

where f_i and s_i are the model value and the added error corresponding to each data point D_i in the light-curve.

The parameter P in the BIC Eq. (A.0.11) is defined as the total number of parameters in the fit $P \equiv 4 + P_x$. P_x corresponds to the effective number of parameters of the fit (controlled by Δ) with the four remaining parameters in P being the rms flux A_i, mean flux B_i, lag τ_i and added error s_i for each i^{th} light-curve. The effective number of parameters P_x is defined as the sensitivity of the model $X(t_i)$ to changes in each data point D_i and is

quantified over all N data points as

$$P_x(\Delta) = \sum_{i=1}^{N} \frac{\partial X(t_i)}{\partial D_i} = \sum_{i=1}^{N} \frac{\left(\frac{1}{\sigma_i}\right)^2}{\sum_k \frac{1}{\sigma_k^2} e^{-\frac{1}{2}\left(\frac{t_i - t_k}{\Delta}\right)^2}}. \tag{A.0.13}$$

To perform the fit, PyROA samples posterior distributions for the fitting parameters A_i, B_i, τ_i and s_i for each i^{th} light-curve using the 'emcee' MCMC sampler (Foreman-Mackey et al 2012) with the BIC Eq. (A.0.11) as the likelihood and uniform priors for the parameters. For each iteration in the MCMC algorithm, each i^{th} light-curve data set is shifted back in time by τ_i (with $\tau_i \equiv 0$ for the driving light-curve) and normalised such that each data point $D_i \to \frac{D_i - B_i}{A_i}$. This has the effect of stacking the light-curves on top of each other. After adding the extra error parameter s_i in quadrature to the error bars of each light-curve $\sigma_i \to \sqrt{\sigma_i^2 + s_i^2}$, the stacked light-curves are treated as a single merged light-curve and the ROA $X(t)$ is determined using a grid of 1000 equally spaced points ranging from the initial to the final times of the combined data set. After normalising the ROA $X(t) \to \frac{X(t) - \bar{X}(t)}{\sigma_x}$ (where $\bar{X}(t)$ and σ_x are the mean and standard deviation respectively for the ROA) the model fit is then determined for each individual light-curve as

$$f_i(t) = A_i X(t - \tau_i) + B_i. \tag{A.0.14}$$

Typically, the optimised parameter values are determined as the 50^{th} percentiles of the posterior distributions and the upper and lower uncertainties as the 84^{th} and 16^{th} percentiles respectively.

PyceCREAM

The following explanation draws heavily from Starkey et al (2016). PyceCREAM models the lagged light-curve flux by adapting the linear response function Eq. (1.10) into a discretised form

$$F_\nu(\lambda, t) = \bar{F}_\nu(\lambda) + \Delta F_\nu(\lambda) \sum_{i=0}^{\tau_{max}} \psi(\tau_i|\lambda) \Delta F_x(t - \tau_i) \Delta\tau \tag{A.0.15}$$

where the variable component of the driving light-curve $\Delta F_x(t)$ is convolved with the normalised, dimensionless transfer function $\psi(\tau|\lambda)$ as expected. Here $\Delta F_\nu(\lambda)$ is the variable component of the spectrum and is used to scale the model variations to fit the data and $\bar{F_\nu}(\lambda)$ is the background flux.

The accretion disc transfer function $\psi(\tau)$ is derived (following the approach of Starkey, D., et al, 2017) by differentiating the reprocessed accretion disc flux $f_{\nu,L}$ in Eq. (1.10) by the driving lamp-post flux $f_{\nu,D}(t-\tau)$ such that

$$\begin{aligned}
\frac{\partial f_{\nu,L}(\lambda,t)}{\partial f_{\nu,D}(t-\tau)} &= \int_0^\infty \psi_\nu(\tau'|\lambda)\delta(\tau-\tau').d\tau' = \psi_\nu(\tau|\lambda) \\
\implies \psi_\nu(\tau|\lambda) &= \int_\Omega \frac{\partial B_\nu(T,\lambda)}{\partial f_{\nu,D}(t-\tau)}\delta(\tau-\tau'(r,\theta,i)).d\Omega \\
&= \int_\Omega \frac{\partial B_\nu(T,\lambda)}{\partial T}\frac{\partial T}{\partial L_x}\frac{\partial L_x}{\partial f_{\nu,D}}\delta(\tau-\frac{r}{c}(1+\sin i\cos\phi)).d\Omega.
\end{aligned} \tag{A.0.16}$$

Here the second equation originates from the Planckian description of accretion disc flux Eq. (1.6) and L_x is the driving luminosity of the lamp-post. Due to the normalised definition of $\psi(\tau)$ in PyceCREAM, the $\frac{\partial L_x}{\partial f_{\nu,D}}$ term just introduces a factor of 4π into the transfer function that has no effect on the result. As such, Eq. (A.0.16) is equivalent to the accretion disc transfer function Eq. (1.12). PyceCREAM evaluates Eq. (A.0.16) in a discretised form over a grid of radii r_{ir} and azimuthal angles θ_{iA}

$$\begin{aligned}
\psi_\nu(\tau|\lambda) = \sum_{ir}\sum_{iA} &\frac{\partial B_\nu(T(r_{ir},\theta_{iA}),\lambda)}{\partial T} \\
&\times \frac{\partial T}{\partial L_x}\frac{\partial L_x}{\partial F_x} f_c(r_{ir})\delta(\tau-\tau'(r_{ir},\theta_{iA},i))\Delta\Omega
\end{aligned} \tag{A.0.17}$$

where $\Delta\Omega = \frac{r_{ir}\Delta r_{ir}\Delta\theta}{D^2}$ and f_c is the fraction of the disc covered by black-body emitting material (see Starkey, D., et al, 2017).

B_ν and T are defined by Plancks function Eq. (1.6) and a thin disc temperature-radius relation of the form $T = T_0\left(\frac{r_0}{r}\right)^{\frac{1}{\beta}}$ where T_0 takes the form Eq. (1.8) including the lamp-post term. This means that $\psi_\nu(\tau)$ is a function of $M\dot{m}$ and inclination i.

PyceCREAM attempts to infer the shape of the driving light-curve (using the lamp-post model) from the data by expressing the driving light-curve as a Fourier time series with N_k terms

$$\Delta F_x = \sum_{k=1}^{N_k} C_k cos(\omega_k t) + S_k sin(\omega_k t) \tag{A.0.18}$$

where C_k and S_k are Fourier amplitude coefficients and $\omega_k = k\Delta\omega$ is the k^{th} Fourier frequency. The maximum and minimum Fourier frequencies $\omega_{low} \equiv \Delta\omega$ and $\omega_{high} \equiv N_k\Delta\omega$ are set by default as

$$\begin{aligned} \omega_{high} &= \frac{2\pi}{\bar{\Delta}t} \\ \omega_{low} &= \frac{1}{2}\frac{2\pi}{T_{rec}} \end{aligned} \tag{A.0.19}$$

where $\bar{\Delta}t$ is the mean time separation between adjacent points and T_{rec} is the recurrence time for the Fourier series. T_{rec} should be set to be longer than the time-span of the data plus the width of the transfer function to ensure that the periodicity of the Fourier series does not appear in the light-curve fits which are expected to be aperiodic.

During the fitting procedure, PyceCREAM uses a bayesian statistic called the Badness of fit (BOF) which the MCMC sampler attempts to minimise. BOF is defined as

$$\begin{aligned} BOF &= -2\ln P(M|D) \\ &= \chi^2 + \sum_{i=1}^{N} \ln(\sigma_i^2) - 2\ln P(M) + \text{constant} \end{aligned} \tag{A.0.20}$$

where $P(M|D)$ is the bayesian posterior distribution with N_{par} parameters $\underline{M}$ and N data points $\underline{D}$ with corresponding error-bars σ_i. The second expression in Eq. (A.0.20) comes from Bayes equation assuming Gaussian errors on the data points where $\chi^2 \equiv \sum_{i=1}^{N}\left(\frac{D_i - f_i}{\sigma_i}\right)$ is the standard chi-squared statistic and f_i are the model values at measured times.

The $\ln P(M)$ term in Eq. (A.0.20) corresponds to the prior distributions for the fitting parameters. Uniform priors are chosen for the cos$i$, log$M\dot{m}$, logΔF_ν and log$\bar{F}_\nu(\lambda)$ parameters. However when uniform priors are chosen for the S_k and C_k parameters, PyceCREAM has a tendency to overfit the data by using too many high frequency Fourier terms to form the driving light-curve. This is because for uniform priors $BOF \propto \chi^2$ meaning the algorithms attempts to minimise the BOF becomes equivalent to minimising χ^2. As a result, the algorithm is encouraged to fit the data as closely as possible which it does by forming long Fourier chains to generate an overly flexible driving light-curve. To mitigate this, PyceCREAM instead uses Gaussian priors for S_k and C_k defined by

$$P(M) = \prod_{k=1}^{N_k} \frac{e^{-\frac{1}{2}\frac{C_k^2 + S_k^2}{\sigma_k^2}}}{2\pi\sigma_k^2}. \tag{A.0.21}$$

Here the mean of the Gaussian prior is defined as $\langle C_k \rangle = \langle S_k \rangle = 0$ and the variances as $\langle S_k^2 \rangle = \langle C_k^2 \rangle = \sigma_k^2$ where σ_k^2 is defined as

$$\sigma_k^2 \equiv \frac{P_0 \Delta\omega}{2} \left(\frac{\omega_0}{\omega_k} \right)^2 . \tag{A.0.22}$$

This is effectively a 'random walk prior' for S_k and C_k such that

$$\langle S_k^2 \rangle + \langle C_k^2 \rangle = P_0 \Delta\omega \left(\frac{\omega_0}{\omega_k} \right)^2 \tag{A.0.23}$$

where $P_0 \Delta\omega$ is the amplitude of the power spectrum of the random walk at ω_0 (see Uttley et al, 2002). It is clear that Eq. (A.0.23) would help to prevent higher frequency Fourier amplitudes from being over represented as $\langle S_k^2 \rangle + \langle C_k^2 \rangle \propto \frac{1}{\omega_k^2}$. Interestingly, a power spectrum of the form Eq. (A.0.23) is consistent with power spectra thought to drive observed X-ray variability (see Uttley et al, 2002; McHardy et al, 2006) which means this prior is effectively a preference that the driving lightcurve is in the form of X-rays. There is some observational evidence to support this idea (e.g. McHardy et al, 2014).

APPENDIX B

Additional and Auxiliary Results

B.1 Comprehensive comparison of RM algorithms

B.1.1 Javelin

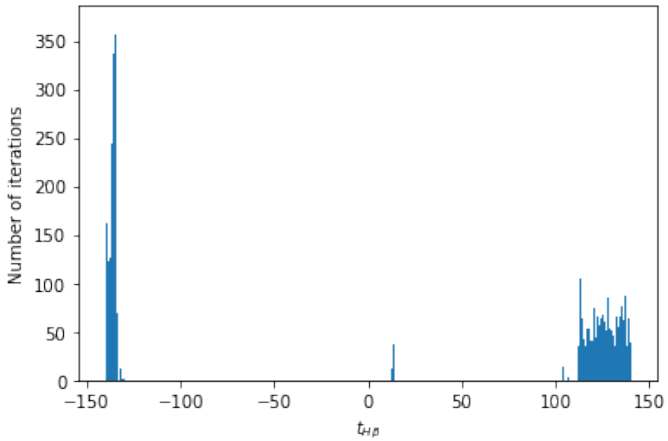

Figure B.1: Posterior lag distributions obtained by Javelin for the 5100$\mathring{A}$ continuum and Hβ light-curves for NGC 4151 from De Rosa et al (2018). Here the MCMC sampler is allowed to explore the full parameter space.

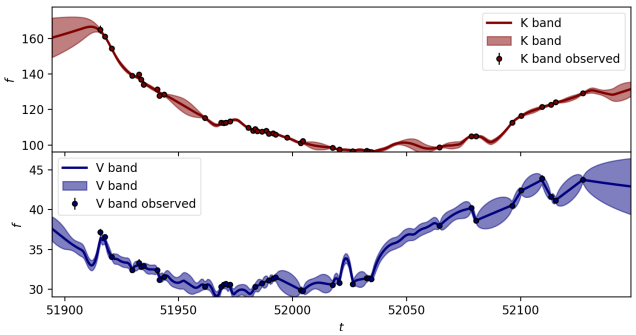

Figure B.2: Fit obtained by Javelin for the V and K band light-curves for NGC 4151 from Koshida et al (2014). Flux units are in mJ

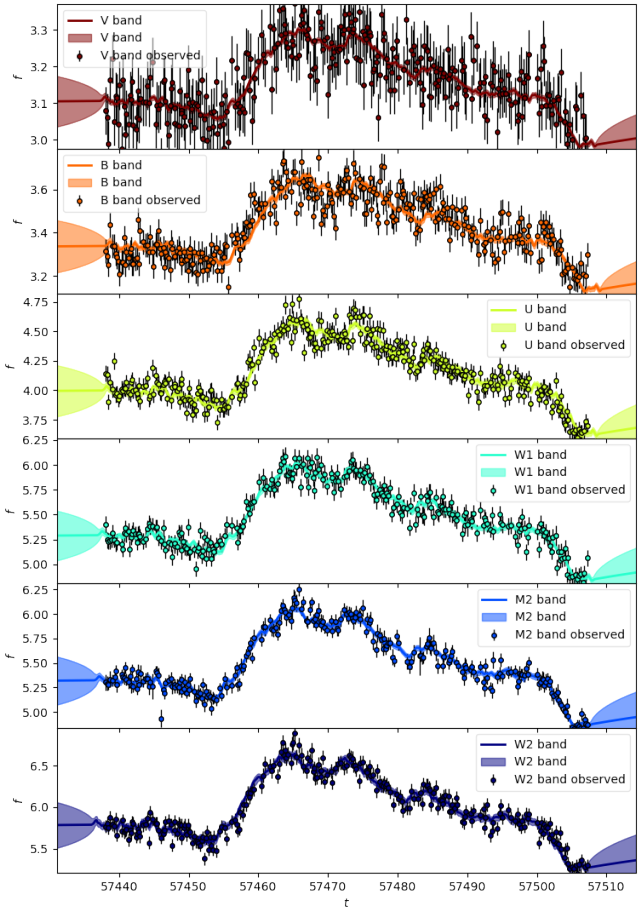

Figure B.3: Fit obtained by Javelin for the Edelson et al (2019) data for NGC 4151. Flux units are in mJ

B.1.2 PyROA

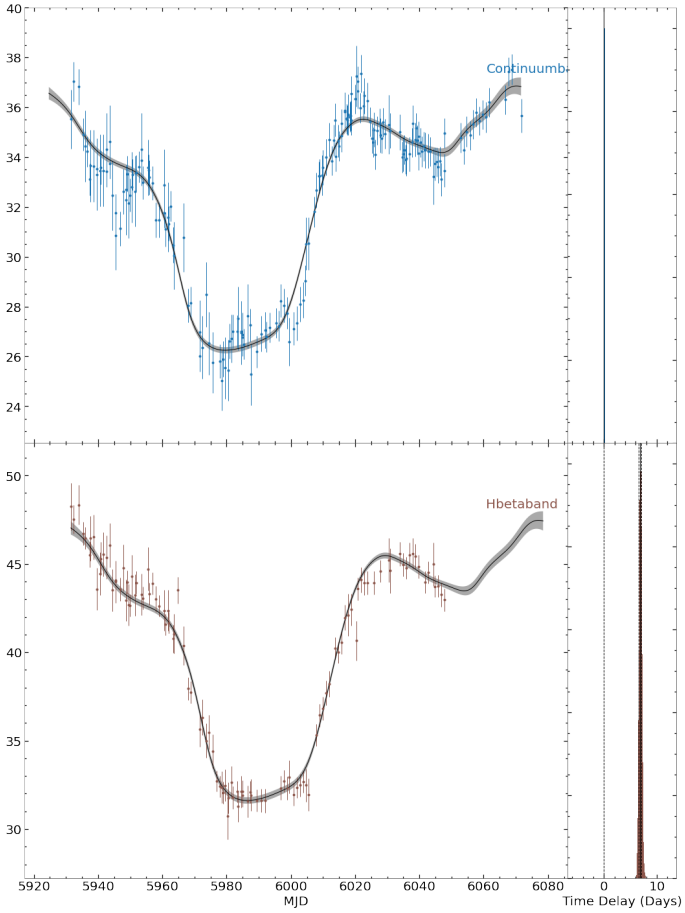

Figure B.4: Fit obtained by PyROA for the 5100$\mathring{A}$ continuum and Hβ bands from De Rosa et al (2018) with the Dirac delta transfer function for NGC 4151. Flux units are in mJ

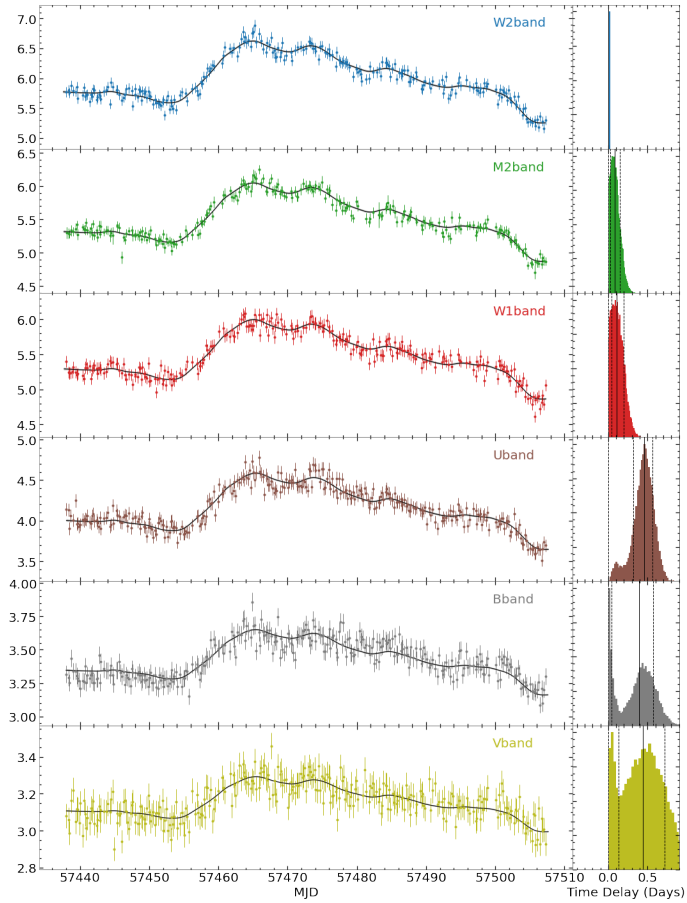

Figure B.5: Fit obtained by PyROA for the Edelson et al (2019) data-set using the Dirac delta transfer function for NGC 4151. Flux units are in mJ

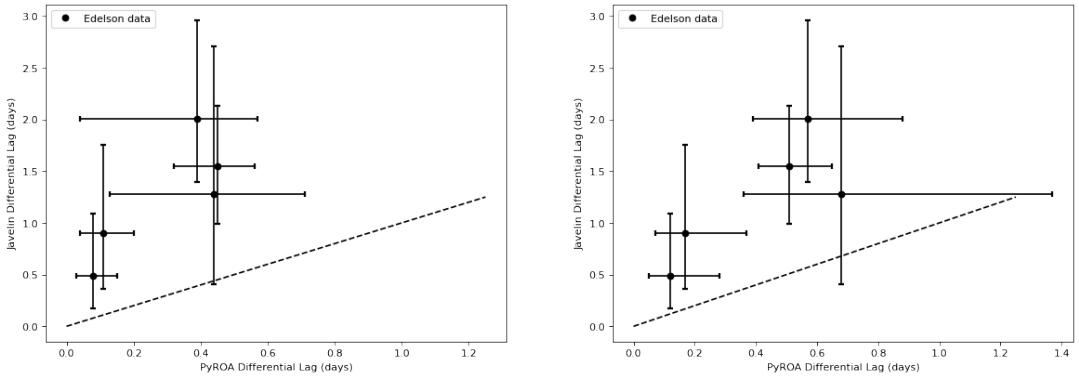

(a) Dirac delta transfer function.

(b) Log-Gaussian transfer function.

Figure B.6: Differential Lag results for NGC 4151 using Javelin and PyROA taken from Koshida et al (2014), De Rosa et al (2018) and Edelson et al (2019). Here the dashed line $y = x$ corresponds to total agreement between Javelin and PyROA.

B.1.3 PyceCREAM

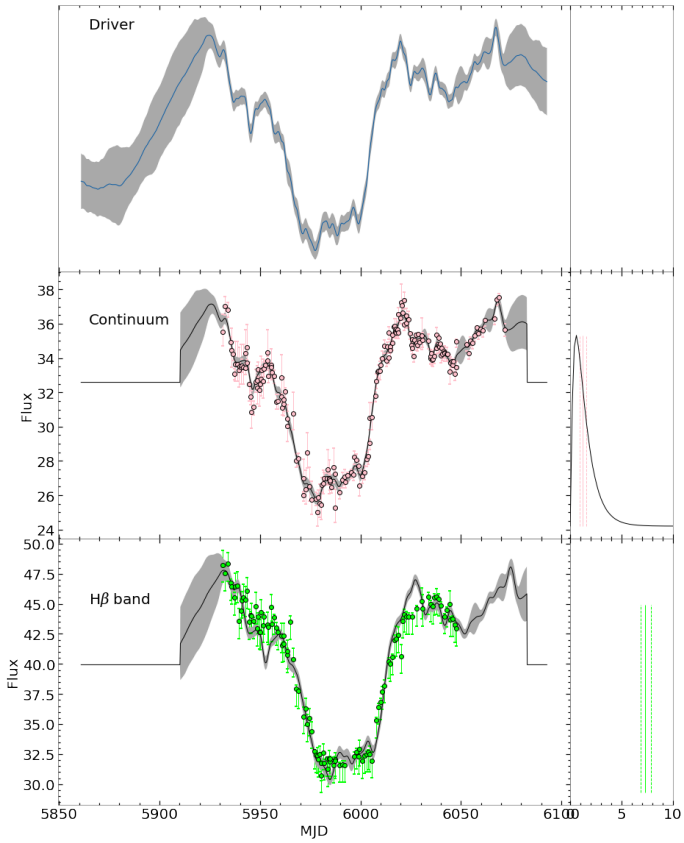

Figure B.7: Fit obtained by PyceCREAM for the De Rosa et al (2018) data-set using the accretion disc transfer function for the 5100$\mathring{A}$ continuum and a top-hat transfer function for the Hβ band for NGC 4151. Flux units are in mJ

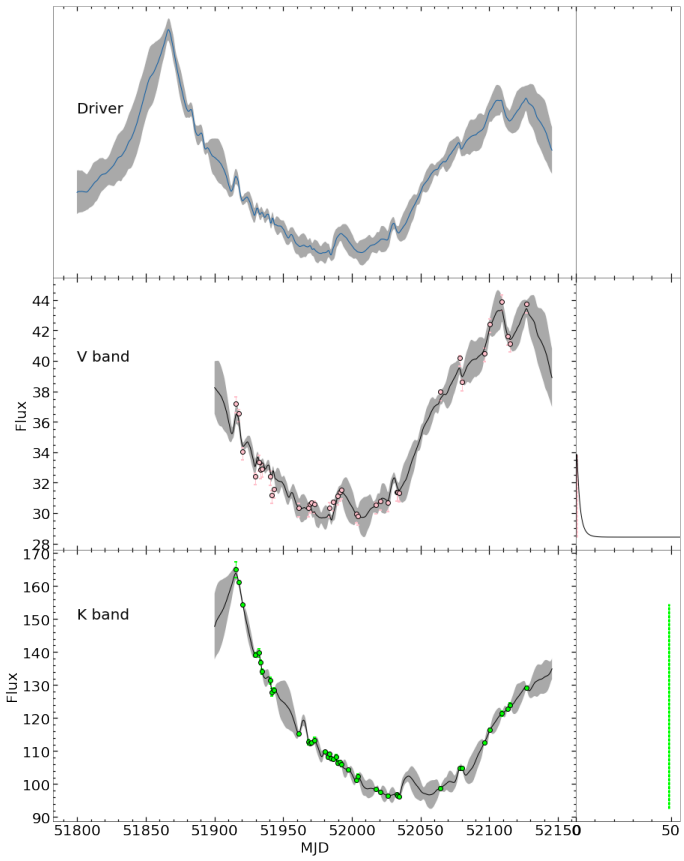

Figure B.8: Fit obtained by PyceCREAM for the Koshida et al (2014) data-set using the accretion disc transfer function for the V band and a top-hat transfer function for the K band for NGC 4151. Flux units are in mJ

B.2 Reverberation Mapping of 3C 273

B.2.1 Contamination Estimates

Figure B.9 shows a more complete version of Figure 3.3 spanning the UV to the near infrared optical with a wavelength range $3000\mathring{A} - 21000\mathring{A}$. Also shown is the expected thin accretion disc relation $f_\lambda \propto \lambda^{-\frac{7}{3}}$ fitted to the spectrum using scipy's 'curve-fit' module. By

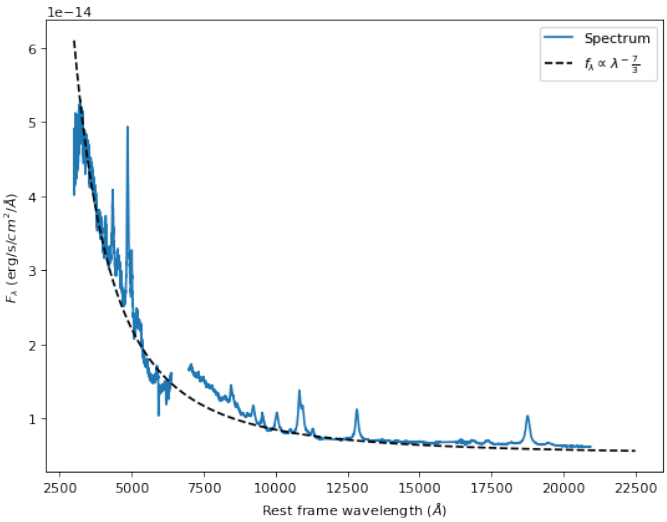

Figure B.9: Spectrum of 3C 273 spanning the UV to the near infrared taken from Landt et al (2011). The thin disc power law relation $f_\lambda \propto \lambda^{-\frac{7}{3}}$ is fit to the spectrum.

using the expected thin disc fit in Figure B.9 as an estimate of the accretion disc specific flux f_λ at wavelength λ, estimates for the percentage flux contamination in each of the measured photometric bands can be obtained. This is done by determining the ratio of the area under the spectrum in Figure B.9 to the area under the fitted thin disc curve in each of the LCO filters. This could not be done for the U band due to the instrumentation effect mentioned above. Similarly, accurate contamination measurements for the I band in 3C 273 could not be obtained due to the gap in the spectrum at this wavelength. The estimated contamination levels are shown in Table 3.3 and 3.4

B.2.2 Design of the Simulation

Our simulation of the accretion disc spectrum in 3C 273 assumes a Schwarzschild SMBH meaning the inner boundary of the accretion disc was set at $r_{ISCO} = 3r_g$ where $r_g \equiv \frac{2GM}{c^2}$ is the Schwarzschild radius. The outer edge was set at an arbitrarily large radius of 10,000 r_g with the accretion disc modelled as a series of radial slices increasing in increments of $1r_g$. To perform the simulation, the temperature of each disc increment was determined using

the thin disc temperature-radius relation Eq. (1.4) with SMBH mass $M = 8.9 \times 10^8 M_\odot$ and bolometric luminosity $L_{bol} = 10^{46.66}\text{ergs}^{-1}$ which was used to determine $\dot{m}$ using the relation Eq. (1.1) with a standard efficiency $\eta = 0.1$ (all values are taken from Landt et al (2011)). This was done both with and without the boundary condition term in Eq. (1.4) thereby generating the two simulations shown in Figure 3.3. The predominant wavelength emitted by each disc increment was then determined from the derived temperature T using Wien's law Eq. (3.1) with the standard value $X = 4.96$. To determine the expected flux f_{ν_0} emitted at λ_0, Plancks function relation Eq. (1.7) was used with the assumption of a face-on disc with respect to observers.

B.2.3 X considerations and derivation

The use of Wiens law Eq. (3.1) (with $X = 1$) in the temperature radius relation Eq. (1.4) assumes that the flux emitted at wavelength λ from the disc is emitted entirely from a particular annulus at temperature T. As such it ignores the contribution to λ from the rest of the disc which is expected to emit as a black-body continuum. The dimensionless constant X is added to Eq. (3.1) to act as a scale factor to account for the contribution to λ from the rest of the disc. A value of $X = 4.96$ is used for the standard Wien's displacement law. However, following the approach of Mudd et al (2018), a corrective X value can be derived for a particular wavelength λ_0 emitted by a particular AGN accretion disc by

$$X = \frac{\langle R_{\lambda_0} \rangle}{R_{\lambda_0}}. \tag{B.2.1}$$

Here R_{λ_0} is the disc radius emitting predominantly at λ_0 using Wiens law with $X = 1$. $\langle R_{\lambda_0} \rangle$ is the flux weighted mean radius and can be interpreted as the average radial location of the part of the disc emitting predominantly at λ_0 taking account of the contributions to λ_0 from the entire disc's continuum black-body emission. As such, $\langle R_{\lambda_0} \rangle$ is defined as

$$\langle R_{\lambda_0} \rangle = \frac{\int_{R_{inner}}^{R_{outer}} B_\nu R^2 . dR}{\int_{R_{inner}}^{R_{outer}} B_\nu R . dR}. \tag{B.2.2}$$

X can therefore be interpreted as a scale factor converting the simplistic description of accretion disc emission tied to a particular annulus to the more physically correct description involving the entire disc emitting as a black-body.

To test the effectiveness of Mudd et al (2018) treatment of X, we derived lag predictions for 3C 273 using both the standard approach $X = 4.96$ and the new approach outline above which are shown in column 3 of Table 3.6. To derive the X values for each of the LCO filters used to monitor 3C 273 in our campaign, $\langle R_{\lambda_0} \rangle$ was calculated using Eq. (B.2.2) and substituting the temperature-radius relation Eq. (1.4) into Plancks function Eq. (1.6) using the M, $\dot{m}$ and r_{ISCO} values used to obtain the lag predictions in Table 3.6. Here $R_{inner} \equiv 3r_g$ and $R_{outer} \equiv 10000r_g$ as done in the simulation. R_{λ_0} was determined by substituting Wiens law Eq. (3.1) with $X = 1$ into the temperature radius relation Eq. (1.4). The estimated X values for each of the observed filters in 3C 273 is shown in Table B.1. As can be seen they are not too dissimilar from the standard $X = 4.96$ and decrease in magnitude with increasing wavelength. This makes intuitive sense as the longer wavelength filters will have smaller contributions from the brightest, inner regions of the accretion disc meaning the ratio between assuming a single emitting annulus R_{λ_0} and the full flux weighted mean radius $\langle R_{\lambda_0} \rangle$ can be expected to be smaller.

Filter	X_{new}
U	4.99
B	4.52
G	4.39
V	4.22
R	4.11
I	3.96
Z	3.88

Table B.1: A set of proportionality factors X for Wiens law (4.1) derived following the approach of Mudd et al (2018) for each of the LCO filters used to observe 3C 273.

B.2.4 Investigating the trend

The trends in our 3C 273 light-curve data appear to have a quasi-periodic character and were reasonably well fit by Sine functions with 'lmfit' (Newvillem, M et al 2016) assuming linear interpolation across the gaps. An example of the fit obtained for the B band trend is shown in Figure B.10(a). To test the apparently identical trend present in our U band light-curve, the U band data-set was subtracted from the remaining light-curves in Figure 4.1(a). This was done by shifting each light-curve back by the expected differential lags shown in Table 3.6 and then normalising the flux of each data-set by subtracting its mean $\bar{f}$ and scaling it by its standard deviation σ such that $f_{new} = \frac{f-\bar{f}}{\sigma}$. Each optical light-curve

was then cut-down to select for data points most similar in time to those in the U band light-curve to keep the data sets dimensionally consistent. The subtracted light-curves obtained have the appearance of white noise with only the possibility of weak residual trends apparent. An example of the residual B band light-curve after subtraction of the U band is shown in Figure B.10(b). This indicates that the trend in the U band is the same as in the other light-curves which further refutes the possibility that the trend originates from the jet as the U band light-curve is expected to have no significant jet contribution. However the usefulness of the U band subtraction is limited due to the large scatter in this data-set.

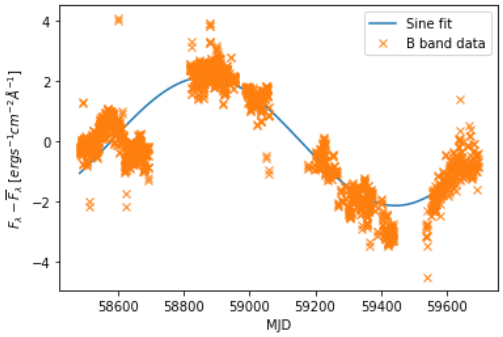

(a) Sine fit to the B band light-curve allowing the amplitude and period of the quasi-periodic oscillation to be estimated.

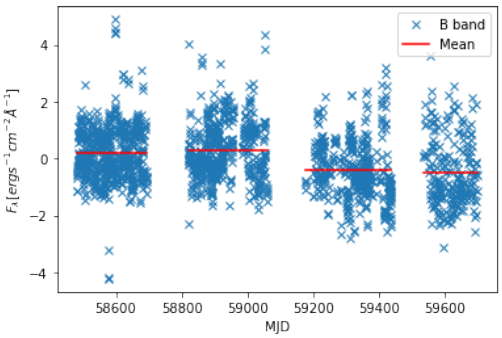

(b) The residual light-curve left after subtraction of the U band from the B band.

Figure B.10: Investigations of the long-term trend in 3C273 with the B filter used as an example.

B.2.5 Intra-day Jet variability

Another possible explanation for the bias found in our default PyROA fits could be a result of intra-day variability detected in optical measurements of 3C 273 in the vri bands carried out by Xiong et al (2017) which they attribute to the effects of relativistic shocks in the jet. Xiong et al (2017) could not detect any significant time lag between their measured v and i intra-day variable light-curves. These results could explain why the short timescale variability fits in Figure B.15(b) returned zero biased lags if the apparent intra-day variability in our light-curves can be attributed to the jet. In addition, our light-curve data for 3C 273 is remarkably well sampled with $\sim$ 83% of all observations having cadences on the intra-day scale and $\sim$ 75% having cadences on scales less than the most significant jet intra-day timescale (according to Xiong et al (2017)) of 154 minutes. Therefore if there is intra-day variability originating from the jet in 3C 273, our data-set

would likely detect it. That said, there are significant overlaps in the error-bars of our flux measurements on the intra-day scale. When selecting for 'meaningful' variability, defined as the nearest pairs of data-points with a difference in flux greater than the sum of their error-bars, we found only $\sim 10-15\%$ of our data across all six light-curves displayed intra-day variability that we could be confident existed and only $\sim 6\%$ displayed variability on the significant 154 minutes timescale. On top of this, the intra-day variability detected by Xiong et al (2017) was not very significant with most of it occurring on amplitudes $\leq 10\%$ and only being detected on 7 out of the entire 105 nights they observed (although this may be a result of their relatively short observing periods).

B.2.6 BLR lag estimates

The 'Failed Radiatively Accelerated Dust-driven Outflow' (FRADO) model of the formation of the BLR explained by Czerny et al (2015) models the formation of the BLR as originating from dusty outflows from the accretion disc. Under this model, the inner edge of the BLR can be expected to form at the same radius as the part of the accretion disc with an effective temperature of $\sim$ 1000K at which point dust begins to form. Using our PyROA RM results, the predominant wavelength emitted by the 1000K region of the accretion disc in 3C 273 can be estimated using Wiens law Eq. (3.1) with a value $X = 7.4$ to make it consistent with the up-scaled accretion disc suggested by our PyROA lag estimates. This can be expected to emit predominantly at $\sim 19500\mathring{A}$ rest wavelength which places it between the H and K bands as can reasonably be expected. By assuming the 1000K region of the accretion disc exists at the same radius as the inner edge of the BLR and that the K emitting region exists at the outer edge of the BLR where the torus begins to form (as per the FRADO schematic shown in Figure 1.1) a mean lag for the BLR in 3C 273 can be estimated by interpolating the best-fit power law in Figure 3.7(b) at these wavelengths and averaging over the expected lags. This was converted to absolute lags for our PyROA RM results by estimating the B band lag at 21.6 days with $X = 7.4$. Similar absolute lag estimates were obtained using the best-fit combined PyROA and Javelin RM results with a value $X = 8$ to scale the accretion disc appropriately. The lag values are given in Section 3.3.2.

B.2.7 Assorted Graphs

Filter	Signal amplitude relative to noise amplitude
B	2.00
G	3.46
V	3.47
R	3.34
I	1.59
Z	1.60

Table B.2: Estimates for the amplitude of the model fit by PyROA in Figure 3.7 to the magnitude of the residuals.

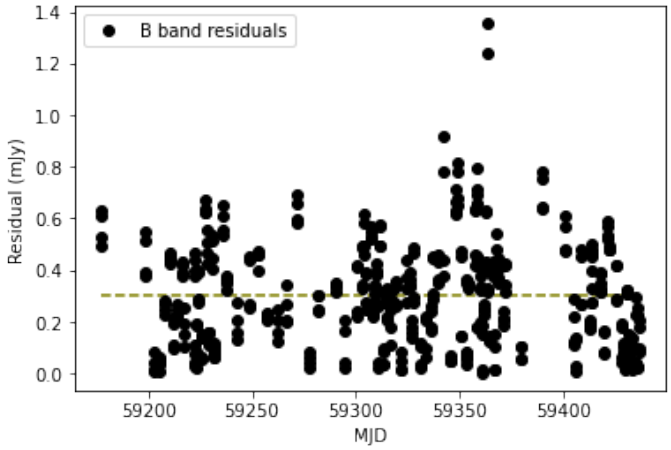

Figure B.11: Distribution of the residuals in the B band light-curve with respect to the model fit by PyROA in Figure 3.7.

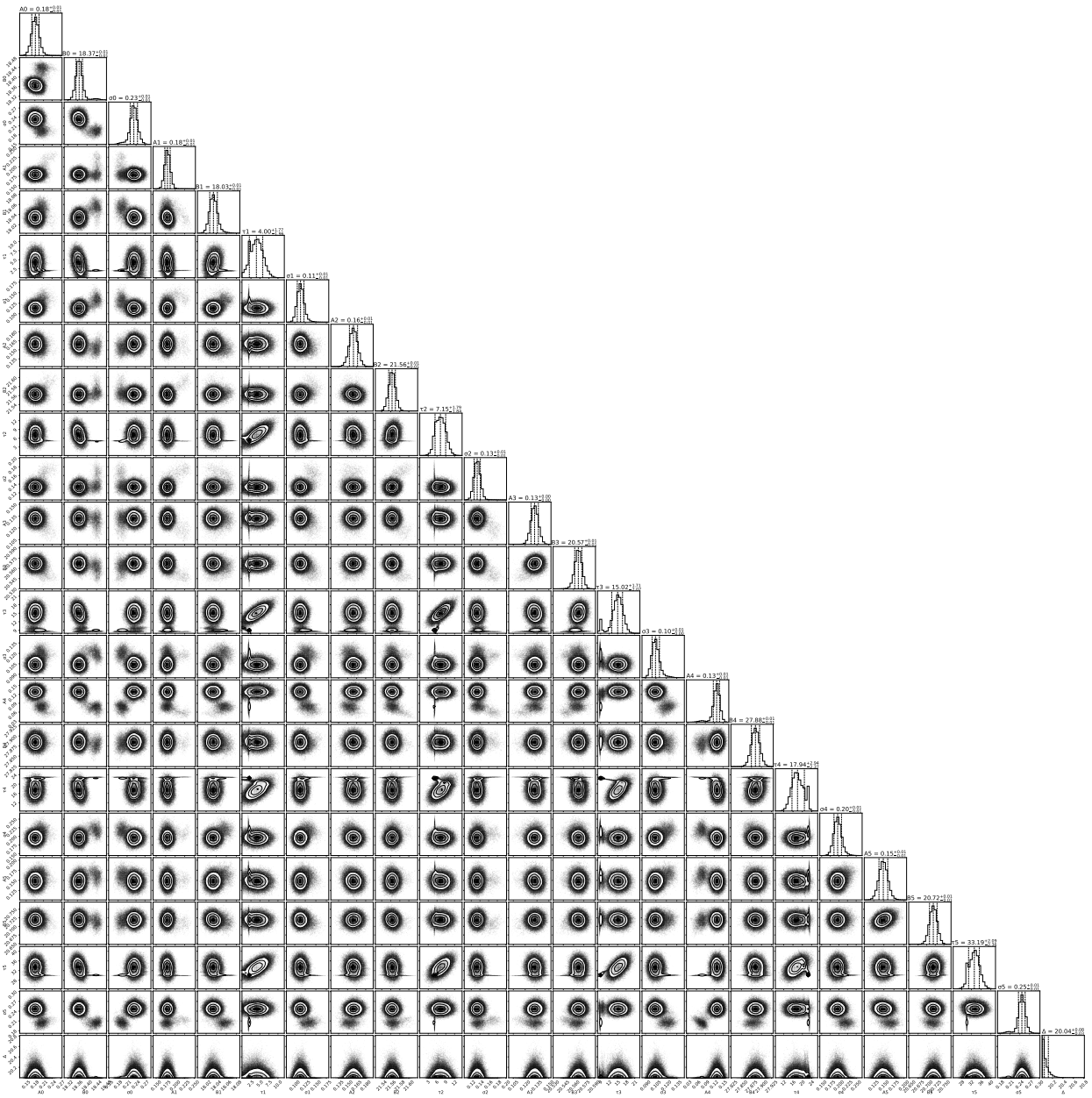

Figure B.12: PyROA corner plots to the 3C 273 fits in Figure 3.7.

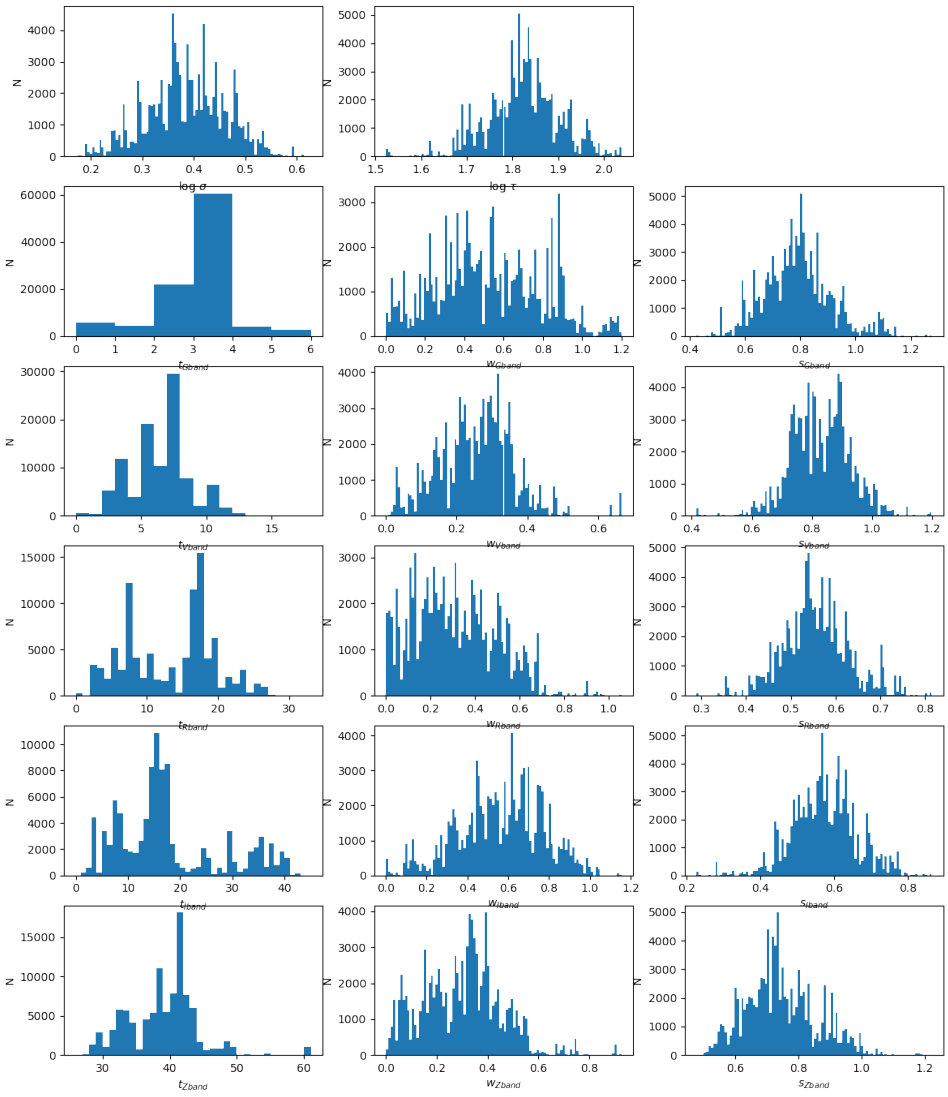

Figure B.13: Posterior distributions obtained by Javelin for the fit in Figure 3.9. The distributions are for the decorrelation timescale τ_d and short timescale variability amplitude $\hat{\sigma}$ and then the lag τ, tophat width w and scale s for each light-curve.

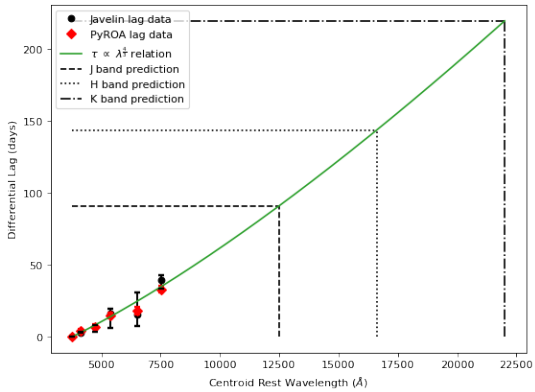

(a) Extrapolation of the thin disc $\beta = \frac{4}{3}$ power law.

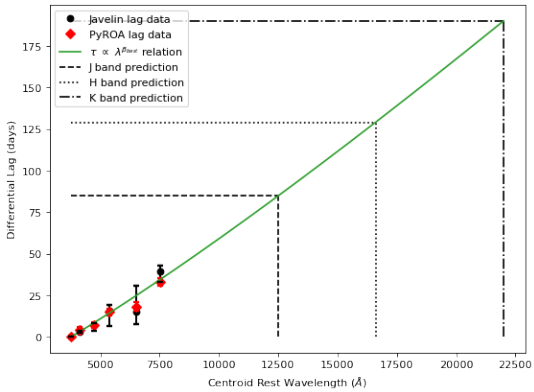

(b) Extrapolation of the best-fit $\beta \sim 1.16$ power law.

Figure B.14: Extrapolations of the thin disc and best-fit power laws fit to the combined PyROA and Javelin RM results into the near-infrared JHK regime. This allowed lag predictions in Table 3.10 to be made.

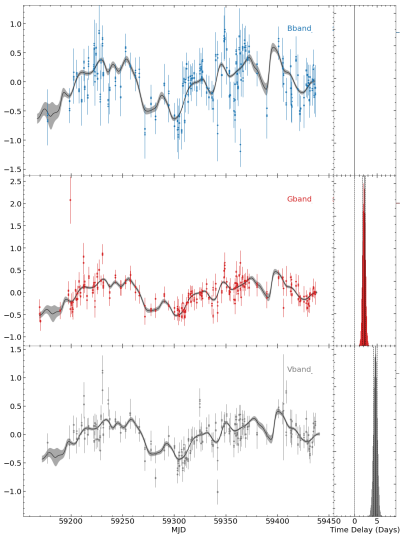

(a) PyROA fits for bgv filters in 3C 273. The MCMC chains converged to the expected lags.

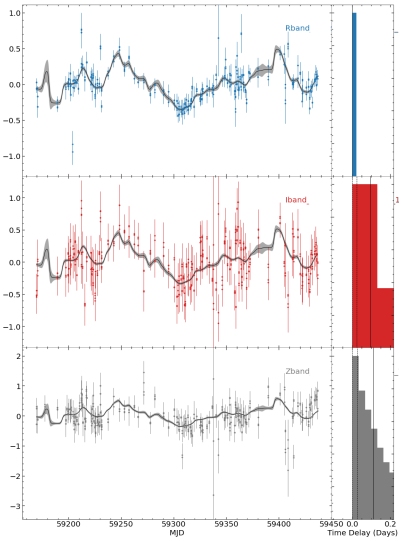

(b) PyROA fits for riz filters in 3C 273. The MCMC chains converged towards zero indicating a stronger bias for longer wavelengths.

Figure B.15: Zero bias dependence on wavelength tests. For each filter the Markov chain was initialised half-way between zero and its expected lag. Blurring was controlled across the 6 filters.

B.3 Reverberation Mapping of 1H 2106-099

B.3.1 Erroneous Javelin Fits

The differential lag estimates for 1H 2106-099 obtained for all ugriz filters by Javelin is shown in Table B.3. The fits and distributions we obtained are shown in Figures B.20 and B.21. Figure B.16 shows the differential lags and residuals obtained by Javelin with respect

Filter	Lag estimate (days)	Lag Prediction (days)	
		X=4.96	X_{new}
U	0	0	0
G	$0.74^{+0.13}_{-0.09}$	0.50	0.31
R	$2.41^{+0.15}_{-0.31}$	1.13	0.70
I	$2.54^{+0.04}_{-0.07}$	1.75	1.08
Z	$2.59^{+0.12}_{-0.12}$	2.32	1.43

Table B.3: Differential lag estimates for the regions of the accretion disc in 1H 2106-099 emitting predominantly in each of the LCO filters. Two sets of predictions are obtained using the standard $X = 4.96$ and a new set of X values derived following the approach of Mudd et al (2018).

to the U band plotted against the rest frame centroid ugriz wavelengths. As can be seen the same discontinuity between the ug and riz filters is obtained as found with PyROA. However, the two power laws show the opposite behaviour as found with the PyROA analysis with the ug appearing steeper and the riz shallower. Thin disc power laws have been well fitted to the ug and riz filters with scipy 'curve-fit'. However, when a power law with an unfixed exponent is fit to the riz filters following the logarithmic approach done for the PyROA results, an unrealistically small exponent $\beta = 0.19 \pm 0.06$ is preferred which is completely inconsistent with all the preceding analysis. We do not have much confidence in the lag estimates in Table B.3 due to the erroneous U band model fit seen in Figure B.20 which appears to lag behind the U band data. This would have a significant effect on the small lags we are attempting to measure. In particular, the erroneous U band fit would result in anomalously large differential lag estimates for the g band which the algorithm has likely compensated for by shifting the riz lags upwards resulting in the compact lags seen in Figure B.16. The reason for this is probably explained by the presence of many bimodal distributions in Figure B.21 which indicates the algorithm had multiple preferred fitting solutions. In particular, many of the top-hat width distributions are bimodal with a sharp peak at ~ 0 which we found grew more significant as the analysis was run with more iterations. As such, in the limit of a large number of parameters we

would expect Javelin to fit the light-curve data with Dirac delta transfer functions and return lag estimates approaching the solutions returned in the Dirac delta PyROA fits. The distributions therefore indicate a problem with convergence which is more significant for the U band fit as it has the poorest cadence and is therefore the least constrained.

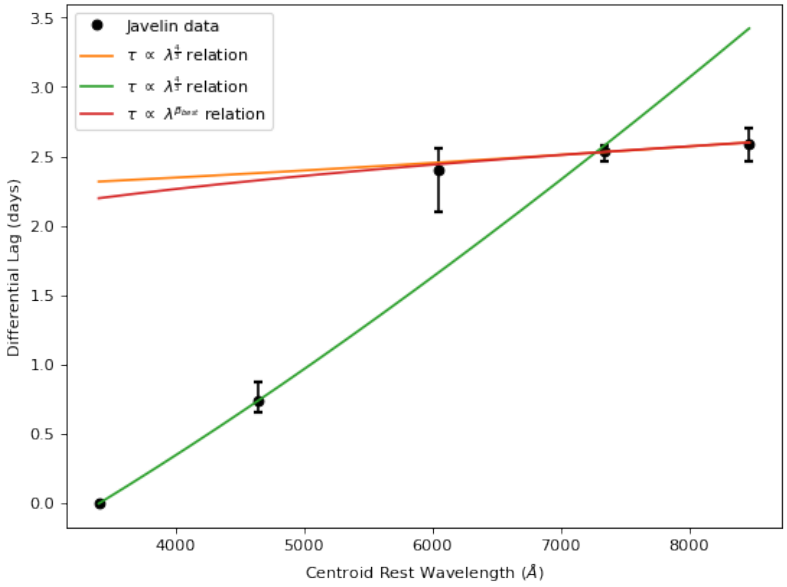

Figure B.16: $\tau \propto \lambda^{\beta}$ power laws fit to the Javelin lag estimates. As can be seen two separate thin disc power laws can be fit to the riz and ug data points with $\beta = 0.19 \pm 0.06$ and $\beta = \frac{4}{3}$ respectively.

B.3.2 Assorted Graphs

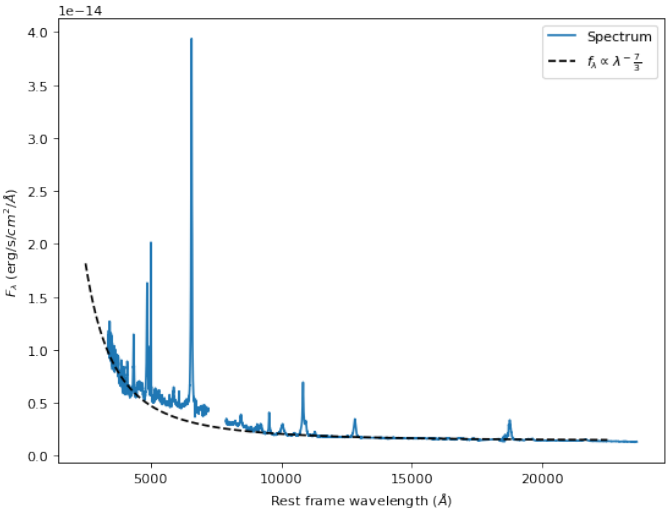

Figure B.17: Spectrum of 1H 2106-099 spanning the UV to the near infrared taken from Landt et al (2011). The thin disc power law relation $f_\lambda \propto \lambda^{-\frac{7}{3}}$ is fit to the spectrum.

Filter	X_{new}
U	3.82
G	3.70
R	3.63
I	3.59
Z	3.56

Table B.4: A set of proportionality factors X for Wiens law (4.1) derived following the approach of Mudd et al (2018) for each of the LCO filters used to observe 1H 2106-099.

Filter	Signal amplitude relative to noise amplitude
U	16.5
G	20.1
R	28.2
I	21.4
Z	10.8

Table B.5: Estimates for the amplitude of the model fit by PyROA in Figure 3.16 to the magnitude of the residuals.

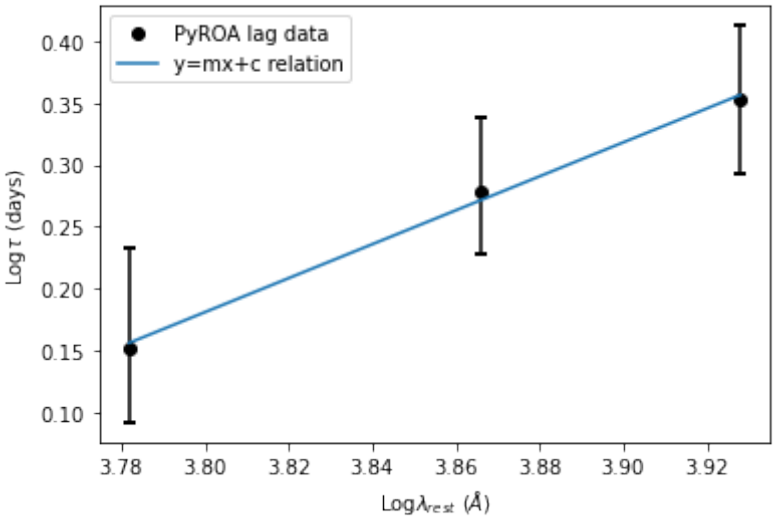

Figure B.18: Plotting of riz PyROA lag estimates in logarithmic space. A linear fit returned an estimated power law exponent $\beta = 1.37 \pm 0.36$

Filter	Lag Prediction (days)
J	8.67
H	12.65
K	18.42

Table B.6: Absolute lag predictions for the JHK emitting regions of the accretion disc in 1H 2106-099 interpolated from Figure B.25 using the PyceCREAM RM results.

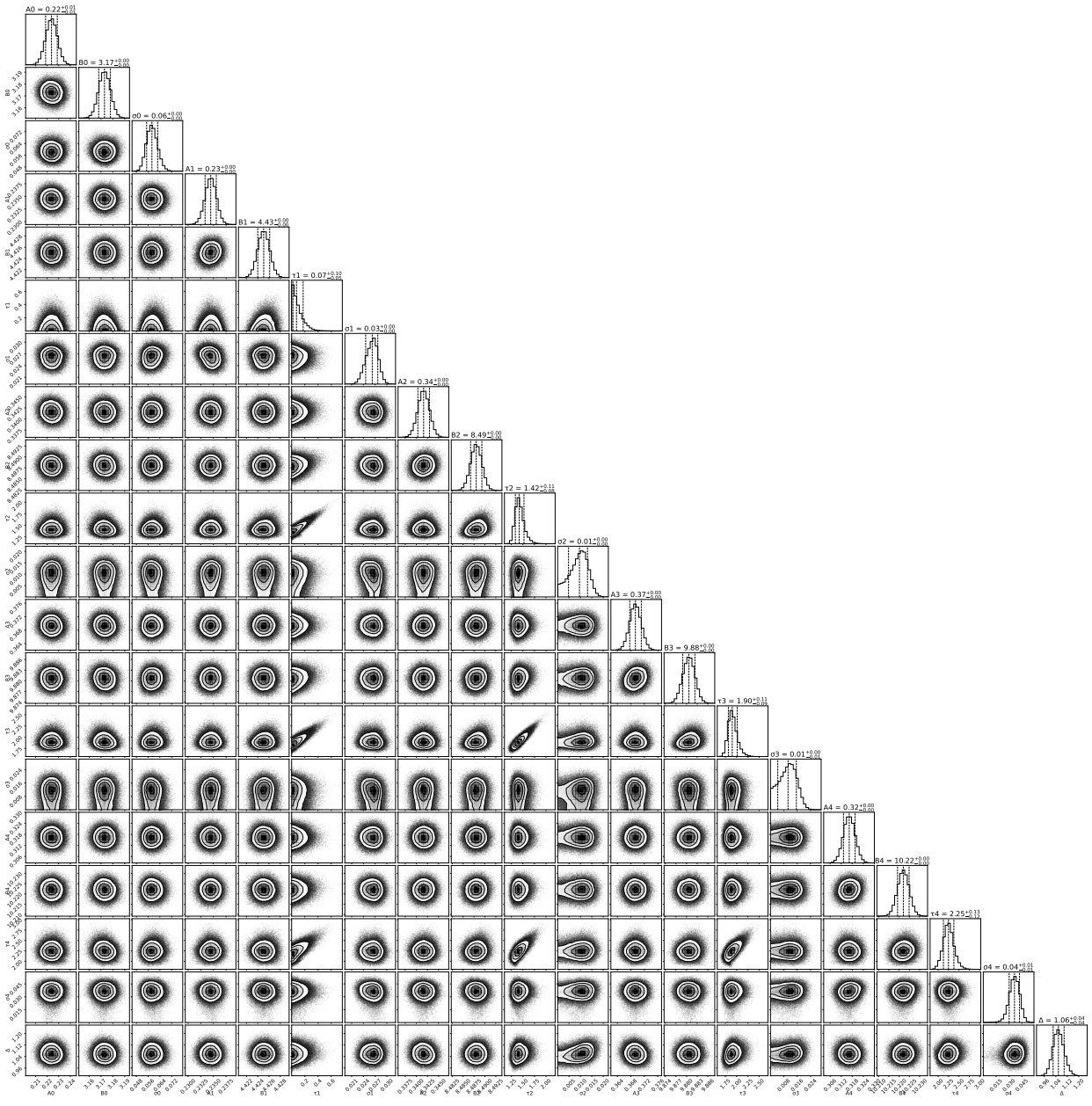

Figure B.19: PyROA corner plots to the 1H 2106-099 fits in Figure 3.16.

Filter	Lag Prediction (days)	
	Shifted	*Unshifted*
J	2.68	4.02
H	4.18	5.52
K	6.23	7.56

Table B.7: Differential lag predictions for the JHK emitting regions of the accretion disc in 1H 2106-099 interpolated from Figures B.23 using the Javelin RM results. Predictions for the original results in Figure 3.22 and the shifted results in Figure 3.23 are shown. The lag predictions are made with respect to the G band.

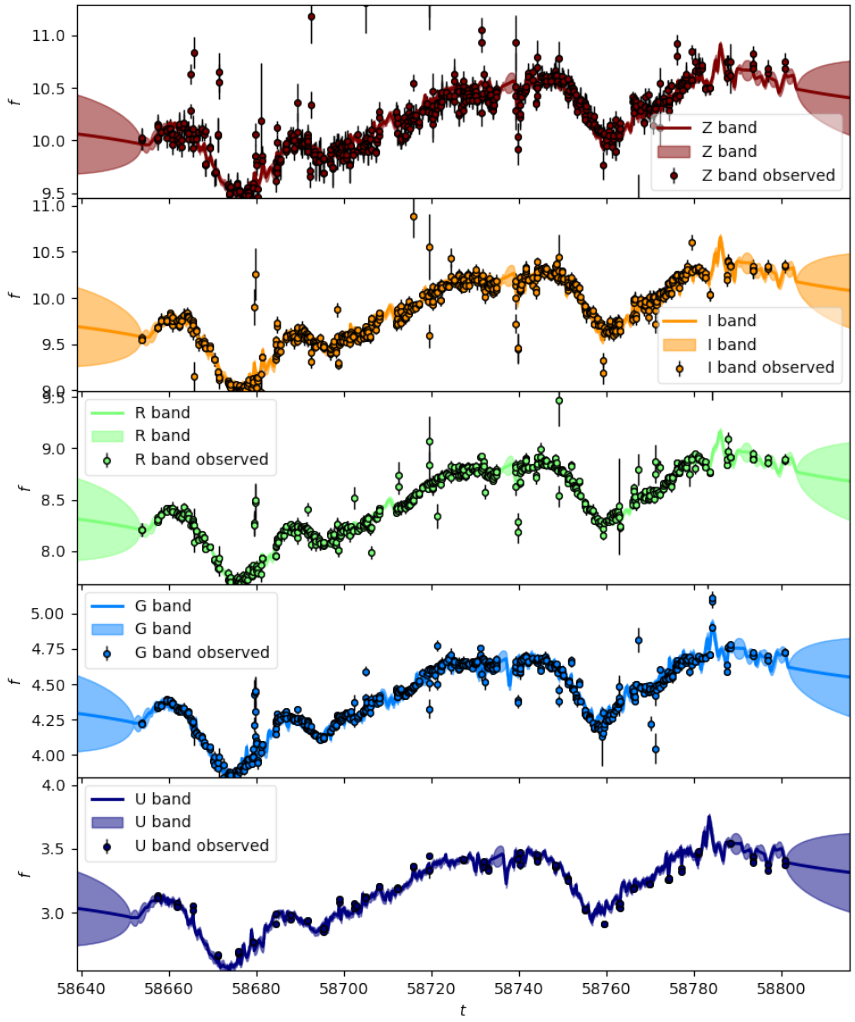

Figure B.20: Javelin fit to the full ugriz light-curves obtained for 1H 2106-099. Flux values are in mJy.

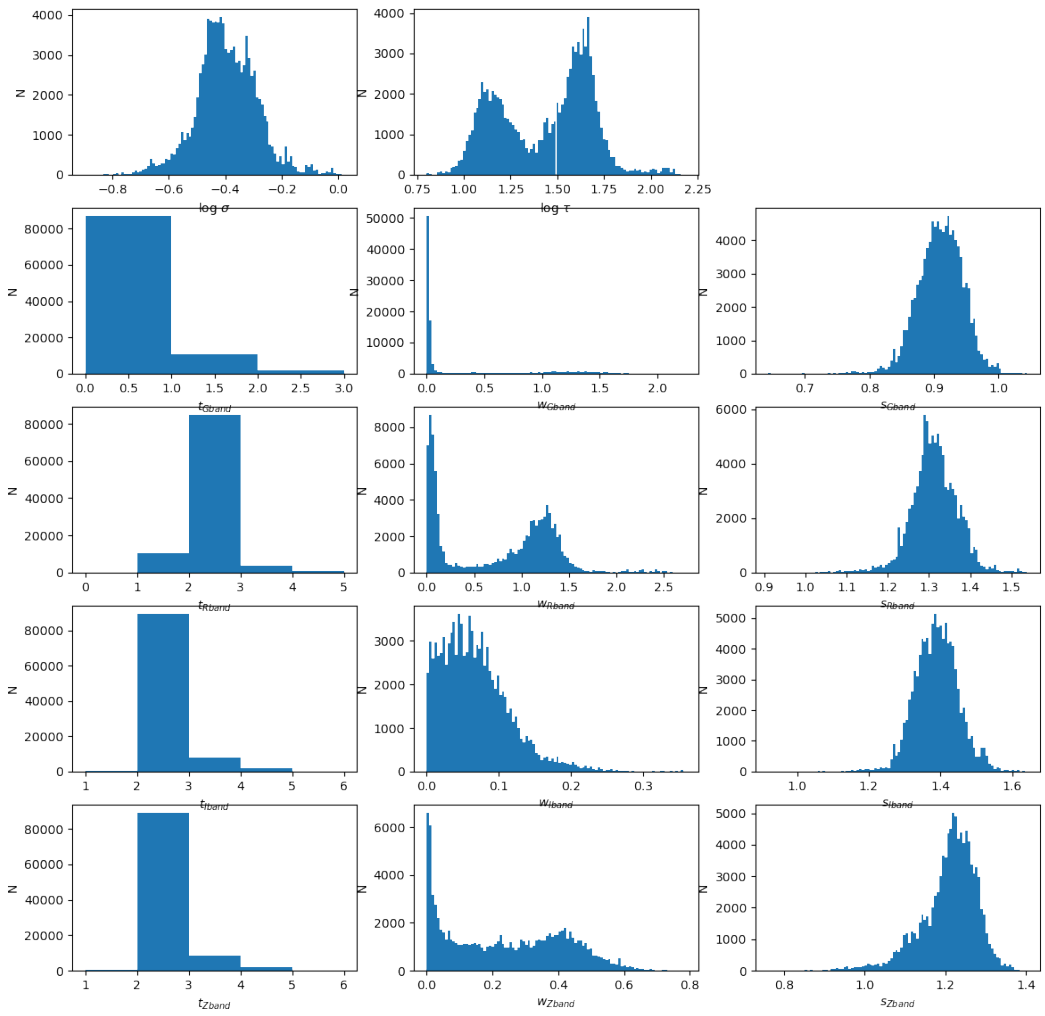

Figure B.21: Distributions for the 1H 2106-099 fits in Figure B.20.

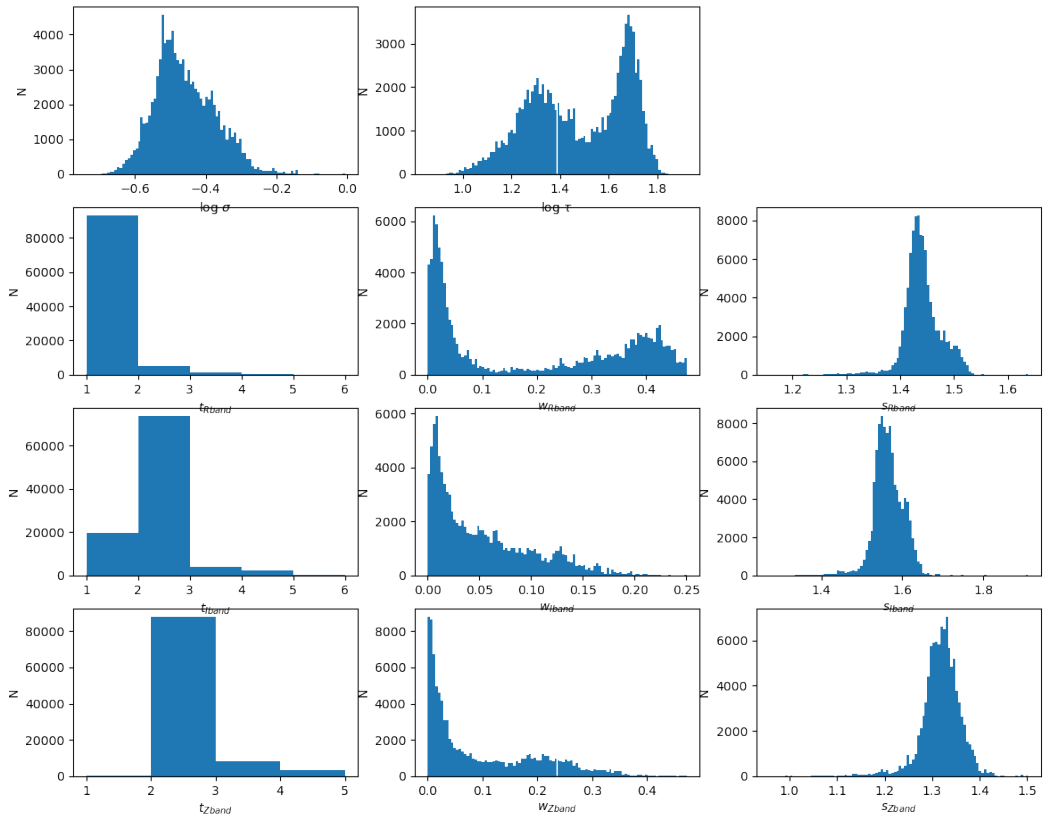

Figure B.22: Distributions for the griz 1H 2106-099 Javelin fits in Figure 3.17.

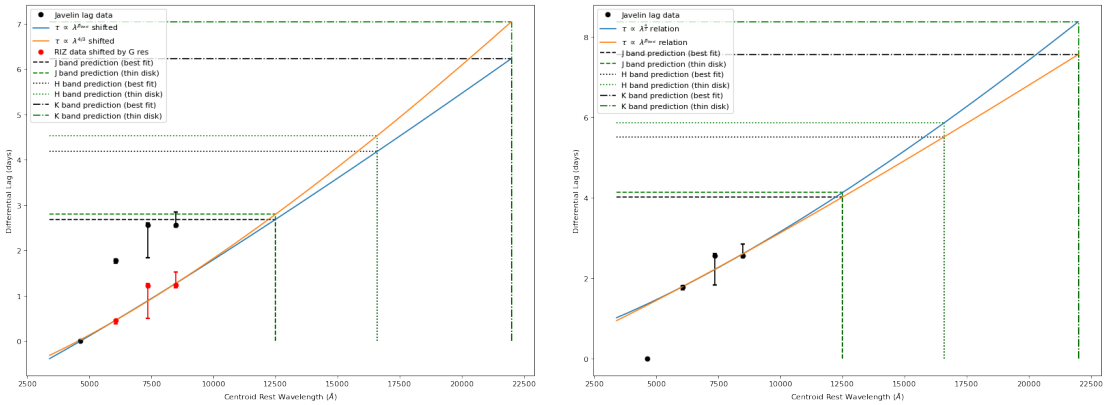

(a) Extrapolation of the shifted power law corresponding to Figure 3.23.

(b) Extrapolation of the unshifted power law corresponding to Figure 3.22.

Figure B.23: Extrapolations of the shifted and unshifted best-fit power law fit to the riz Javelin RM results into the JHK regime corresponding to Figures 3.23 and 3.22 respectively. Here $\beta_{best} = 1.12 \pm 0.20$. This allowed lag predictions in Table B.7 to be made.

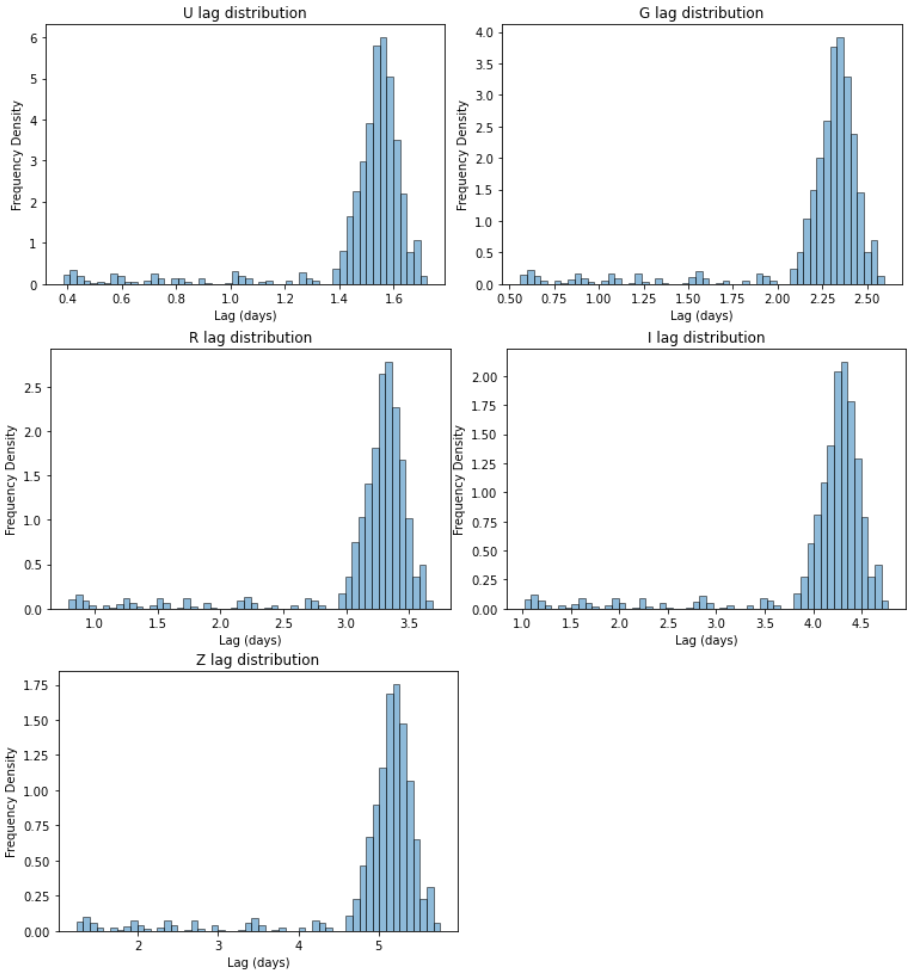

Figure B.24: PyceCREAM distributions for Figure 3.18.

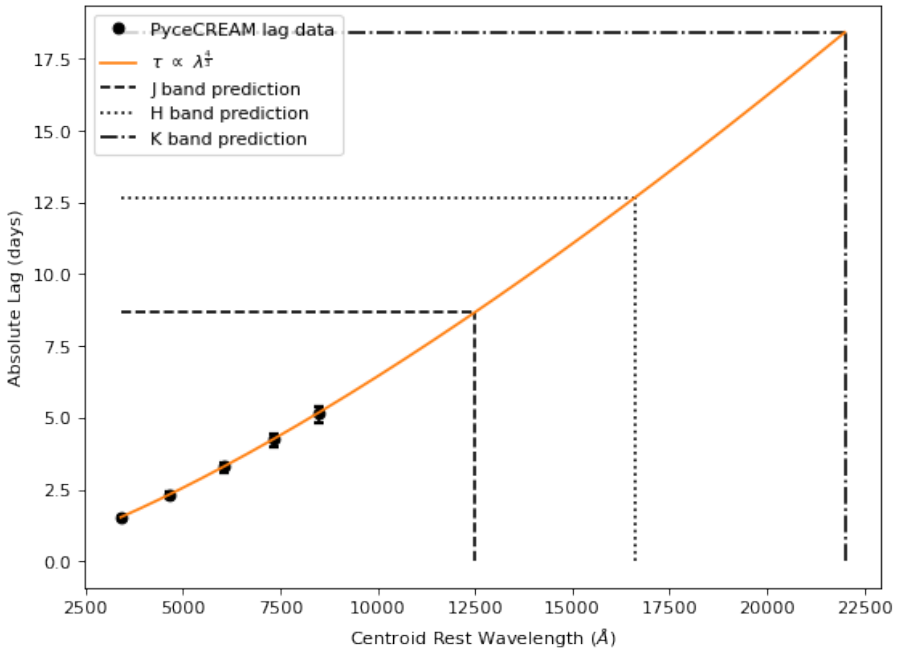

Figure B.25: Extrapolations of the best-fit power law fit to the PyceCREAM RM results into the JHK regime. This allowed lag predictions in Table B.6 to be made.

B.4 Design of dust RM campaigns

B.4.1 Definition of gaps

Histograms of the time separation between consecutive data points were generated for all objects within the Koshida et al (2014) and Minezaki et al (2019) data-sets and Log-Gaussian functions were fit using 'lmfit. An example histogram for SDSS J0007-0054 is shown in Figure B.26 from the Minezaki et al (2019) study. This was done reasonably well with the exception of PG 0953+414 and SDSS J0957-0023 from Minezaki et al (2019). Due to a lack of observing data, these objects generated inconclusive histograms and so were excluded from the investigation. New histograms were then generated for the

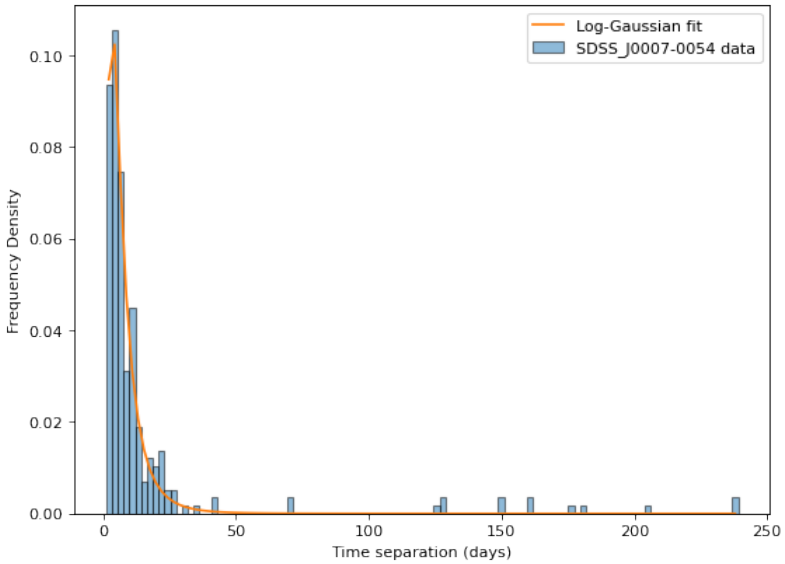

Figure B.26: A histogram of the time separation between consecutive data points for SDSS J0007-0054 from Minezaki et al (2019). Light-curve data from both the R and K bands is included. A Log-Gaussian distribution was fit to the histogram.

remaining objects in terms of the natural logarithm of the inter-data time separations which took an approximately Gaussian form as expected. This was determined by fitting Gaussian distributions to each histogram using 'lmfit' as shown below for SDSS J0007-0054 from the Minezaki et al (2019) study in Figure B.27. It should be mentioned that LBQS 1026-0032 and SDSS J2326-0030 generated incomplete Gaussian fits and so were excluded from the investigation due to the inability of the plotting software to accurately determine the Gaussian fitting parameters.

Each histogram was then normalised using the Gaussian mean μ and standard deviation σ fitted parameters by transforming each bin as $x \rightarrow x' = \frac{x-\mu}{\sigma}$. The normalised

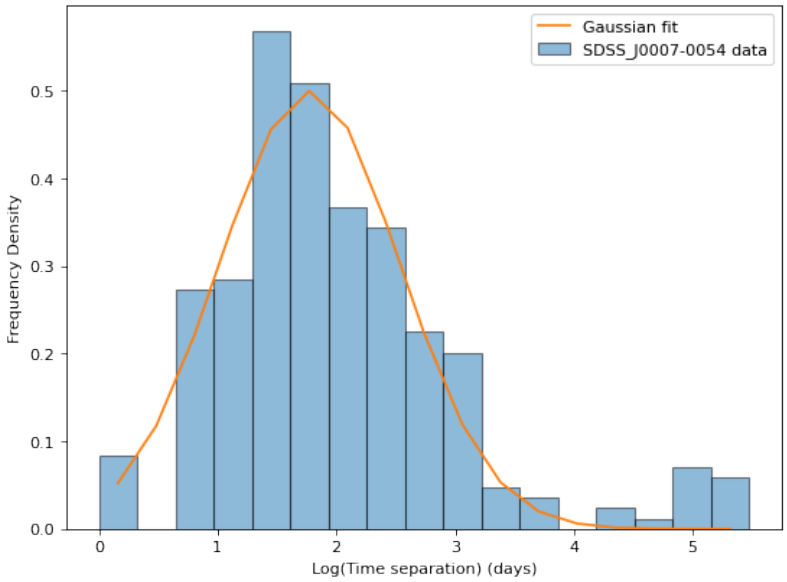

Figure B.27: A histogram of the natural logarithm of the time separation between consecutive data points for SDSS J0007-0054 from Minezaki et al (2019). Light-curve data from both the R and K bands is included. A Gaussian distribution was fit to the histogram.

histograms were then added together to produce a combined histogram which more closely resembled a Gaussian distribution due to the central limit theorem. The combined histogram for the Minezaki et al (2019) objects is shown in Figure B.28. This enabled a Gaussian distribution to be well fitted to the combined histogram with the fitting parameters being used to determine the upper 84^{th} and 97.5^{th} percentiles. These were then used to define the boundary between gaps and cadence for each object in the study by performing inverse normalisation $x'_{84/97.5} \rightarrow x_{84/97.5} = \sigma x_{84/97.5} + \mu$ and then converting back to the Log-Gaussian form by $e^{x_{84/97.5}}$. As such two separate definitions for gaps were derived based on the upper 1σ and 2σ boundaries from the Gaussian histograms.

The preceding statistical method of defining the gaps was performed separately for the Koshida et al (2014) and the Minezaki et al (2019) data-sets. This was because the two studies had starkly different typical cadences and so could be expected to have very different average gap sizes. It should be mentioned that the standard deviation used to define the boundary between gaps and cadence refers to the standard deviation in the Gaussian histograms and not the original Log-Gaussian distributions. We decided to define the gaps in relation to the Gaussian histograms as 2QZ J1345-0231 and PG 1613+658 from Minezaki et al (2019) both generated poor Log-Gaussian fits with unusable fitting parameter estimates but generated acceptable Gaussian fits after they had been transformed.

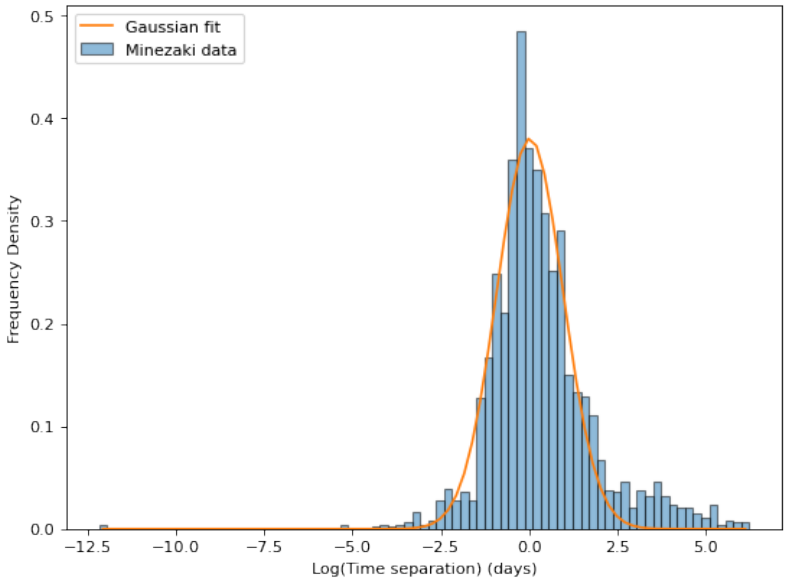

Figure B.28: A normalised histogram of the natural logarithm of the time separation between consecutive data points for the complete Minezaki et al (2019) data-set. A Gaussian distribution was fit to the histogram.

Therefore the Gaussian approach was chosen in the interests of not excluding these objects from the study particularly as PG 1613+658 was the last of the Palomar–Green (Schmidt & Green 1983) survey to remain in the study. Moreover, recalculating the gap boundary in terms of the Log-Gaussian standard deviation revealed no significant difference compared to the Gaussian standard deviation except for 4 objects. However, using the Gaussian approach for these 4 objects resulted in under-estimates for the gap boundary with respect to the Log-Gaussian approach which is a relatively safe effect for the following cadence analysis as gaps will not be included in the cadence definition. The only consequence would be slightly smaller cadence estimates.

B.4.2 Assorted Graphs

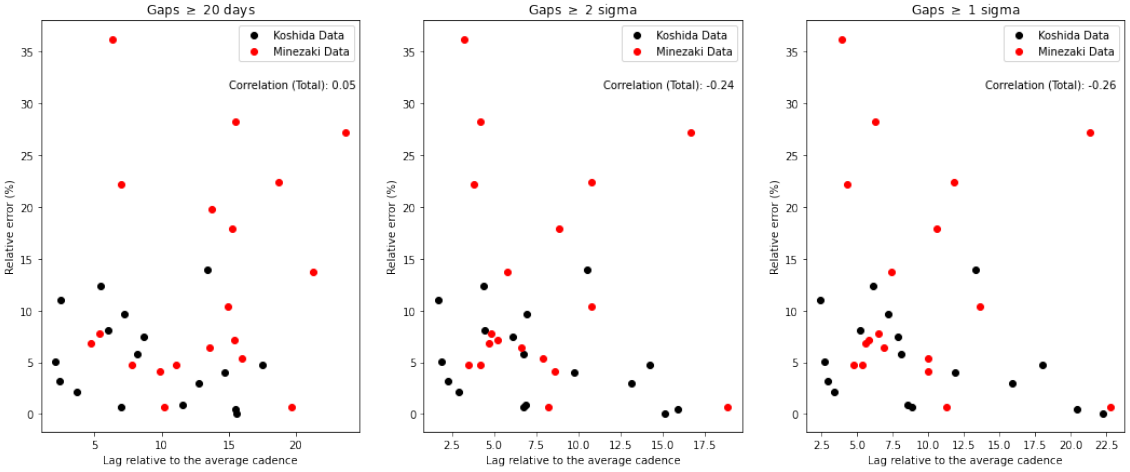

Figure B.29: The derived relationship between the relative error on Javelin lag estimates and the 'lag relative to the average cadence' for the Koshida et al (2014) and Minezaki et al (2019) data-sets. Here the results are shown for the three different gap definitions defined in Section 4.2. The Spearman's rank correlation measurements are shown.

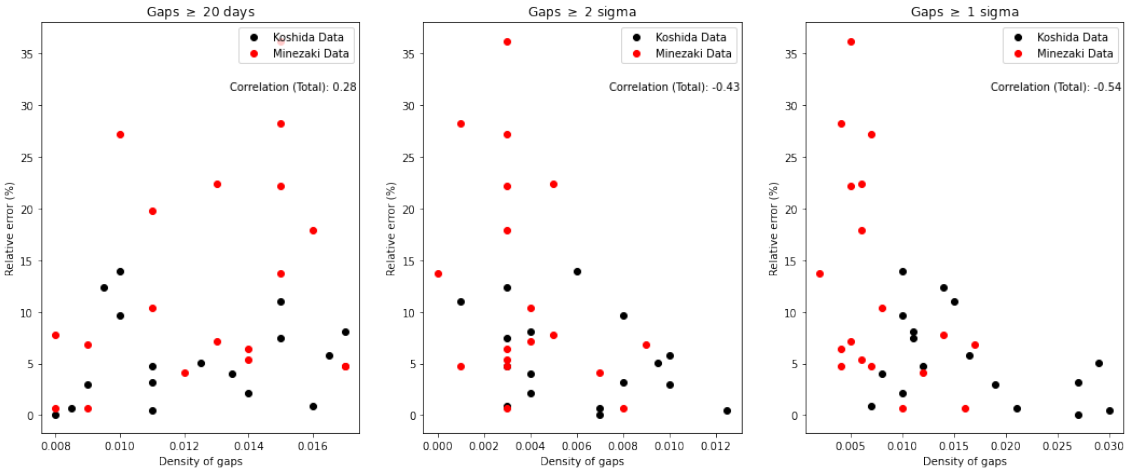

Figure B.30: The derived relationship between the relative error on Javelin lag estimates and the density of gaps for the Koshida et al (2014) and Minezaki et al (2019) data-sets. Here the results are shown for the three different gap definitions defined in Section 4.2. The Spearman's rank correlation measurements are shown.

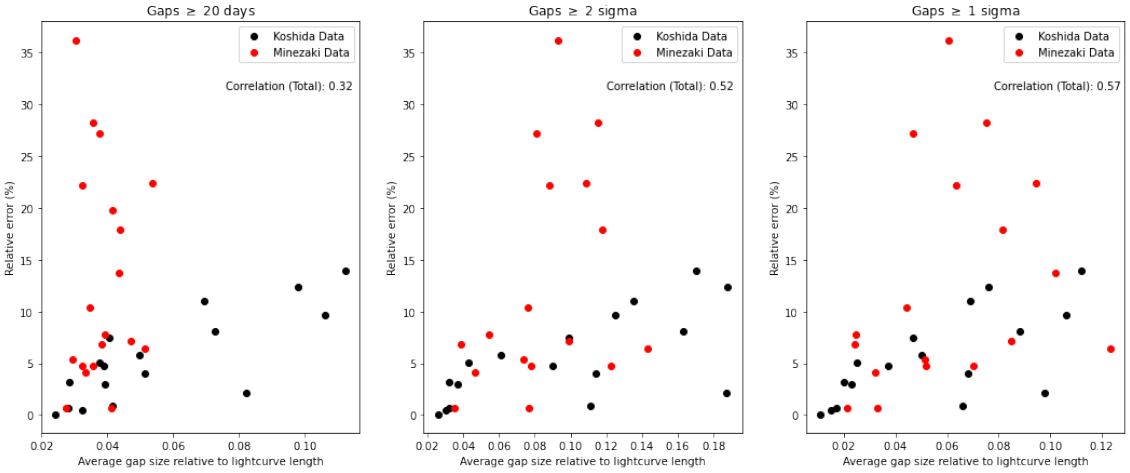

Figure B.31: The derived relationship between the relative error on Javelin lag estimates and the average gap size relative to the light-curve length for the Koshida et al (2014) and Minezaki et al (2019) data-sets. Here the results are shown for the three different gap definitions defined in Section 4.2. The Spearman's rank correlation measurements are shown.

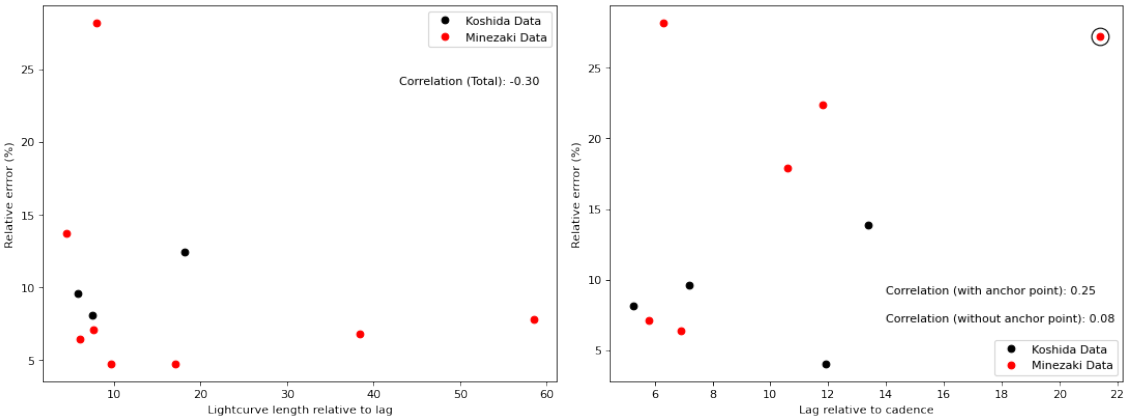

(a) The relationship between the γ parameter and the relative error on lag estimates after controlling for the ϵ parameter.

(b) The relationship between the ϵ parameter and the relative error on lag estimates after controlling for the γ parameter.

Figure B.32: Sub-samples selected from Figure 4.4.